

https://dspace.org/

Photocatalytic and thermoelectric properties of Cu3 (V, Nb , Ta) Se4 & Cd (G a , A l)2O4: a numerical investigation

Rugut, Elkana Kipkogei

2020

https://hdl.handle.net/10539/32000

Downloaded from a DSpace repository. https://dspace.org/



PHOTOCATALYTIC AND THERMOELECTRIC PROPERTIES OF $Cu_3(V,Nb,Ta)Se_4$ & $Cd(Ga,Al)_2O_4$: A numerical investigation

Elkana Kipkogei Rugut
(1214396@students.wits.ac.za)

Supervisors: **Prof. Daniel Joubert**
Dr. Glenn Jones

A thesis submitted to the Faculty of Science
University of the Witwatersrand,
in fulfillment of the requirements for
the degree of Doctor of Philosophy (PhD)
School of physics,
University of the Witwatersrand,
Johannesburg.

May 21, 2020

Declaration

I declare that this thesis is my own, unaided work. It is being submitted for the Degree of Doctor of Philosophy at the University of the Witwatersrand, Johannesburg. It has not been submitted before for any degree or examination at any other University.

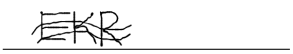

(Signature of candidate)

Date:May 21, 2020.

Abstract

Presently, the scientific community is exploring alternative approaches of generating, conserving and utilizing clean energy in ways that are not only economically viable, but also free from posing health hazards to humanity. This global challenge on energy, forms the basis of this study, whereby the cubic Cu_3QSe_4 (Q = Ta,Nb,V) sulvanites were examined using density functional theory (DFT) approaches, to ascertain if they hold any promising potential in photocatalysis whereby in the presence of light, water is broken down to obtain hydrogen which is a competent and safe energy carrier. On the other hand, thermoelectric materials play an instrumental role in efficient use of energy as they are capable of tapping heat energy that could have otherwise been lost and converts it into electricity. In line with this, $Cd(Ga,Al)_2O_4$ spinels were comprehensively studied to examine their applicability as the main component in the design of thermoelectric device.

The main goal of this study was to investigate the photocatalytic properties of the sulvanite-type compounds $Cu_3(V,Nb,Ta)Se_4$ and thermoelectric properties of spinel oxides $Cd(Ga,Al)_2O_4$ in line with clean energy production. In order to achieve these, the following properties were investigated: structural properties of compounds of interest such as lattice constants and Kleinman parameter were determined from relaxed structures. Thereafter, dynamical, energetic and mechanical stability test through phonon, cohesive energy, formation energy and elastic constant calculations were undertaken. Upon verifying their stability, optical study was carried out at the Bethe-Salpeter Equation (BSE) level of approximation to obtain the optical band gap of the sulvanite compounds followed by determination of the absolute band edges done via Mulliken analysis as well as via band gap center approach, to ascertain if $Cu_3(V,Nb,Ta)Se_4$ are indeed suitable for single photon water splitting.

Considering that photocatalysis occurs at the surface of a material, surface properties of $Cu_3(V,Nb,Ta)Se_4$ sulvanites were investigated through calculation of surface energies, vacuum potential and work function among other photocatalytically relevant parameters. At the peak of the study, transport properties of $Cd(Ga,Al)_2O_4$ were then determined by solving Boltzmann transport equations to obtain the Seebeck coefficient, charge carrier concentration and lifetime, thermal and electrical conductivity as well as power factor and consequently the figure of merit. These in turn provide an indication whether these spinel oxides possess good thermoelectric properties.

Dedication

This thesis is dedicated to my beloved family.

Acknowledgements

First of all, I would like to express my sincere gratitude to my supervisors Prof. Daniel Joubert and Dr. Glenn Jones for their continuous support, patience, guidance, motivation and immense knowledge. Secondly, the work described in this thesis was fully funded by the Johnson Matthey Technology Centre (under contract number JM6473), I appreciate JM fraternity for their unconditional assistance. Thirdly, I am grateful to my family for their love, prayers and support during all these years of my academic journey, not forgetting my able mentors in academia for the instrumental role they have played. Fourthly, I acknowledge the Centre for High Performance Computing (CHPC), South Africa, for providing computational resources to this research project. Lastly, I would like to appreciate my colleagues for the valuable discussions.

Contents

1 INTRODUCTION **2**
- 1.1 Energy crisis . . . 2
- 1.2 Aim and objectives of the study . . . 2
- 1.3 Outline of the thesis . . . 3
- 1.4 Sulvanite compounds . . . 3
- 1.5 Spinel oxides . . . 5

2 LITERATURE REVIEW **7**
- 2.1 Review of previous work . . . 7
- 2.2 Thermoelectric materials . . . 9
- 2.3 Aspects of good thermoelectric materials . . . 11
- 2.4 Applications of thermoelectricity . . . 13
- 2.5 Hydrogen generation techniques . . . 15
- 2.6 Rationale of photocatalysis . . . 17
- 2.7 Properties of a good photocatalytic material . . . 20
- 2.8 Applications of photocatalysis . . . 23

3 THEORETICAL FRAMEWORK **26**
- 3.1 Band edge prediction techniques . . . 26
- 3.2 Surface properties . . . 28
- 3.3 Charge density decomposition . . . 32
- 3.4 Boltzmann Transport Equations (BTE) . . . 34
- 3.5 Relationship between kinetic coefficients and Seebeck coefficient . . . 34
- 3.6 Transport and thermoelectric properties . . . 36
- 3.7 Relationship between effective mass and Seebeck coefficient . . . 37

4 COMPUTATIONAL DETAILS **39**
- 4.1 Workflow . . . 39
- 4.2 Convergence in *ab initio* calculations . . . 40
- 4.3 Structure optimization . . . 41
- 4.4 Surface energy simulation steps . . . 41
- 4.5 Electronic structure . . . 42
- 4.6 Midgap surface states . . . 43
- 4.7 Vibrational properties . . . 43
- 4.8 Mechanical properties . . . 44

5 RESULTS AND DISCUSSION **50**

5.1 $Cd(Ga,Al)_2O_4$ spinel oxides . . . 51
5.2 Cu_3QSe_4 sulvanites . . . 63
5.3 Optical properties . . . 72
5.4 Determination of surface energy in Cu_3TaSe_4 . . . 74
5.5 Determination of surface energy in Cu_3VSe_4 . . . 76
5.6 Determination of surface energy in Cu_3NbSe_4 . . . 78
5.7 Wulff construction . . . 80
5.8 Charge density difference via Bader analysis . . . 82
5.9 Determination of work function in Cu_3QSe_4 sulvanites . . . 83
5.10 Determination of band edge location using Mulliken approach . . . 84

6 CONCLUSIONS **87**

References **110**

List of Figures

1.1 Crystal structure of Cu_3TaSe_4. . . . 4
1.2 Brillouin zone of Cu_3TaSe_4. . . . 4
1.3 Crystal structure of $CdGa_2O_4$. . . . 5
1.4 Brillouin zone of $CdGa_2O_4$. . . . 5

2.1 Diagrammatic representation of the thermoelectric effects. . . . 10
2.2 Diagramatic representation of the relationship between ZT and efficiency. . . . 11
2.3 Diagrammatic representation of the optimization of the figure of merit (ZT). . . . 12
2.4 Hydrogen generation techniques that involve water. . . . 15
2.5 Reaction energy diagram. . . . 18
2.6 Water splitting cartoon. . . . 18
2.7 Water splitting process. . . . 19
2.8 Solar energy distribution. . . . 20

3.1 Slab surface model. . . . 29
3.2 Cluster surface model. . . . 29
3.3 Low index orientation for a simple cubic crystal structure. . . . 30
3.4 Surface models for a simple cubic crystal structure obtained from surface explorer for low index facets. . . . 30
3.5 Schematic diagram showing charge density decomposition. . . . 32
3.6 Diagrammatic representation of the Seebeck effect. . . . 36
3.7 Workflow for computing ZT. . . . 37

4.1 Simulation steps. . . . 39
4.2 Cut-off energy convergence for Cu_3TaSe_4 along various low index surface orientations. . . . 41
4.3 Schematic diagram showing surface simulation steps. . . . 42

5.1 The electronic band structure for $CdGa_2O_4$. . . . 52
5.2 The electronic band structure for $CdAl_2O_4$. . . . 52
5.3 The phonon band structure together with partial and total density of states for $CdGa_2O_4$. 55
5.4 The phonon band structure together with partial and total density of states for $CdAl_2O_4$. 55
5.5 Specific heat capacity of $Cd(Ga,Al)_2O_4$. . . . 56
5.6 Helmholtz free energy of $Cd(Ga,Al)_2O_4$. . . . 56
5.7 Entropy of $Cd(Ga,Al)_2O_4$. . . . 56
5.8 Lattice thermal conductivity of $Cd(Ga,Al)_2O_4$. . . . 57
5.9 Cumulative lattice thermal conductivity of $Cd(Ga,Al)_2O_4$ at 300K. . . . 57
5.10 Group velocity of $CdGa_2O_4$. . . . 57
5.11 Group velocity of $CdAl_2O_4$. . . . 57

5.12 Phonon lifetime of $CdGa_2O_4$. 58
5.13 Phonon lifetime of $CdAl_2O_4$. 58
5.14 Mean free path of $Cd(Ga,Al)_2O_4$. 58
5.15 Total modal Grüneisen parameter of $Cd(Ga,Al)_2O_4$. 58
5.16 Seebeck coefficient of $CdGa_2O_4$. 59
5.17 Electrical conductivity of $CdGa_2O_4$. 59
5.18 Electronic contribution to thermal conductivity of $CdGa_2O_4$. 60
5.19 Total thermal conductivity of $CdGa_2O_4$. 60
5.20 Power factor of $CdGa_2O_4$. 60
5.21 Figure of merit of $CdGa_2O_4$. 60
5.22 Seebeck coefficient of $CdAl_2O_4$. 61
5.23 Electrical conductivity of $CdAl_2O_4$. 61
5.24 Electronic contribution to thermal conductivity of $CdAl_2O_4$. 62
5.25 Total thermal conductivity of $CdAl_2O_4$. 62
5.26 Power factor of $CdAl_2O_4$. 62
5.27 Figure of merit of $CdAl_2O_4$. 62
5.28 The electronic band structure together with partial and total density of states for Cu_3TaSe_4. 64
5.29 The electronic band structure together with partial and total density of states for Cu_3VSe_4. 64
5.30 The electronic band structure together with partial and total density of states for Cu_3NbSe_4. 64
5.31 The phonon band structure together with partial and total density of states for Cu_3TaSe_4. 67
5.32 The phonon band structure together with partial and total density of states for Cu_3NbSe_4. 67
5.33 The phonon band structure together with partial and total density of states for Cu_3VSe_4. 67
5.34 Entropy of Cu_3QSe_4. 68
5.35 Helmholtz free energy of Cu_3QSe_4. 68
5.36 Specific heat capacity of Cu_3QSe_4. 69
5.37 Calculated κ_l of Cu_3QSe_4. 70
5.38 Cumulative κ_l of Cu_3QSe_4 at 300 K. 70
5.39 Group velocities of Cu_3QSe_4. 70
5.40 Phonon lifetimes of Cu_3QSe_4. 71
5.41 Comparison of mean free path of Cu_3QSe_4. 71
5.42 Total Grüneisen parameter of Cu_3QSe_4. 72
5.43 Mean free path of Cu_3QSe_4. 72
5.44 Determination of optical gap of Cu_3TaSe_4. 73
5.45 Determination of optical gap of Cu_3NbSe_4. 73
5.46 Determination of optical gap of Cu_3VSe_4. 73
5.47 Determination of the bulk energy of Cu_3TaSe_4 from linear plots for various surface orientations. 74
5.48 Total slab energy per formula unit convergence with respect to the slab size. 75
5.49 100 and 111 surface energy convergence. 75
5.50 110 surface energy convergence. 75
5.51 Determination of the bulk energy of Cu_3VSe_4 from linear plots for various surface orientations. 76
5.52 Total slab energy per formula unit convergence with respect to the slab size. 77
5.53 100 and 111 surface energy convergence. 77
5.54 110 surface energy convergence. 77
5.55 Determination of the bulk energy of Cu_3NbSe_4 from linear plots for various surface orientations. 78
5.56 Total slab energy per formula unit convergence with respect to the slab size. 79

5.57 100 and 111 surface energy convergence. 79
5.58 110 surface energy convergence. 79
5.59 Predicted equilibrium shape of sulvanite crystals using Wulffman program. Due to large differences in the predicted values of surface energies, only 110 facet appears in the morphology. 80
5.60 Surface and bulk DOS for Cu_3TaSe_4. 81
5.61 Surface density of states for Cu_3TaSe_4. 81
5.62 Surface and bulk DOS for Cu_3NbSe_4. 81
5.63 Surface density of states for Cu_3NbSe_4. 81
5.64 Surface and bulk DOS for Cu_3VSe_4. 82
5.65 Surface density of states for Cu_3VSe_4. 82
5.66 The charge density difference in Cu_3QSe_4 with the volumetric sections. 82
5.67 The charge density difference in Cu_3QSe_4 without the volumetric sections. 83
5.68 Determination of work function of Cu_3QSe_4 from vacuum potential and Fermi level for various surface orientations. The electrostatic potential was averaged in the *x*- and *y*-directions to get the potential along the *z*-direction. 84
5.69 Alignment of the band edges using Mulliken approach at PH = 0. 85
5.70 Position of the band edges using BGC approach at PH = 0. 86

6.1 The effect of PH on redox potential of water via Mulliken approach at PH of 7. 91
6.2 The effect of PH on redox potential of water via BGC approach at PH of 7. 91

List of Tables

5.1 Structural and energetic properties of $Cd(Ga,Al)_2O_4$ spinel oxides. 51
5.2 Fundamental gaps (eV). 52
5.3 Mechanical properties of $Cd(Ga,Al)_2O_4$ spinel oxides. 54
5.4 Structural and energetic properties of Cu_3QSe_4 sulvanites. 63
5.5 Fundamental gaps (eV). 64
5.6 Mechanical properties of Cu_3QSe_4 sulvanites. 66
5.7 Cu_3QSe_4 surface properties for the stable 110 orientation. 83
5.8 Pearson absolute electronegativity values for elements of interest. 84
5.9 Band alignment in Cu_3QSe_4 via Mulliken approach. 85
5.10 Cu_3QSe_4 band edges based on BGC approach. 86

1

INTRODUCTION

In this Chapter, we discuss the dangers posed by the inevitable global energy crisis on humanity. We also provide the aim and the specific objectives which the current study was geared towards achieving. Additionally, we present the scope of the thesis as well as what has been explored and the existing gaps to be filled in exploring our compounds of interest - sulvanites and spinels.

1.1 Energy crisis

The negative impact of conventional energy sources on the environment has been stimulating the research on clean energy production and use. Although oil, gas and coal may continue to exist for next several decades, its reserves keep declining which may result in their depletion. Any alternative energy source must seek to confront the rampant climate change associated with the conventional sources. Such an alternative should cost less and have low carbon intensity when compared with petroleum products [1]. This has also been triggered by increase in population. The growing global population rate is estimated to be 200,000 persons per day. This would eventually cause increase in energy demand on limited fossil fuel reserves. Fossil fuel accounts for approximately 86% of the global primary energy sources [2]. This dominance of the fossil fuels on energy production results in serious global problems such as emission of greenhouse gases resulting in serious climate change, breakdown of the ozone layer hence the increase in level of ultraviolet radiation, acid rains, decrease in biodiversity and increase in soil erosion among others [3]. Also, dwindling fuel supply could propel environmental catastrophes, wars and economic collapse [4]. To address these obvious challenges, the scientific community is extensively examining the alternative sources of energy such as solar, wind, geothermal and water just to mention a few, as possible options to replace oil. This global challenge therefore forms the basis of our current study, whereby sulvanite compounds are explored to ascertain their viability in photocatalytic applications whereas the spinel oxides are investigated to see if they hold any tangible potential in thermoelectric applications.

1.2 Aim and objectives of the study

The aim of this study was to investigate the photocatalytic properties of sulvanite-type compounds $Cu_3(V,Nb,Ta)Se_4$ and thermoelectric properties of spinel oxides $Cd(Ga,Al)_2O_4$ for clean energy produc-

tion. In order to achieve the main goal of this research, the following properties were investigated:

1. Structural properties of compounds of interest such as lattice constants and Kleinman parameter were determined from relaxed structures.
2. Dynamical, energetic and mechanical stability test through phonon, cohesive energy, formation energy and elastic constant calculations were undertaken.
3. Optical study was carried out at the Bethe-Salpeter Equation (BSE) level of approximation to obtain the optical band gap of sulvanite compounds.
4. Absolute band edges were then determined via Mulliken analysis as well as via band gap center approach to ascertain if $Cu_3(V,Nb,Ta)Se_4$ are indeed suitable for single photon water splitting.
5. Surface properties of $Cu_3(V,Nb,Ta)Se_4$ were investigated through calculation of surface energies, vacuum potential and work function among other photocatalytically relevant parameters.
6. Computation of the lattice thermal conductivity of the spinel oxides as well as the sulvanite-type compounds was also done.
7. Transport properties of $Cd(Ga,Al)_2O_4$ spinels were then evaluated by solving Boltzmann transport equations to obtain the figure of merit, Seebeck coefficient, charge carrier concentration, lifetime, thermal and electrical conductivity as well as power factor. These help establish whether these spinel oxides possess good thermoelectric properties.

1.3 Outline of the thesis

The remainder of the thesis is organized as follows: in Chapter 1, we briefly discuss the compounds of interest namely the sulvanites and spinel oxides. In Chapter 2, we review previous work on $Cd(Ga,Al)_2O_4$ spinels and $Cu_3(Ta, V, Nb)Se_4$ sulvanites as well as provide the definition of thermoelectric materials, thermoelectric effects, discussion on how to gauge the efficiency of a thermoelectric system, aspects of good thermoelectric material and applications of thermoelectricity. Also, we discuss in a nutshell the hydrogen generation techniques that involves water where we pay more emphasize on photocatalysis. The properties of a good photocatalytic material, as well as their areas of application and water splitting processes are reviewed.

In Chapter 3, we summarize the theoretical framework that forms the basis of this study. In Chapter 4, we give the computational details of the study in form of the workflow and also consider how structural optimization was done, how stability tests were carried out as well as a description of how lattice thermal conductivity, transport coefficients, optical gaps and surface energies were evaluated. In Chapter 5, we present and discuss our results in detail, as well as benchmark with the existing theoretical and experimental data where possible. In the appendix section, we provide the supplementary information to our current study along with an outline of the publications that emanated from this work.

1.4 Sulvanite compounds

Sulvanite is a mineral consisting of a sulfide of copper and vanadium (Cu_3VS_4). The isostructural compounds Cu_3VS_4, Cu_3VSe_4, Cu_3NbSe_4 and Cu_3TaSe_4 belong to the family of sulvanites [5] and crystallize in the cubic crystal system of space group $P\bar{4}3m$ (No. 215) [6], with eight atoms in the unit

cell. Cu, Ta and Se atoms are positioned at 3d (0.5,0,0), 1a (0,0,0) and 4e (u,u,u) sites of Wyckoff coordinates, respectively [7]. Where u is the internal parameter. Sulvanite compounds have potential application in opto-electronics attributed to their wide band gap [8], used as light modulators [9], applied in solar cells as p-type absorbing layers in heterostructures and dielectric mirrors due to their unique physical properties and the fact that sulvanites, especially Cu_3TaSe_4 possess lattice constant comparable to that of silicon, 5.66 Å and 5.43 Å respectively; which makes the growth of heteroepitaxial thin films of Cu_3TaSe_4 on silicon substrates possible. Seebeck coefficient measured at room temperature from sintered pellets of Cu_3TaSe_4 indicate conductivity with a value of $+24\ \mu VK^{-1}$ [8]. Since Cu_3QSe_4 (Q = V,Nb,Ta) sulvanites are cubic with very high symmetry, they are expected to show optical isotropy. Hence, their optical properties are independent of crystal orientations, which is advantageous in that the challenges involved in manufacturing anisotropic materials with particular orientation are eliminated [10]. Cu_3QSe_4 are characterized by a 3D arrangement of $CuSe_4$ and QSe_4 tetrahedra connected by common edges and the $CuSe_4$ share vertices with each other in all directions to form a three-dimensional framework [6] as displayed in Figure 1.1 alongside its Brillouin zone [11] exhibited in Figure 1.2.

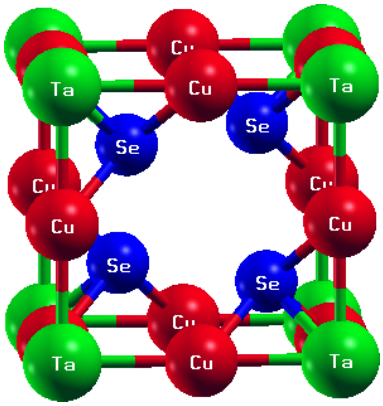

Figure 1.1: Crystal structure of Cu_3TaSe_4.

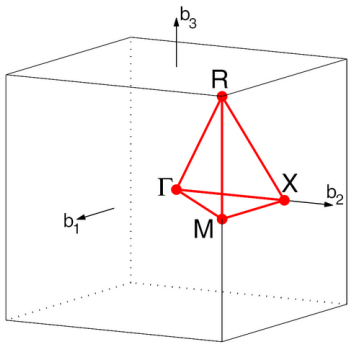

Figure 1.2: Brillouin zone of Cu_3TaSe_4.

To review what has been done on sulvanite compounds, Cu_3QSe_4 in specific, in 1963, Arkel and Crevecoeur [12] reported Cu_3VSe_4 to be black in color and narrow bandgap. Whereas Cu_3NbSe_4 and Cu_3TaSe_4 were red and green respectively, with wide band gaps. A decade ago, Delgado *et al.* [6] reported the structural analysis of Cu_3TaSe_4 from X-ray powder diffraction data obtained via Rietveld method. Espinosa-García *et al.* [5], did theoretical study on the elastic properties of sulvanite compounds and concluded that they are brittle and fragile. They further investigated the thermal properties of sulvanites such as the average sound velocity and Debye temperatures. This was worthwhile because in principle, we can predict the behavior of a material under high pressure and high temperature environments from the basis of its thermodynamic properties [13]. The melting points of Cu_3TaSe_4 and Cu_3NbSe_4 are reported to be 1328 and 1206 K respectively [7]. Recently (2017), Yuan *et al.* reported the thermoelectric properties of Cu_3MCh_4 (M = V,Nb,Ta; Ch = Se,Te) from first principles, having ZT values of around 2 with small effective masses, where majority charge carriers are holes [14].

Although a number of researchers have explored synthesis, crystal structures, thermal and optical properties of sulvanite compounds, we are not aware of any existing theoretical or experimental studies on surface properties of Cu_3(V,Nb,Ta)Se_4 so far, which motivated us to investigate. We have considered sulvanite compounds consisting of selenium only, this is because though sulfur and tellurium belongs to chalcogen group as selenium, tellurium is a rare element and possess some degree of toxicity [15] whereas sulfide photocatalyst are known to be unstable in the water-oxidation reaction under visible light since the S^{2-} anions are more susceptible to oxidation than water, thereby causing photodegradation of the

photocatalyst [16]. In addition, semiconductors are particularly useful as photocatalyst because of their favorable combination of electronic structure, light absorption properties, charge transport characteristics and excited state lifetimes [17].

1.5 Spinel oxides

A spinel is a hard glassy mineral that occur as octahedral crystals of variable colour consisting mainly of magnesium and aluminium oxides having a general formula AB_2O_4. More information about spinel compounds has been elaborated by Garcia [18]. In Geophysics, spinel ($MgAl_2O_4$) is known to be a constituent of the shallow upper mantle [19]. Moreover, its prototypical character for ceramics and its diverse electronic applications has triggered investigation of other spinel oxides [20]. In this study, we are interested in thermoelectric properties of $Cd(Ga,Al)_2O_4$. Structural studies of spinel oxides of interest have been conducted by several researchers both theoretically and experimentally [21–24]. $Cd(Ga,Al)_2O_4$ spinels occur in face centered cubic structure composed of 8 formula units consisting of 56 atoms; 8 Cd cations, 16 Ga cations and 32 O anions. The positions of the cations Cd and Ga are fixed by the symmetry, but the anion O positions are variable and are specified by the anion parameter u. Cd cations occupy the Wyckoff position 8a (0.125, 0.125, 0.125), Ga cations are located at the Wyckoff position 16d (0.5, 0.5, 0.5) and O anions are positioned at the Wyckoff position 32e (u, u, u) [25]. Its space group is *Fd-3m* as shown in Figure 1.3 alongside its Brillouin zone [11] displayed in Figure 1.4.

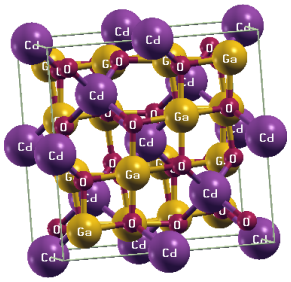

Figure 1.3: Crystal structure of $CdGa_2O_4$.

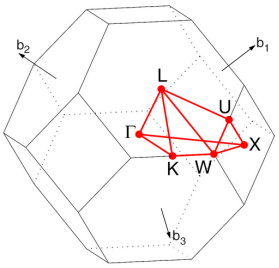

Figure 1.4: Brillouin zone of $CdGa_2O_4$.

Regarding cadmium gallate ($CdGa_2O_4$), Bouhemodou *et al.* [26] carried out the structural, electronic and optical properties from first principles using WIEN2K code. They investigated as well the pressure induced energy shift, where they noticed that band gap increases almost linearly with an increase in pressure within (0-80) GPa. In addition, the same authors [27], explored the behavior of lattice constants, elastic constants and bulk modulus of $CdGa_2O_4$ and $CdAl_2O_4$, where they noted that C_{11}, C_{12} and B_0 varied linearly with respect to change in pressure whereas C_{44} showed no significant change.

Omata *et al.* [28], reported the electrical conductivity of sintered sample of $CdGa_2O_4$ to be about 10^2 S/cm, hence a promising material as a transparent electronic conductor [29]. According to Nguyen and Koffyberg [30], $CdGa_2O_4$ has a low resistivity and a wide experimental optical band gap of 3.07 eV (4.05) for indirect (direct) transition with electron affinity of 4.3 eV. Photoluminesence (PL) study conducted by Zhitar *et al.* [31], showed that PL features of $CdGa_2O_4$ could be tuned using optical filters. Xiangfeng and Tamaki [32], prepared $CdGa_2O_4$ sensor using powder calcined at 800°C giving high sensitivity along with good selectivity to dilute methanethiol (CH_3SH) at 300°C.

Regarding cadmium aluminate ($CdAl_2O_4$), Bouhemadaou *et al.* [33], reported its thermal properties such as sound velocity, coefficient of thermal expansion with respect to temperature and pressure,

heat capacity and effective mass among other thermal properties. Moreover, the Grüneisen parameter (γ) of $CdAl_2O_4$ has been reported [34], though in their case, γ was obtained at high temperatures as compared to our value determined at absolute temperature (300 K). Guaqiang *et al.* [35], reported a high performance co-precipitation $CdAl_2O_4$ catalyst for the isomerization of dipotassium 1,8-naphthalenedicarboxylate. Both $CdGa_2O_4$ and $CdAl_2O_4$ have been studied as phosphors [36–38]. At the moment, we are not aware of any report on thermoelectric studies on $CdGa_2O_4$ and $CdAl_2O_4$ spinels, which inspired us to examine.

2

LITERATURE REVIEW

In this chapter, we review various research studies that were previously done by other scientists as well as discuss some of the basic scientific ideas about photocatalysis and thermoelectricity. We also present the aspects of material choices that ought to be considered and the possible areas of applications.

2.1 Review of previous work

In this section, previously reported experimental and theoretical work on $Cd(Ga,Al)_2O_4$ spinels and $Cu_3(Ta, V, Nb)Se_4$ sulvanites are reviewed. The essential first step in establishing relationships among the stoichiometry, structure and physical properties in solid-state materials is the synthesis of new compounds [39]. In 1984, F. Stone carried out structural characterization of Cadmium-Copper Gallium oxide spinels [23], which were prepared by solid-state reaction of mixtures and thereafter the unit cell parameters were deduced using X-ray powder diffractometry. Through their studies, Stone, Porta and Turner [40] noted that spinels can be prepared readily as polycrystalline solids and that the wide range of cations which can be accomodated enables close study to be made of the influence on structural chemistry of changing the chemical composition. Although X-ray powder diffraction is the most widely used technique for structural analysis of polycrystalline solids, the determination of inversion in spinels using this technique is problematic as scattering powders of the cations approach one another.

Yan and Takei [41], have reported the results of the crystal growth of single crystals of both spinel $ZnGa_2O_4$ and $CdGa_2O_4$ by the flux method. They observed that via this approach, the volatility of CdO led to the generation of Cd-poor $CdGa_2O_4$ crystals. Bouhemadou *et al.* [27], did first-principles calculations of structural and elastic properties of both $CdGa_2O_4$ and $CdAl_2O_4$ together with $CdIn_2O_4$ using the pseudo-potential plane-waves approach based on density functional theory, within the generalized gradient approximation as implemented in Cambridge Serial Total Energy Package (CASTEP) code [42]. From their observation, Cadmium dialuminium, gallium and indium oxides are wide bandgap semiconductors that are characterized by high transmissibility in the visible spectrum and possess excellent electrical properties. These properties have led to their applications in various fields such as solar cells, flat-panel displays, invisible security circuits and windshield defrosters.

Additionally, Murtaza *et al.* [43], have explored the electronic and optical properties of cubic spinels CdX_2O_4 (X = In, Ga, Al) using the modified Becke-Johnson potential based on density functional theory. Apart from computing their electronic band profile, density of states, effective masses and chemical bonding; they also explored optical properties of these ternary materials such as the dielectric constants,

refractive index, reflectivity, optical conductivity and absorption coefficient. Boujnah *et al.* [44], have also explored the optoelectronic response of spinel oxides CdX_2O_4 (X = In, Ga, Al) done using Wien2K package [45] that is based on density functional theory. They also analyzed the bandgap dependent optical parameters such as the absorption coefficient, complex dielectric function, electron-energy-loss function, complex index of refraction and reflectivity coefficient as functions of photon energy.

As stated in section 1.5, Bouhemadou *et al.* [33] calculated the structural, elastic, electronic, optical and thermodynamic properties of the cubic spinel $CdAl_2O_4$ using *ab initio* density functional theory, where they employed the full-potential augmented plane-wave plus local orbitals (FP-(L)APW + l_o) as implemented in the Wien2K package. Gibbs program was used to study the thermal effects within the quasi-harmonic Debye model. The authors also investigated as well the pressure and temperature effects on lattice constant, bulk modulus, volume expansion coefficient, heat capacities, Debye temperature for pressure and temperature in the range of 0-30 GPa and 0-1300 K, respectively.

For the case of Cu_3(Ta,V,Nb)Se_4 sulvanites; In 1961, F. Hullinger [46], prepared sulvanite analogues by substituting Nb and Ta for V; and Se and Te for S. He sintered the elements at 600 - 800 $^{\circ}$C and obtained polycrystalline samples for which he determined their lattice constants and magnetic susceptibilities. From the findings of Van Arkel and Crevecoeur that was done in 1963 [12]; the crystals of the sulvanite analogues containing Nb and Ta appeared to be of interest as modulators for visible light in that from their findings, the bandgap of these materials decreased in the substitutional sequence S $\rightarrow$ Se $\rightarrow$ Te, but increased in the sequence V $\rightarrow$ Nb $\rightarrow$ Ta.

Additionally, Lu and Ibers [47], synthesized Cu_3NbSe_4 alongside KCu_2TaSe_4 from a stoichiometric reaction of the elements at 950 $^{\circ}$C. For the case of Cu_3NbSe_4, the starting materials were loaded into a quartz tube that was subsequently evacuated to 10^{-4} Torr and sealed. The tube was then placed in a furnace that was held at 950 $^{\circ}$C for 4 days. The reaction tube was then cooled at 200 $^{\circ}$C at a rate of 4 $^{\circ}$C/hr and finally to 25 $^{\circ}$C over 2 hours. The red-orange crystals obtained were examined by the electron microprobe and confirmed to be Cu_3NbSe_4. Concerning its crystallography, Weissenberg photography indicated that Cu_3NbSe_4 crystallizes in the cubic system.

For the case of Cu_3TaSe_4, Delgado *et al.* [6], prepared Cu_3TaSe_4 structure by refining it from X-ray powder diffraction data using the Rietveld method. The sample was synthesized using the melt and annealing technique where stoichiometric quantities of Cu, Ta and Se were charged in an evacuated quartz ampoule. Thereafter the ampoule was sealed under vacuum and the fusion process was carried out inside a furnace that was heated up-to 1500 $^{\circ}$C at a rate of 20 $^{\circ}$C/hr. The ampoule was shaken using a mechanical system during all the heating process. Then, the temperature was gradually raised at the same rate up-to 850 $^{\circ}$C. The ampoule was kept at this temperature for 30 days. Finally, the sample was cooled to room temperature at a rate of 10 $^{\circ}$C/hr to ensure that the samples produced are in good thermal equilibrium. Cu_3TaSe_4 was obtained as a single phase and its structure was refined by Rietveld method using X-ray powder diffraction data.

Using similar techniques, Grima-Gallardo *et al.* [7], obtained the polycrystalline samples of Cu_3NbSe_4 and Cu_3TaSe_4 by the melt and anneal technique in which the X-ray diffraction patterns indicated that both materials are single phase. They also investigated: a) the variation with pressure of the Raman modes of Cu_3NbSe_4 and Cu_3TaSe_4; b) the optical absorption of Cu_3NbSe_4 and Cu_3TaSe_4 at ambient conditions; c) the optical absorption of Cu_3TaSe_4 at high pressure and d) the thermal transitions of Cu_3NbSe_4 and Cu_3TaSe_4. From optical absorption measurements extracted by Grima-Gallardo *et al.*, they obtained the values of the indirect and direct gap of Cu_3NbSe_4 to be 2.14 and 2.45 eV, respectively. Also, the variation of the indirect gap of Cu_3TaSe_4 under pressure in the (0-5.5) GPa range was observed, obtaining the indirect energy gap at zero pressure to be 2.43 eV and the extracted pressure coefficient

was -0.032 eV/GPa.

The above discussion on previous studies of sulvanites of interest has been from the experimental perspective. From the theoretical point of view, Peralta and Valencia-Balvin [48], have studied Cu_3XY_4 (X = Nb, V, Ta and Y = S, Se) using the first principles calculations where they explored their structural and dynamic behavior at different temperatures. They also determined the vibrational spectra of the stated sulvanites using molecular dynamics in the microcanonical ensemble.

Yuan *et al.* [14] also carried out quantitative analysis of the electronic and thermal properties of Cu_3MCh_4 (M = V, Nb, Ta; Ch = Se, Te) using the first-principles calculations in combination with the semi-classical transport theory. They obtained the highest numerical values of the dimensionless figure of merit (ZT) at 1000 K for the case of Cu_3MSe_4 to be 1.91, 2.35 and 2.03, respectively. The authors attributed the excellent thermoelectric performance to the high band-degeneracy and smaller effective mass of holes. Espinosa-García *et al.* [5], have calculated the elastic properties of the sulvanites using first-principles total energy calculations within the density functional theory along with the local density and generalized gradient approximations to extract quantities such as bulk modulus, elastic constants, Zener anisotropy factor, isotropic shear modulus and Young modulus. They further analyzed them to obtain other thermodynamic properties such as the average sound velocity and Debye temperature. From the numerical values obtained, they concluded that these sulvanites are brittle and fragile. They further calculated the electron localization function that exhibits the bonding behavior in these ternary compounds.

The geometric and electronic properties of sulvanite structured Cu_3MCh_4 (M = V, Nb, Ta; Ch = S, Se, Te) as potential photovoltaic materials have been computed by Kehoe, Scanlon and Watson [49]. This was carried out using both PBEsol+U and HSE06 methods. They reported that although these compounds have a good potential, all their fundamental gaps were indirect in nature hence could lower the open-circuit voltage leading to low efficiency of prospective devices, which is a drawback. Additionally, Espinosa-García *et al.* [50], observed that broad range of gaps and chemical stability of sulvanite compounds have made them promising materials for technological applications such as photovoltaic and transparent conductors. This motivated the authors to carry out the electronic and optical studies of the sulvanite family of compounds based on first principles approach using VASP code [51]. The calculated optical spectra at Bethe-Salpeter equation level of approximation showed that Cu_3MCh_4 (M = V, Nb, Ta; Ch = S, Se, Te) have good absorption in the visible regime of the electromagnetic spectra.

Moreover, Li *et al.* [52], carried out density functional theory simulation of the natural sulvanites Cu_3MX_4 (M = Nb, Ta; X = S, Se) as potential photocatalytic candidates. From their findings, these compounds are promising as photocatalysts in the harvesting of visible light for water splitting. The structures also showed high dynamic stabilities as confirmed by their calculated phonon dispersions and elastic constants. Further more, the band edge positions predicted indicated that these materials straddle the redox potential of water. Owing to the small average effective mass and effective separation of the photogenerated charge carriers deduced, these compounds have low chances of recombination, which in turn enhances their photocatalytic ability.

2.2 Thermoelectric materials

Thermoelectric materials, which can generate electricity from waste heat or be used as solid-state Peltier coolers, can play an important role in attaining a global sustainable energy solution.

2.2.1 Thermoelectric effects

There are three major effects of thermoelectric phenomenon namely Seebeck, Peltier and Thomson effect [53] as shown in Figure 2.1. Seebeck effect is attained when a conductor generates a voltage when subjected to temperature gradient, whereas Peltier effect refers to the temperature induced by voltage gradients, which is simply the opposite of Seebeck effect. In this study, we focused on the Seebeck effect, where heat is converted to electricity arising from the movement of charge carriers from a higher temperature to a lower temperature region producing a voltage [54].

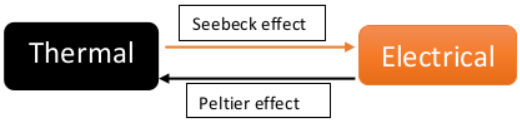

Figure 2.1: Diagrammatic representation of the thermoelectric effects.

On the other hand, Thomson effect relates the reversible thermal gradient and electric field in a homogeneous conductor. However, thermoelectric materials can be used for both cooling via the Peltier effect and electric power generation via the Seebeck effect. Thermoelectric power generation from waste heat offers a possible solution to human energy requirement through increasing energy efficiency using the existing energy-generation technologies.

2.2.2 Correlation between figure of merit and Carnot efficiency

The efficiency of a thermoelectric device is determined by the material used in making the device, and thus the current focus of research is on finding better thermoelectric materials. Therefore, efficiency of a thermoelectric device is related to the thermoelectric figure of merit [55], which dictates the coexistence of high electrical conductivity and low thermal conductivity which is an extraordinary feature [56]. The dimensionless figure of merit (ZT) is expressed as:

$$ZT = \frac{S^2\sigma T}{\kappa} = \frac{S^2\sigma T}{\kappa_e + \kappa_l}; \tag{2.2.1}$$

where S, σ, T and κ are the Seebeck coefficient, electrical conductivity, temperature in Kelvin scale and thermal conductivity respectively. Thermal conductivity is composed of the electronic and phononic contributions ($\kappa = \kappa_e + \kappa_l$). According to equation (2.2.1); S, σ and κ are all coupled with each other such that by increasing electrical conductivity and Seebeck coefficient while at the same time decreasing thermal conductivity will lead to substantial improvement in ZT. Therefore, a compromise has to be reached among these conflicting parameters so as to enhance the figure of merit, which in turn limits its value, although there is no theoretical upper limit for the figure of merit [57] and the larger the value, the better the efficiency of the thermoelectric cooler or power generator.

The three parameters (S, σ and κ) are strongly dependent on the crystal structure, electronic structure and carrier concentration of a material. Apart from high figure of merit, the material should have sound mechanical, metallurgical and thermal characteristics in order to be used in practical thermoelectric generators [58]. The shortcoming of the existing thermoelectric materials is their relatively low energy conversion efficiency [59] as illustrated below.

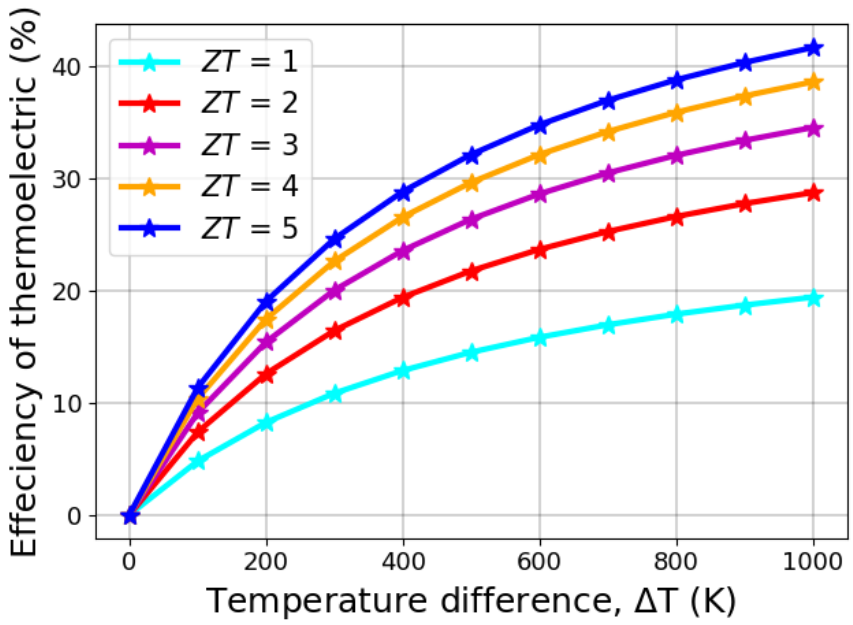

Figure 2.2: Diagramatic representation of the relationship between ZT and efficiency.

Figure 2.2 shows a direct relationship between the thermoelectric energy conversion and ZT when the cold temperature (T_c) is 300 K. Temperature of the hot part of the system is given by the sum of the temperature of cold part plus ΔT (where ΔT is temperature difference between the hot and cold region), that is $T_h = T_c + \Delta T$. It is evident that in order to attain high thermoelectric output, materials with high ZT values are mandatory. There is an increase in thermoelectric efficiency with temperature at a fixed ZT. In addition, the efficiency increases with an increase in ZT at a fixed temperature.

In practice, the most widely preferred materials in thermoelectric applications have Bismuth telluride (Bi_2Te_3) as their active component, possessing a maximum ZT value of about unity [60]. This implies that its efficiency is $\approx$ 10% at room temperature as per Figure 2.2. This signifies that a lot has to be done to discover, improve or design materials with higher ZT values in order to realize more efficient thermoelectric system.

2.3 Aspects of good thermoelectric materials

To achieve a high thermoelectric efficiency, the following aspects of materials choice should be considered:

2.3.1 Size of the band gap

An ideal thermoelectric material should not only have high figure of merit but also a wide operational temperature range. Generally, semiconductors often have high thermoelectric figure of merit attributed to their moderate Seebeck coefficients, good electrical conductivity and low thermal conductivity as compared to metallic and insulating systems. Metals have low Seebeck coefficient and high thermal

conductivity, whereas insulators have comparably high Seebeck coefficient and very low electrical conductivity, which edges them out. Thus, metallic systems are not good for thermoelectric prospects mainly because they cannot maintain thermal gradient [57], this has also been elaborated by Shakouri [61] as represented in Figure 2.3.

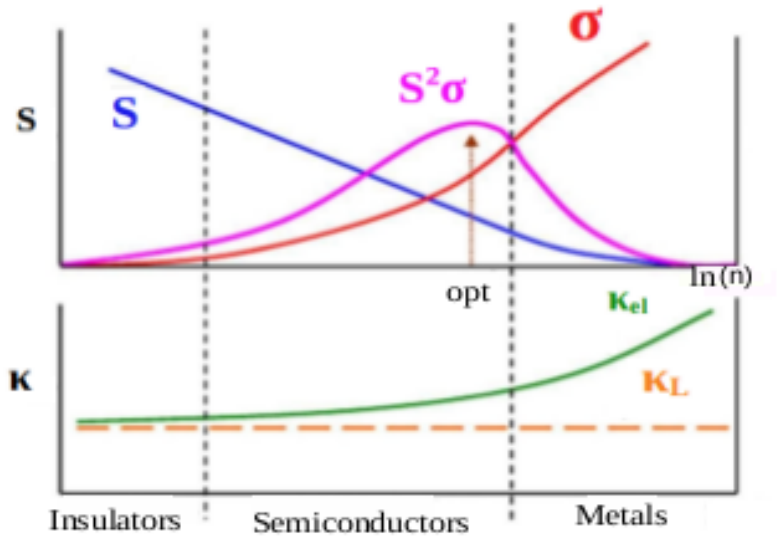

Figure 2.3: Diagrammatic representation of the optimization of the figure of merit (ZT). [61]

2.3.2 Mechanical stability

The most important criterion to gauge if a material can be used in any type of application is its stability. Though majority of thermoelectric studies have been towards the electrical and thermal properties, mechanical properties are also instrumental for their long term reliability as the thermoelectric system may be exposed to temperature oscillating environment, hence properties such as hardness, fracture, strength, elastic moduli and creep rate has to be investigated as well as their variation with respect to change in temperature, porosity, composition and grain size [62].

2.3.3 Layered crystal structures

Layered materials are preferred candidates for thermoelectric application due to their low out-of-plane thermal conductivity giving high efficiency [63]. They also provide a considerable tunability of the transport properties by being layered.

2.3.4 Cost

Bi_2Te_3 is known to be a good thermoelectric material at room temperature with ZT of about unity [64]. Its short-coming is that it is costly, because of the large amounts of expensive tellurium it con-

tains [65]. Therefore, possibility of considering cheap, non-toxic and readily available earth abundant elements/compounds is worth examining.

2.3.5 Nanostructuring

Nanostructuring may lead to an increase in the magnitude of dimensionless figure of merit relative to that of the bulk materials possibly because the thermal conductivity will most likely decrease due to phonon scattering since nanocrystalline materials have many interfaces between crystals, resulting in an increase in the power factor due to quantum confinement [66] as phonons are confined to the grain, especially if their mean free path is larger than the material grain size.

2.3.6 Complex bulk materials

Complex bulk materials such as skutterudites [67] and clathrates [68] and filled antimonides [69] possess low thermal conductivity, hence have improved ZT and efficiency. The skutterudites and clathrates are basically caged complex compounds, where the vibrations of the rattler (which is the guest atom) lowers the thermal conductivity. On the other hand, filled antimonides attain low thermal conductivity through the presence of defects or due to the high complexity of their crystal structures. Moreover, according to Pei *et al.* [70], when the primitive cell gets large, the first Brillouin zone shrinks and therefore most of the high-frequency vibrational modes are folded back as optical ones with significantly reduced velocities near zone boundaries.

2.4 Applications of thermoelectricity

Thermoelectricity is useful in the following areas either as power generators or coolers:

2.4.1 Waste heat recovery in automobiles

According to Yang *et al.*, during the internal combustion of gasoline in a vehicle, a quarter of the fuel energy is utilized in vehicle mobility and other accessories whereas the remainder ($\frac{3}{4}$) is lost in form of heat in the exhaust and coolant. Also, recall that friction and parasitic losses also comes to play [71]. To curb this, a number of car manufacturers are currently testing variety of thermoelectric generators which operates by exploiting the temperature gradient between two sides of the generator. This is aimed at scavenging some of the waste heat from exhaust and in turn using it to run the air conditioning units, lights and recharge batteries in hybrid vehicles among others. An attempt to replace the alternator in cars with a thermoelectric generator mounted on the exhaust stream is being carried out in order to improve the fuel efficiency [72].

2.4.2 Space exploration

National Aeronautics and Space Administration (NASA) spacecraft named voyager used Radioisotope Thermoelectric Generator (RTG) as power source, which utilizes the Seebeck effect in producing heat [73]. Spacecrafts are mechanized in hardware and software, which when operated by ground commanded

sequences; are capable of making detailed scientific measurements for the exploration of outer system [74]. Space provides an excellent working environment for thermoelectric generators in that the average temperature in space is about 3 K, hence acts as the cold side of the generator whereas the hot side is provided by the radioactive source (i.e strontium 90, ^{90}Sr) which emits heat as it decays. This has been applied in Apollo mission, as well as powering Cassini and voyager spacecraft millions of miles from the earth.

2.4.3 Design of thermal suits

Fire resistant clothing used by fire fighters limit the transmission of heat towards the body. Some are made of Nomex and others of polybenzimidole fiber. Moreover, physical quantities can be transformed into a readable signal using a sensor. Among various types of sensors, thermal sensors can stimulate and predict the heat flux transmitted through human bodies under hazardous fire exposure [75].

2.4.4 Portable refrigerators

A thermoelectric refrigerator has a heat transfer system and a heat exchanger with an evaporating surface and a conducting surface. A fluid flow path is provided to allow working fluid in its vapor phase to flow from the evaporating surface to the condensing surface and working fluid in its liquid phase to flow from the condensing surface to the evaporating surface [76]. In addition, niche applications for bulk thermoelectric devices which are basically small heat pumps that follows the laws of thermodynamics have been developed such as small portable refrigerators and picnic coolers [77]. Portable picnic boxes have been designed to maintain food in a refrigerated condition during its transportation and storage prior to use at a point remote from the location where it was filled [78]. In line with this, storage and transportation of vaccine in a potent state from the manufacturer to the person being immunized at a temperature of (2-8) °C poses a challenge especially in developing countries. Fortunately, through the development of solid state thermoelectric coolers, portable packages have been designed and developed to facilitate this [79].

2.4.5 Spot cooling

Climate-controlled seat systems have been developed to provide rapid seat cooling in summer and equally fast heating in the winter. Operation of sensors is also crucial in infrared imaging systems for heat-seeking missiles and night vision systems [80].

2.4.6 Thermoelectric air conditioning

Thermoelectric air conditioner consists of a pair of thermocouple structures having a pair of spaced sets of thermocouple junctions of which one is cold and the other is hot when thermoelectric current which is often in direct current (dc) form is passed through these sets in one direction, but these thermal conditions are reversed when the current is passed in the opposite direction [81]. The advantage is that thermoelectric air conditioning devices can be used in nearly all environments formerly conditioned by conventional refrigerator or cooling systems and further exhibit utility in some environments not amenable to conditioning by conventional methods [82]. However, the short coming of thermoelectric

devices in air conditioning is that large number of thermoelectric bodies and junctions are required to produce a useful heat pumping effect with presently known materials due to their low efficiency [83].

2.4.7 Sensors

The technical characteristics of sensors using Seebeck effect mainly depend on their thermoelectric properties namely Seebeck coefficient, thermal conductivity and electrical resistivity. Boyer and Cisse [84], pointed out that having an in-depth knowledge on thermoelectric data of materials is crucial in the production of sensors based on Seebeck effect such as thermocouples, thermopiles, radiation detectors, hyper frequency power sensors and electrical converters. According to Muehlbauer *et al.* [85], thermoelectric enzyme sensors have been designed that can detect heat generated by various substrates reacting selectively on their enzyme-immobilized surfaces with remarkable room temperature sensitivity. Additionally, a lot of scientific research presently is towards clean energy generation where hydrogen is perceived to be the future energy carrier. Hence expectedly, hydrogen gas sensors are required to accurately regulate hydrogen gas concentrations and alarm in case of hydrogen gas leakage, so as to ensure product safety. This is where combustible gas sensors such as stannic oxide play a crucial role in selectively detecting the presence of gases when variation in resistance crop up [86].

2.5 Hydrogen generation techniques

Figure 2.4 shows various techniques that are applicable in generating hydrogen gas, whereby water is involved [87] and are discussed briefly underneath.

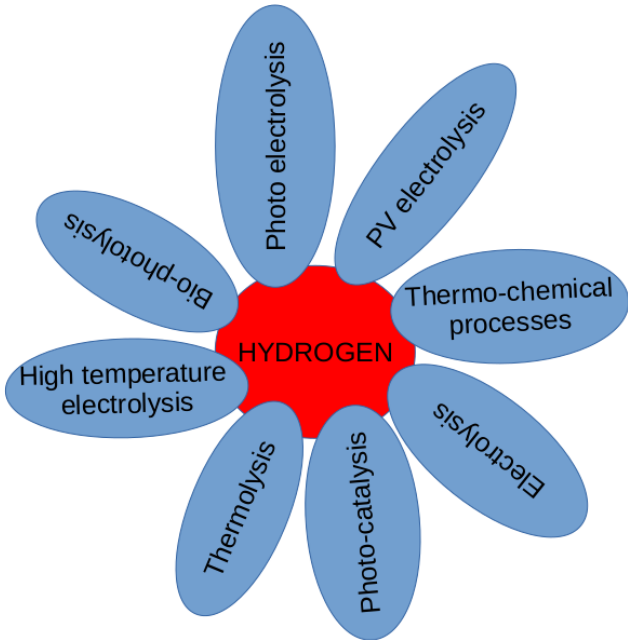

Figure 2.4: Hydrogen generation techniques that involve water.

2.5.1 Electrolysis

This is a technique that uses a direct electric current to initiate chemical reaction at the electrodes leading to decomposition of the material. Although hydrogen production via electrolysis of water from alkaline aqueous electrolytes is a well established conventional technology, its hydrogen production cost is very high [88].

2.5.2 Thermo-chemical process

Is a two-step process involving the use of metal oxide redox pair i.e Fe_3O_4/FeO, where the first thermal reduction process of Fe_3O_4 occurs at high temperature and is highly endothermic [89].

$$Fe_3O_4 \rightarrow 3FeO + \frac{1}{2}O_2; \qquad \Delta H = 319.5kJ/mol; \tag{2.5.1}$$

The next step is water decomposition process, which is slightly exothermic and occurs at a moderate temperature.

$$3FeO + H_2O \rightarrow Fe_3O_4 + H_2; \qquad \Delta H = -33.6kJ/mol; \tag{2.5.2}$$

2.5.3 PV electrolysis

In this approach, solar energy is used to power electrolysis process [90]. Basically, it is a combination of photo-voltaic cells (PV) and water electrolyzers [91]. Its short-coming is the fluctuation of output.

2.5.4 Photo electrolysis

Is the decomposition of water into hydrogen and oxygen via absorption of light in the presence of a catalytic semi-conducting electrodes such as $SrTiO_3$ immersed in an electrolyte [92].

2.5.5 Bio-photolysis

In this process, fuels are produced from biomass through Bio-conversion whereby in the presence of light, some specific micro organisms such as the green micro-algae and cyanobacteria are able to dissociate water into molecular hydrogen and oxygen [93].

2.5.6 High temperature electrolysis

In this technique, water is converted to steam using thermal energy. An oxygen ionic conductor is often used as a solid-oxide electrolyte. Dissociation of steam occurs at the cathode whereas formation of hydrogen molecules occurs at the cathode surface [94]. Its advantage is that the high temperature electrolyzer used saves the electric energy due to favorable thermodynamic and kinetic conditions [95].

2.5.7 Thermolysis

Involves the use of extreme heat to split water, but the process seems unrealistic for large scale application since it requires extremely high temperatures of over 5000 K. Moreover, separating the generated gases is problematic as it needs heat resistant membranes, which aren't easy to design or develop [96].

2.5.8 Photocatalysis

Is a phenomenon by which chemical reactions occurs in the presence of light, water and a photocatalyst material preferably a semiconductor [97]. Water decomposition by means of sunlight mimics photo-synthesis by converting water into H_2 and O_2 using inorganic photo-semiconductors that catalyze the water-splitting. The maximum efficiency achieved so far in the overall water splitting using particulate photocatalysts (5.9%) is still far from practical application (10%) [16], hence finding robust and efficient photocatalysts for water splitting is still a major challenge. In this study, we will be focusing on hydrogen generation via this approach. Thus, we carry out its systematic probe as discussed below.

2.6 Rationale of photocatalysis

The word photocatalysis is of Greek origin and is composed of two parts: the prefix "photo" (phos ⇒ light) and the word "catalysis" (katalyo ⇒ break apart or decompose) [17]. IUPAC defines photo-catalysis as 'change in the rate of a chemical reaction or its initiation under the action of ultraviolet, visible or infrared radiation in the presence of a substance'. It is a multi-step process that involves the acceleration of a photoreaction in the presence of a catalyst, where the latter is a material that speeds up reaction without being consumed. Since it involves sunlight and water that are fortunately abundant and essentially inexhaustible, this approach has attracted substantial interest over the past half century as it has the potential to meet the growing global energy demand, mitigate greenhouse gas emission, and provide a solution to the concerns about sustainable energy supplies [98]. Photocatalysts absorb light quanta and are involved in the chemical transformations of the reaction participants.

Figure 2.5 shows the effect of a catalyst in a chemical reaction, whereby it simply reduces the activation energy by providing an alternative reaction pathway with a low activation energy than the non-catalyzed mechanism. In Figure 2.5, G denotes the Gibbs free energy, whereas E1 and E2 denotes activation energy for non-catalyzed and catalyzed mechanisms respectively.

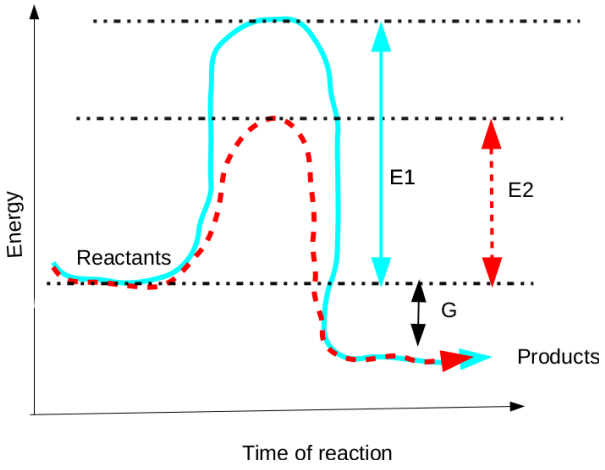

Figure 2.5: Reaction energy diagram.

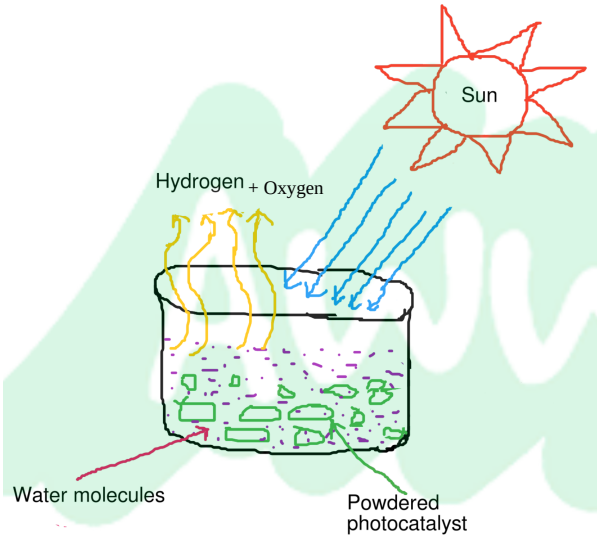

Figure 2.6: Water splitting cartoon.

Figure 2.6, shows water splitting cartoon; whereby upon interaction with light in the presence of a suitable powdered photocatalyst, water molecules are broken down to release hydrogen and oxygen. In some instances, co-catalysts are used to minimize the over-potentials and thus minimizing the energy loss in the reactions [99]. The difference between a photocatalyst and co-catalyst is that a catalyst is an independent entity where both absorptions of light and reaction occur, while the co-catalyst cannot absorb light on its own and acts as a support to the catalyst so as to accelerate the reaction [100].

Basically, there are two types of photocatalysis namely homogeneous photocatalysis where the reactant and the photocatalyst exist in the same phase and heterogeneous photocatalysis where the catalyst is in a different phase from the reactants. In this study, we are interested in heterogeneous photocatalysis because heterogeneous catalysts have some advantages over homogeneous catalysts due to the ease of separation of catalysts from the reaction products, applicability to continuous chemical industry and recyclability [101]. Additionally, most common heterogeneous photocatalysts are transition metal oxides and semiconductors that have unique characteristics. In heterogeneous photocatalysis, the catalytic reaction is initiated by excited electrons and holes that are generated by the absorption of photons in a semiconducting material serving as a photocatalyst [102].

2.6.1 Water splitting process

The photocatalytic water-splitting involves two half-reactions: the photo-oxidation of water to form oxygen that occurs in valence band and the photo-reduction of protons to form hydrogen that occurs in conduction band provided the band gap energy of the photocatalyst is greater than 1.23 eV, thus the process cannot occur spontaneously. This is shown in Figure 2.7.

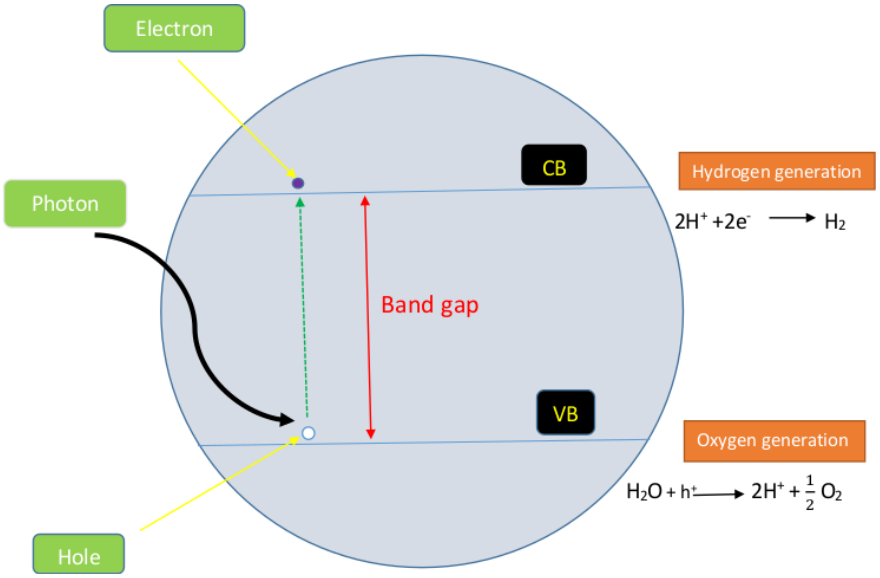

Figure 2.7: Water splitting process.

Inspired by the pioneering work of Fujishima and Honda in 1972 [103] which indicated that hydrogen production through water splitting was possible using TiO_2, photocatalysis has become a vibrant multi-disciplinary research topic cutting across fields such as semiconductor physics, surface science, physical and photo chemistry, material science and chemical engineering.

Maeda *et al.* [104] proposed a three step water splitting reaction on a semiconducting photocatalyst whereby the photocatalyst absorbs photon energy greater than band gap of the material and generates photoexcited electron-hole pairs in the bulk, photoexcited carriers then separate and move to the surface without recombination, where the adsorbed species are then reduced and oxidized by the photoexcited electrons and holes to produce hydrogen and oxygen respectively.

2.6.2 Comparison between hydrogen and electricity as energy carriers

Two major possible sources of energy to humanity are hydrogen and electricity. When compared, hydrogen has the following preferences than electricity; it has good energy conversion effectiveness since the chemical energy stored in the H-H bond is easily released when it combines with oxygen yielding water as the only product, it is abundant and has a range of possible storage options such as in gas or liquid form or even be absorbed in metal hydrides, ease of transportation over long distances, conversion onto a variety of fuels through many diverse reactions, ability to eliminate the environmental harms such as shock, high gravimetric energy density and generates almost no green house gas except in rare cases where oxygen produced reacts with nitrogen present in air to form nitrous oxides. For the above mentioned reasons, hydrogen is a competent and safe energy carrier [87], although presently electricity is the most common energy carrier. It is also worth mentioning the relationship that exists between photovoltaics, photoelectrochemical cells and photocatalysts in that they share common physical mechanisms in the initial stages of energy conversion. Photon absorption occurs leading to production of electronically excited states consisting of electron-hole pairs. The electron-hole pairs then separate and move resulting in production of either current or fuel in the subsequent steps [105].

2.7 Properties of a good photocatalytic material

The following are conditions to be fulfilled by a material for effecient water splitting in the presence of a photon:

2.7.1 Size of the band gap

A good photocatalytic material should have an appropriate band gap, this is because water splitting into H_2 and O_2 is an uphill reaction, hence it requires standard Gibbs free energy change of $+237$ KJ/mol or 1.23 eV. According to Navarro *et al.* [16], solar energy conversion gives rise to energy loss, which in turn increases the optimal band gap for high performance photocatalysts from the theoretical value of 1.23 eV to around 2 eV for maximum utilization of the solar energy [106]. Besides the energy loss, there is an activation barrier in the charge-transfer process between photocatalysts and water molecules, necessitating a photon energy greater than the band gap of the photocatalyst to drive the overall water splitting reaction at reasonable reaction rates [104].

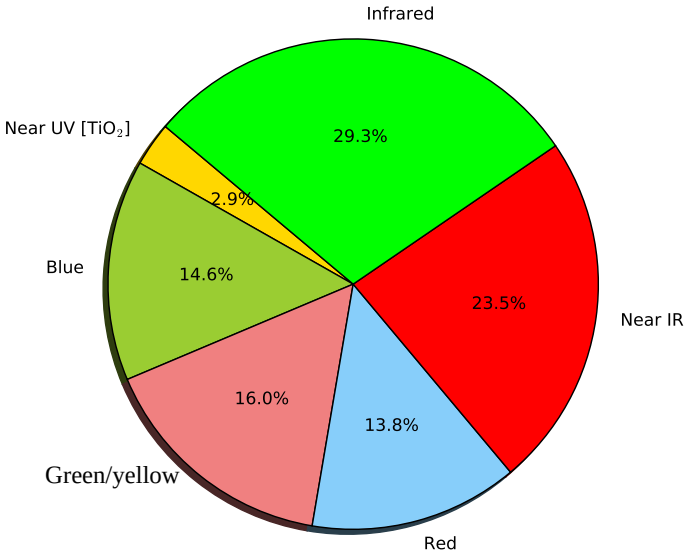

Figure 2.8: Solar energy distribution.

Figure 2.8 shows a pie chart representing percentage energy distribution of terrestrial solar spectrum when the sun is at Zenith angle of 49.19 ° (AM 1.5). It is evident that a photocatalytic material whose wavelength lies in the visible range (between 400 nm and 700 nm) are preferred for efficient absorption of solar spectrum, which translates to an improved efficiency in converting solar to chemical energy (H_2) [16].

Note that, direct water splitting in absence of a photocatalyst cannot be achieved by sunlight because the water molecule cannot be electronically excited by sunlight photons [107]. For the bulk part of the solar spectrum consisting of visible light whose energy range is (1.65 - 3.1) eV, primary goal in photocatalytic water splitting is to efficiently utilize the visible light to achieve the photocatalytic reaction [108]. Wide band gap semiconductors can also be tuned by doping, where foreign elements are introduced into the parent photocatalyst without giving rise to a new crystallographic forms, phases or structures and the

aim is to enhance the net separation of photogenerated charges and thereby harness efficiently the wide visible-light component of the solar spectrum [109].

2.7.2 Location of the band edges

The band edges should be well-positioned relative to the water redox levels. Overall photocatalytic water-splitting process is energetically favorable only if the conduction band edge is more negative than the hydrogen reduction potential whereas the valence band edge is more positive than the oxidation potential of water [110]. Otherwise half reaction occur if one band edge condition is met or no photocatalytic reaction occur if neither of the band edge conditions is fulfilled. Photocatalysts that are active only for half reactions of water splitting can be employed for construction of the two-photon photocatalysts system commonly referred to as Z-scheme water splitting [111]. The idea of Z-scheme water splitting is attained by linking two photo-systems and was first proposed by Bard in 1979 [112]. In brief, the process of Z-scheme photocatalysis entails the following: Oxygen evolution photocatalyst (OEP) injects electrons to hole acceptors; hydrogen evolution photocatalyst (HEP) accepts electrons from donors and eventually the electron mediator (EM) provides an electron relay system with suitable potentials [98].

2.7.3 Charge carrier mobility

A good photocatalytic material should possess high carrier mobility to ensure the electrons and holes reach the surface and reduce or oxidize the targets before recombining [113]. The electron-hole recombination ($h^+ + e^- \rightarrow$ heat) needs to be reduced so as to improve the quantum yield of photocatalysts, by minimizing the loss of the absorbed light as heat. In some instances, suitable scavenger or a surface defect state is crucial to trap the electron or hole throughout the process so as to prevent recombination. Additionally, on a photocatalyst surface, the distances between the H_2 and O_2 evolution sites are very important, in that if they are in a very close proximity there is a high chance of them reacting back to produce water [114].

2.7.4 Chemical and structural stability

Photocatalyst should be thermally and chemically stable in water environment. It should have a high chemical and structural stability under irradiation. A large group of photocatalysts with suitable semiconducting properties for solar energy conversion such as cadmium sulfide and gallium phosphide are unstable in water oxidation reaction because their anions are more susceptible to oxidation than water, causing their degradation [16]. Photocorrosion is considered to be the main reason causing poor photocatalytic stability in metal sulfides, though it can be suppressed by applying a suitable sacrificial reagent [115]. In addition, some of the semiconductors undergo photocorrosion induced by H^+ formed upon irradiation [116], although the photocorrosion menace can be controlled by covering the photocatalyst using a protective shield.

2.7.5 Recyclability

Recyclability of the material should also be considered. This is because the operating cost of the photocatalytic reaction is linked to re-usability, since most photocatalyst are employed once without being recycled.

2.7.6 Synthesizability

Materials which are not stable (metastable), pose a challenge in photocatalyst synthesis if they are prone to dissociate. The decomposition energies, that is cohesive and formation energies provide an indicator for the synthesizability of the photocatalytic compounds considered in this study. This is also supported by the fact that all the sulvanites of interest have already been synthesized experimentally, as discussed in section 1.4 and 2.1.

2.7.7 Abundance

The use of the earth abundant elements like copper, niobium, tantalum, vanadium and selenium as components of the photocatalytic materials would lead to affordable photocatalysts for practical use. Abundance and cost of the materials will consequently dictate the suitability of a feasible photocatalytic material for large scale production.

2.7.8 Particle morphology

While studying on morphologies of zinc oxide particles and their effects on photocatalysis, Haneda and Di [117] concluded that morphology of ZnO particles is very sensitive to the preparation methods and conditions, which also depends on crystallinity. Further, Testino *et al.* [118], noted that there is a possibility of controlling the photocatalytic activity of TiO_2 nanoparticles by tailoring their crystalline structure, morphology and surface chemistry since the morphology of crystalline surfaces is directly related to the orientation and temperature dependent free energy of the surface under the conditions of thermodynamic equilibrium [119].

Additionally, morphology control of photocatalysis has been considered to be one of the most promising avenues to improve the photocatalytic properties. This is justified by the fact that photocatalytic reactions are basically surface-based processes, hence photocatalytic efficiency is closely related to the particle morphology and micro-structure of photocatalytic materials [120]. Surface is like a static substrate upon which the process of growth and reaction occur, though it often participates actively in these processes via rearrangements in structure [121].

2.7.9 Phase purity

A pure substance does not have to be strictly a single element or compound. Even a mixture of two or more phases of a pure substance is pure provided the chemical composition of all the phases is the same [122]. For the case of TiO_2, Yu *et al.* [123] found out that the composite of two phases of titania (that is, anatase and brookite) gives an enhanced photocatalytic activity since it suppresses the recombination of photogenerated charge carriers. In this regard, many studies have focused on the development of materials suitable for water splitting within the visible regime of electromagnetic spectrum by addressing the light absorption, band edge position, crystallographic quality, particle morphology and phase purity [124].

2.7.10 Selectivity and activity

These two attributes are worth exploring, the selectivity of a reaction is the fraction of the starting material that is converted to the desired product. Activity is a measure of how fast one or more reactions proceed in the presence of the catalyst. Designing the catalysts with higher activity, selectivity, and stability is the key topics of heterogeneous catalysis. Concisely, it is a challenge of great importance to determine as well as design new semiconducting materials that are efficient, stable and abundant [125].

Although doping of wide band gap semiconductors such as TiO_2 may help tailor its gap, doping might introduce defect sites or level traps that acts as recombination centers leading to low quantum yield. Thus, the most reliable candidates for visible light photocatalysts would be single phase metal oxides with narrow band gap [126]. In contrast to cationic doping, the anionic replacement normally results in fewer recombination centers, hence more effective for enhancing photocatalytic activity [107]. Although TiO_2 absorbs light only in the ultraviolet region, it is the most promising material so far for both fundamental research and practical applications due to its high photoreactivity, economical cost, non-toxicity, photo-stability as well as biological and chemical inertness [127]. Roy *et al.* [128] realized that low solar photocatalytic efficiency is not associated with light absorption but more likely with charge transfer kinetics to monitor generation, separation and motion of charge carriers.

2.8 Applications of photocatalysis

Apart from clean energy generation, photocatalysis is essential in various applications such as catalyzing the breakdown of bio-resistant organic contaminants, water disinfection, killing of cancerous cells, nitrogen fixation, design of self-cleaning surfaces, clean-up of oil spills and fabrication of mosquito traps amongst others as deliberated shortly underneath.

2.8.1 Clean energy production

The disadvantages of solar energy such as low energy density, unstable intensity and discontinousness propelled scientific community to think of possible economical way of converting solar energy to chemical energy to enhance its utilization. A great deal of research on the conversion of solar energy to chemical energy has been directed towards the development of splitting water into hydrogen and oxygen [116]. Photocatalytic hydrogen production has been perceived as a potential solution to address excessive utilization, limited reserves and negative issues related to fossil fuels of which bulk part of hydrogen is produced through steam reforming of methane [129] ($CH_4 + H_2O \rightarrow CO + 3H_2$), producing green house gas that triggers global warming. Currently, the rate of increase in carbon dioxide concentration via simulation indicates that the average global temperature will increase by about 6 °C before the end of the current century [128], which pose adverse global environmental risk to future generation. Moreover, an increase in fossil fuel energy consumption translates to an increase in pollution, implying that more resources will be spend on pollution control rather raising the living standards of the society [130].

2.8.2 Degradation of bio-resistant contaminants

Apart from hydrogen generation, photocatalysts like monoclinic Bi_2O_4 drive a powerful oxidation process to break down various bioresistant organic contaminants such as dyes and bacteria when exposed to

light [131]. Moreover, rapid industrialization results in immense increase of organic pollutants into aquatic habitats posing a risk since most are non-biodegradable. Photocatalytic degradation of these pollutants is an attractive solution [132]. In addition, photocatalytic oxidation of organic compounds is of considerable interest for environmental applications and in particular for control and elimination of hazardous wastes [133].

2.8.3 Water disinfection

According to Ireland *et al* [134], TiO_2 photocatalysis is a viable process for disinfection of bacteria in water treatment system. This helps curb the spread of waterborne infections.

2.8.4 Inactivation of cancerous cells

Ruxiong *et al.* [135], noted that under light irradiation, titania particles have a distinct cell killing effect *in vitro* and a significant anti-tumor effect *in vivo*, whereas in the absence of light, titania particles depicted no effect on cell survival *in vitro* and no effect on growth of tumor *in vivo*. Furthermore, according to Robertson *et al.* [136], when common bacterial pathogens (that is *Escherichia coli*, *Salmonella enterica serovar* Enteritidis and *Pseudomonas aeruginosa*) were exposed to TiO_2 and UVA light, the bacterial number decreased substantially.

2.8.5 Nitrogen fixation

This is a process by which the nitrogen present in the air is converted to ammonia (NH_3) or related nitrogenous compounds. This process is biologically crucial in that most organisms are in a position to metabolize ammonia but few can metabolize dinitrogen (N_2) [137]. Hence, photocatalytic reduction of molecular nitrogen to ammonia has important economic potential as an alternative to the Haber process. This was investigated by Khan *et al.* [138], where they carried out photocatalytic reduction of dinitrogen to ammonia in a surface-modified semiconductor particulate system containing $Pt/TiO_2/RuO_2$ semiconductor powder.

2.8.6 Clean-up of oil spills

Titania is known to photo-assist the oxidation of organic pollutants in water by dioxygen. Non-catalytic photo-oxidation of crude oil on salt water eliminates part of the near-UV and visible absorbing polycyclic aromatic hydrocarbons of which some are carcinogens. The short coming is that it produces potentially toxic compounds (i.e phenols) which may polymerize upon further oxidation to polymeric tars, which are resistant to bio-degradation. On the other hand, TiO_2-photo assisted oxidation process not only eliminates polycyclic aromatics at an increased rate, but also eliminates phenols [139].

2.8.7 Self-cleaning surfaces

Photocatalysis taps the ability of some photocatalyst like TiO_2 to decompose organic contaminants when exposed to UV light, which in turn translates to reduced maintenance cost [140].

2.8.8 Design of insect traps

Mosquito trap with an air cleaning function is designed to be composed of the ultra-violet (UV) ray mosquito-enticing lamp which emits UV light of wavelength (340 - 380) nm, the fan, and the optical catalyst-coated layer. This ensures that the mosquitoes are attracted and killed only by the operation of the fan, thereby solving the drawbacks posed by the preceding mosquito trap techniques that used the high voltage. The device also sterilizes viruses drifting in the air, using the mosquitoes as media by use of the photochemical reaction of the photocatalyst (mainly TiO_2), hence preventing infection of people and domestic animal due to the viruses [141].

3

THEORETICAL FRAMEWORK

Although this work is based on density functional theory (DFT), most of the fundamental principles of DFT are not discussed in details since the same has been broadly elaborated in our previous work [142]. Detailed readers are also referred to the paper written by Hohenberg and Kohn in 1964 [143]. For our case, only a flavor of DFT that is directly related to current study is considered herein, which is mainly pertinent to the lattice dynamics and the surface aspect of the study. Therefore, we briefly discuss how one can predict the band edge position of a material computationally using the Mulliken analysis and the band gap center approach, in order to ascertain its applicability in photocatalysis. We also discuss the surface properties of a material shortly such as the surface models, high and low index surfaces, surface energy, work function as well as charge decomposition. Boltzmann transport equations are also discussed along with the relationship between kinetic coefficients and effective mass in relation to Seebeck coefficient, which is an important measure of performance of a thermoelectric material.

3.1 Band edge prediction techniques

Information about the band edge position provides the first hand test that a material must fulfill, to be a potentially effective photocatalyst [105]. There are two common techniques that are used in *ab initio* studies to predict the location of band edges of a material. These techniques are namely the Mulliken analysis approach and the band gap center approach as discussed below.

3.1.1 Mulliken analysis approach

In this technique, the two main ingredients required in order to determine the location of the band edges namely the conduction band edge position (E_{CB}) and the valence edge position (E_{VB}) are the absolute electronegativities and the optical gap ($E_g^{Optical}$) of the potential compounds. Additionally, the following empirical formulas are often used to calculate band edge positions [144];

$$E_{VB} = \chi - E_e + \frac{1}{2}E_g^{Optical}; \tag{3.1.1}$$

$$E_{CB} = E_{VB} - E_g^{Optical}; \tag{3.1.2}$$

where E_e in equation (3.1.1) refers to the energy of free electrons on the standard hydrogen scale, the Fermi level of Normal Hydrogen Electrode (NHE) at 25°C is 4.5 eV with respect to the vacuum level. χ

is the absolute electronegativity of the semiconductor under study, which is expressed as the geometric mean of the electronegativities of the isolated atomic components. These are obtained from Pearson's table of absolute electronegativities [145]. For Cu_3QSe_4, the absolute electronegativity was calculated as follows;

$$\chi = \left[\chi_{\mathrm{Cu}}^{3} \times \chi_{\mathrm{Q}} \times \chi_{\mathrm{Se}}^{4}\right]^{\frac{1}{8}}. \tag{3.1.3}$$

The information about electronegativity can also be applied in computing the ionic character of a material, which is a quantity based on electronegativity difference between the constituent atoms. Linus Pauling proposed an empirical relationship which relates the percentage ionic character in a bond to the electronegativity difference ($\Delta\chi$) as [146];

$$\text{Percentage ionic character} = \left[1 - e^{-(\frac{\Delta\chi}{2})^2}\right] \times 100\%; \tag{3.1.4}$$

such that for a compound consisting of elements A and B, equation (3.1.4) can be expressed as;

$$\%\ \text{ionic character} = \left[1 - e^{-0.25(\chi_{\mathrm{A}} - \chi_{\mathrm{B}})^2}\right] \times 100\%. \tag{3.1.5}$$

Customarily, systems which have ionic character of about (20-30)$\%$ with suitable positions of the valence and conduction band edges are considered to be appropriate for water splitting reactions [147]. A bond's percent ionic character is the amount of electron sharing between two atoms; limited electron sharing corresponds with a high percent ionic character. A covalent bond with equal sharing of the charge density has 0% ionic character, whereas a perfect ionic bond would of course have 100% ionic character.

3.1.2 Band gap center approach

Apart from using the Mulliken analysis to computationally predict band edges, one can as well apply the band gap center technique, which taps the ability of the exact Kohn-Sham band structure to predict accurately the center of the fundamental energy gap relative to the vacuum potential [148]. To calculate band edges via this method, we need to first determine the reference vacuum potential, which is obtained by calculating the electrostatic potential of the material at DFT level of approximation. The optical gap obtained at Bethe Salpeter Equation (BSE) level of approximation is then applied to compute the conduction band minima and the valence band maxima energy according to equation (3.1.6) and (3.1.7) [149].

$$E_{\mathrm{CBM}} = E_{\mathrm{BGC}} + \frac{1}{2}E_g; \tag{3.1.6}$$

$$E_{\mathrm{VBM}} = E_{\mathrm{BGC}} - \frac{1}{2}E_g. \tag{3.1.7}$$

In this approach, the positions of the band edges relative to the vacuum potential were determined by combining surface and bulk calculations. Essentially, if we add equation (3.1.6) and (3.1.7), we establish that the band gap center (BGC) is halfway between the valence band maxima (VBM) and the conduction band minima (CBM). Therefore, the computed E_{CBM} and E_{VBM} are then compared to the redox potential of water as well as those obtained from Mulliken analysis. The ability of a material to perform redox reaction at its surface depends on the position of its band edges relative to the free energies of the reactions of interest. The reactions are thermodynamically favorable if their free energies are located within the band gap energy region.

3.2 Surface properties

Surfaces are generated by cutting a bulk crystal. In principle, a surface possess significantly different properties to the bulk, because when a surface is created, the bulk symmetry is broken and hence there will be forces on the surface atoms. To some extent, surface properties differ from bulk due to lack of interactions in one direction which can cause relaxations and sometimes reconstructions of the surface. The created surface is the point where molecules from the gas phase or a liquid comes into contact with the material. The surface properties are important for the understanding of various surface phenomena such as adsorption, oxidation, corrosion, catalysis and crystal growth [150]. Usually, for the same material, there is a strong variation on photocatalytic activities with respect to crystallographic surface orientation [151].

3.2.1 Surface models

Generally, two surface models are often used to study the surface behavior of materials namely the cluster model and the supercell model. The cluster model treats the surface as a small isolated cluster of atoms, one facet of which has the same symmetry and atomic arrangement as the crystal surface intended to study. This model best suits materials with localized wavefunctions such as the insulating systems. It describes only a limited cluster of the surface atoms. From *ab initio* perspective, supercell model characterize metallic surfaces with delocalized valence wavefunctions much better. The short-coming of the cluster approach relative to supercell approach is that it has spurious perturbation arising from the abrupt truncation of the infinite lattice due to relatively small number of atoms considered [152]. Contrarily, the slab in the supercell is infinite and periodic in the directions parallel to the surface, but finite in the direction perpendicular to the surface. Slab calculations use periodic boundary conditions to model extended surfaces. The slab model avoids the electronic structure artifacts that are sometimes encountered in the calculations where cluster model is used [153].

The main parameters that describe the slab model are the cleavage plane, thickness/number of layers of the slab, thickness of the vacuum and the lateral dimensions of the periodic unit cell. The slab thickness is the number of bulk units repeated in the z-direction and the number of layers needed to converge the surface energy varies with the surface orientation. A vacuum region is inserted into the supercell to separate the periodic replicas. Preferably, the vacuum thickness should be large enough to avoid surfaces of constructive slabs interacting with each other and the thickness of the slab should also be thick enough to avoid interaction between the two surfaces of one slab. This in turn ensures that the middle layers of the slab exhibits bulk-like properties [154]. The slab is placed within a 3D periodic supercell and a vacuum layer is added on either side of the slab to mimic the 2D periodicity of an actual surface [155]. Like all supercells, the slab supercell must be a Bravais lattice and is often of different Bravais lattice to that of the parent crystal i.e parent Cu_3TaSe_4 is cubic whereas (100) slab is described in tetragonal cell. In our study, we applied the supercell model. Figure 3.1 and 3.2 give diagrammatic representation of supercell and cluster model of Cu_3TaSe_4, respectively. The red atoms represents Ta, blue ones are for Cu and green are for Se.

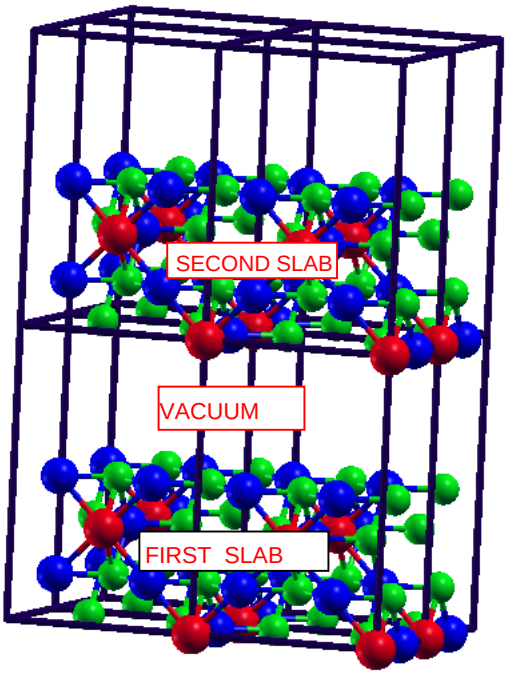

Figure 3.1: Slab surface model.

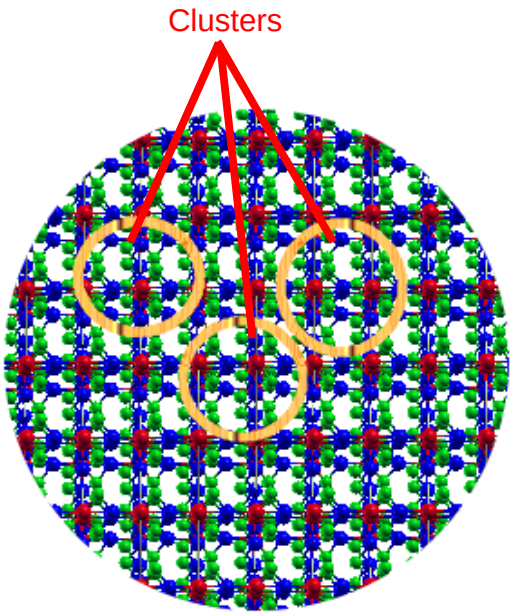

Figure 3.2: Cluster surface model.

3.2.2 High and low index surfaces

A low index plane is one where the sum of the three components is small. Since a facet or a surface of a crystal is a plane, it can be described using Miller indices. We can then classify the ideal surfaces of cubic crystals into two groups namely; the low Miller index (flat) surfaces i.e 100, 110 and 111 surfaces and the high Miller index (stepped) surfaces [156]. Stepped surfaces are often produced by cutting a single crystal at a small angle away from a low Miller indexed crystal plane [157]. The 100, 110 and 111 surfaces are so-called low index surfaces of a cubic crystal system since their miller indices are small in number (0 or 1) and are symmetry-distinct as presented diagrammatically in Figure 3.3 and 3.4. In reality, one may slice a crystal along infinite directions or planes and each possess unique arrangement of atoms at the surface. Obviously, due to symmetry considerations, only three low index orientations (that is 100, 110 and 111) are often considered for cubic crystals and to distinguish them, the stated notations are used. Contrarily, the stepped surfaces can exhibit significantly different properties compared to flat surfaces due to the effect of defects. It should be noted that although the investigation of low index surface can generate a wealth of information on surface properties of a material, in reality, a surface possess additional features like steps, kinks or vacancies [158].

Nonetheless, the vast majority of surface calculations are performed using flat surfaces. This is partially because these surfaces tend to have the lowest surface energies with a tendency to have favorable surface coordination, hence likely to be observed experimentally. The surface energy is associated with the disruption of chemical bonds at the surface. When a surface is formed, the number of nearest neighbors of external layer atoms decreases. This breaks the symmetry of distribution of masses and forces that act on a surface atom from the other atoms [159]. Therefore, less number of atomic bonds are cut in creating a low-index surface than high index ones, provided reconstruction is minimal [160].

On the other hand, high index planes have a high surface energy due to their large density of atomic steps, ledges and kinks [161]. In addition, flat surfaces have small unit cells, hence computationally affordable.

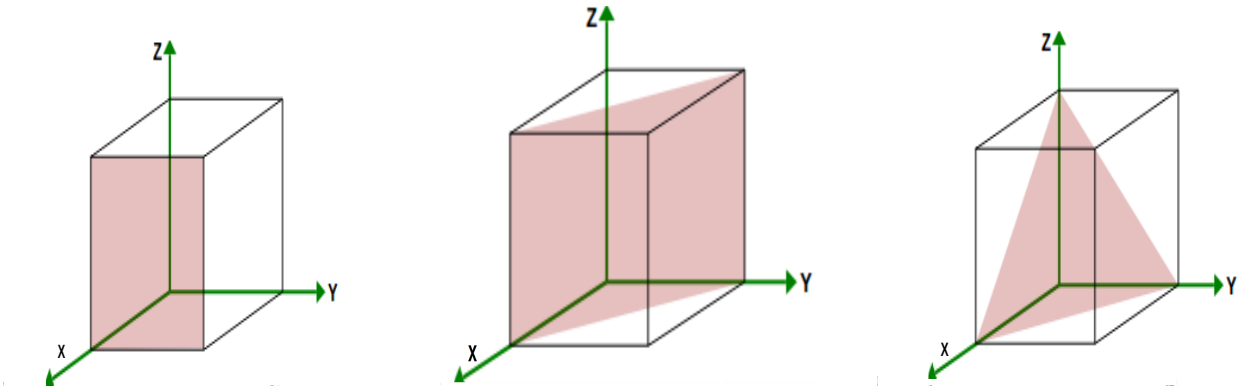

(a) 100 **(b)** 110 **(c)** 111

Figure 3.3: Low index orientation for a simple cubic crystal structure.

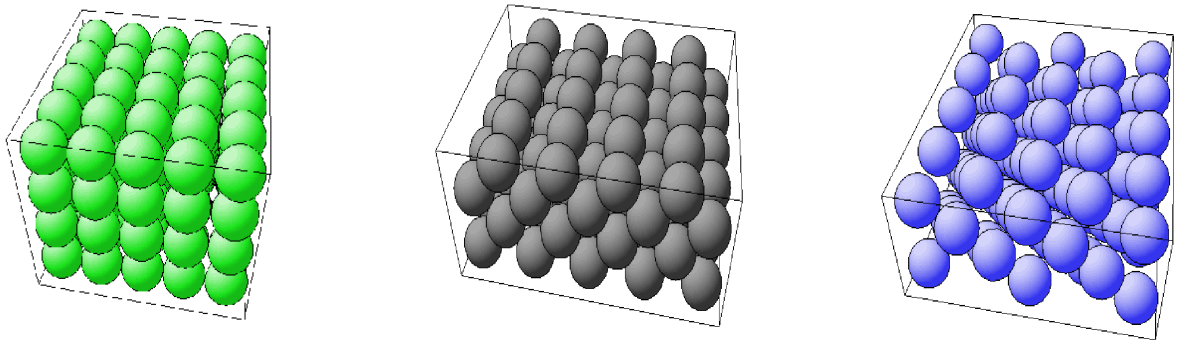

(a) 100 **(b)** 110 **(c)** 111

Figure 3.4: Surface models for a simple cubic crystal structure obtained from surface explorer for low index facets.

3.2.3 Surface energy

Surface energy is the amount of energy required to create a surface (hkl) from the bulk material and is often represented by the symbol γ. It is a crucial parameter that acts as a measure of the excess of surface atoms due to a variety of factors such as broken bonds yielding un-coordinated atoms. Surface energy is always a positive quantity. However, when it is negative, it indicates the material is unstable. It differs from one surface plane to another, hence can be used to establish the relative stability of different surface facets [162]. Besides using the surface energy as a descriptor of surface stability, the stability of surfaces can be estimated as well via evaluation of the number of broken bonds per unit area, electrostatic considerations or electron counting rules [163]. The lower the number of broken bonds in forming a surface, the lower the surface energy.

Surfaces with high surface energy, have a stronger tendency to relax and/or reconstruct than surfaces with low surface energy [164]. It is important that the bulk and surface calculations are done with the

same accuracy as γ involves comparing energy from the supercells of different shapes and sizes, hence one has to be cautious so as to ensure that equivalent computational parameters i.e cut-off energy are used. The energy of the terminated surface of a solid material is always higher than that of the bulk and this energy difference is defined as the surface energy [165]. From the above definition, surface energy of a given slab can be computed using equation (3.2.1) [149].

$$\gamma = \frac{1}{2\mathrm{A}} \left[E_{\mathrm{slab}} - \frac{N_{\mathrm{s}}}{N_{\mathrm{b}}} E_{\mathrm{bulk}} \right]; \tag{3.2.1}$$

where E_{slab} is the total energy of the stoichiometric slab under consideration, E_{bulk} is the total energy of the bulk, N_{s} (N_{b}) is the number of atoms in the slab (bulk), whereas A is the unit surface area of the slab. Note that the above formula is only applicable to surfaces having stoichiometric slabs. For the case of non-stoichiometric, their surface energy cannot be defined precisely using equation (3.2.1). Also, a high surface area is an advantage in terms of a greater concentration of the active sites per square meter and this generally leads to higher reactivity. The factor 2 comes to play since we are considering the upper and the lower side of the slab that are symmetric. For non-stoichiometric slabs or surfaces containing adatoms, the surface energy becomes a function of the chemical potential and of the number of the additional atoms [166]. Basically, the surface energy is the solid analog of the surface tension of a liquid [167]. In this study, the dipole moment induced by the asymmetric slab geometry with different upper and lower surfaces was taken into account by applying the dipole correction in the *z*-direction [166].

It is difficult to obtain experimental surface energy as well as their orientation dependence since various factors such as presence of impurities cannot be totally eliminated, though can be minimized. In this regard, careful calculations based on modern first principle methods plays a crucial role. Most experimental data on absolute surface energies come from surface tension measurement in the liquid phase extrapolated to zero temperature [168]. Thus, accurate computation of surface energy is critical as it is a major driving force determining the morphology and composition of surfaces, interfaces and nanoparticles [162]. Since there is no prior information on stable surface structures of CuQSe4 sulvanites, we considered only the stoichiometric surfaces. Ordinarily, before carrying out an in-depth catalytic study on a material, it is crucial to look at its surface properties at the atomic scale as it is essential in order to characterize the exposed surface that is photocatalytically relevant [169]. Furthermore, since surface properties are orientation-dependent, we first study the low-index surfaces of $\mathrm{Cu_3QSe_4}$ using periodic DFT approach in order to characterize and identify the most stable surface that is pertinent to catalysis.

3.2.4 Work function

The work function, normally denoted by Φ, is the energy required to move an electron from the Fermi level of a material to a point that is infinitely far away in a vacuum and can be expressed as [149]

$$\Phi = E_{\mathrm{vac}} - E_{\mathrm{F}}. \tag{3.2.2}$$

It can also be defined as the minimum energy required for an electron to escape from a solid through a certain surface orientation and it is orientation-dependent [170]. Hence, we have to first determine the most stable surface based on the surface energy, as that is the surface that will be in contact with the vacuum. Therefore, work function represents the energy barrier to free space that prevents an electron at the Fermi level from escaping the solid and consist of two components, a bulk component and a surface component [171]. Ordinarily, the work function and surface energies are very crucial entities required to fully characterize a surface.

3.3 Charge density decomposition

Charge density decomposition provides us with an opportunity to dissociate the charge or energy of a material into contributions from the individual atoms, which in turn provides useful information about the properties of the material [172]. According to quantum mechanical theory, atomic charges in solids or molecules cannot be defined or characterized since they are not observables. Hence, the output of quantum mechanical calculations is a continuous electronic charge density and is not clear how one should partition electrons amongst the fragments of the system such as atoms or molecules [173]. Various schemes have been proposed of which some are based on the electronic orbitals and others are based on the charge density as shown in Figure 3.5, where we have electronic orbital based and charge density based techniques of charge decomposition, as discussed shortly underneath.

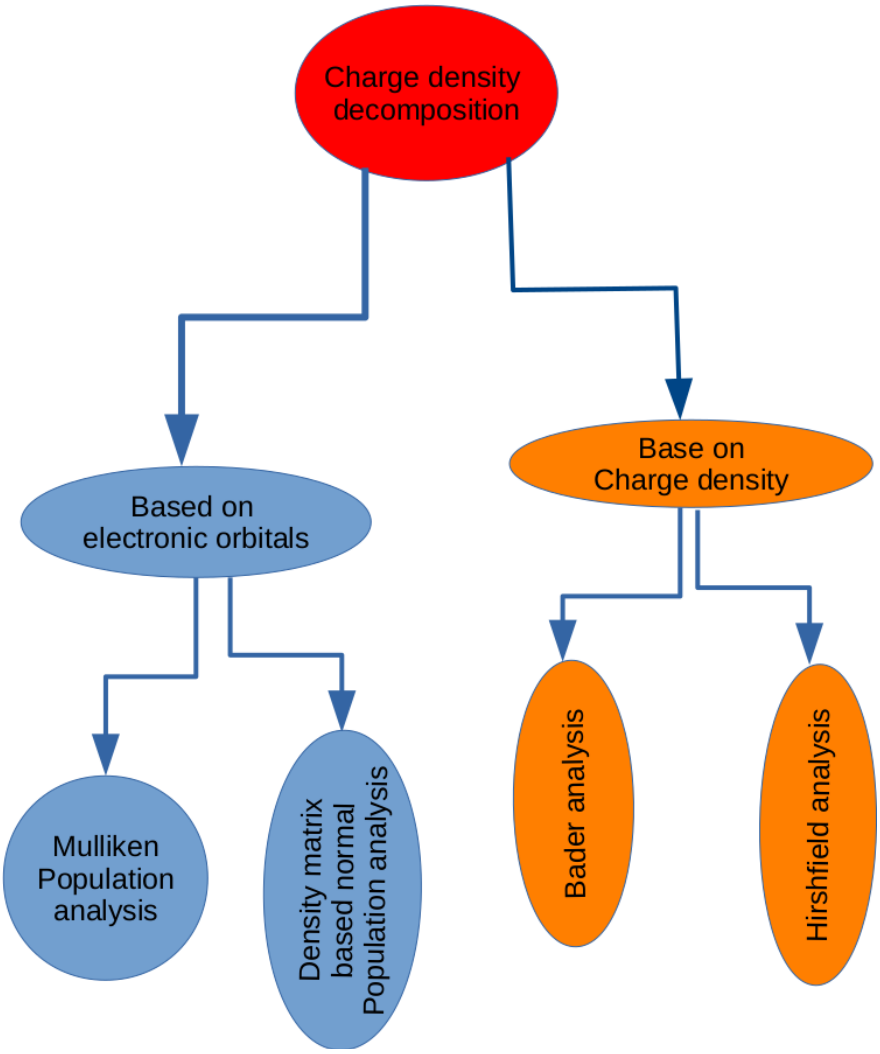

Figure 3.5: Schematic diagram showing charge density decomposition.

3.3.1 Electronic orbital decomposition

Charge density decomposition based on electronic orbital consists of two techniques namely the Mulliken population analysis and density matrix based normal population analysis as outlined below:

Mulliken population analysis

This technique is applicable when the basis functions are centered on atoms and is used in calculation of the electronic wave function of a system. It is a common method where orbital decomposition is used to obtain the atomic densities. Its short coming is that it is sensitive to the choice of basis set, especially if the basis set is enlarged for higher accuracies. The application of Mulliken analysis technique is therefore presently limited because most first principles simulations use plane wave basis functions that are not assigned to any specific atom in the system [173].

Density matrix based normal population analysis

This technique displays enhanced numerical stability as compared to the Mulliken population analysis, although both are based on electronic orbitals. It describes the electronic distribution in compounds having high ionic character better. It is used to calculate atomic charges and orbital populations of molecular wave functions in general atomic orbital basis sets [174].

3.3.2 Charge density based decomposition

In this class, the charge is analyzed based on its density using two approaches, as succinctly provided below:

Hirshfield analysis

This method was proposed by F. L. Hirshfeld in 1977 [175]. It applies similar procedures as those used in X-ray crystallography and provides an alternative method in cartesian space [176]. In this approach, the electron density in each point ('atomic basin') is distributed among all atoms. The disadvantage of this technique is that it overlaps atoms rather than treating them as discrete entities.

Bader analysis

Bader's theory of atoms in molecules is useful for charge analysis. It is also used to define the hardness of atoms, which can be used to quantify the cost of removing charge from an atom and can as well be used to determine the bond strength [177]. Basically, Bader analysis involves the decomposition of electronic charge density into atomic contribution. The region is partitioned into small atomic regions, where the dividing surfaces are at a minimum in the charge density and its gradient is zero along the perpendicular direction [173]. Therefore, since Bader analysis is purely based on charge density decomposition, it is insensitive to the basis set used hence applicable in plane wave based calculations and also those using atomic basis functions. Besides being the most superior method, Bader analysis has its own pitfalls as well, in that it is computationally demanding and the existing algorithms at the moment are complex.

In this study, Bader analysis was used to examine the electron density distribution on the most stable surfaces of the sulvanite compounds.

3.4 Boltzmann Transport Equations (BTE)

At the equilibrium position, electrons being fermions obey Fermi-Dirac distributions;

$$f_o(\epsilon, T) = \frac{1}{\left[e^{(\epsilon-\epsilon_F)/K_BT} + 1\right]}. \tag{3.4.1}$$

In absence of any external force, the behavior of electrons can be described fully by equation (3.4.1). However, when external forces are introduced i.e temperature gradient or electric fields, equation (3.4.1) becomes invalid since it cannot describe well the distribution of charges brought about by inelastic scattering phenomena such as electro-optical phonon scattering. This is where BTE becomes handy. Generally, the BTE have been developed to describe the distribution function in presence of external forces and inelastic scattering processes.

For the steady state, in the presence of a low electric field, BTE can be expressed as [178, 179];

$$v(\vec{k}).\nabla_r f(\vec{k}, T) + \frac{e\vec{E}}{\hbar}.\nabla_k f(\vec{k}, T) = \int \left\{ s(\vec{k'}, \vec{k}) f(\vec{k'}, T) \left[1 - f(\vec{k}, T)\right] - s(\vec{k'}, \vec{k}) f(\vec{k}, T) \left[1 - f(\vec{k'}, T)\right] \right\} d\vec{k'}; \tag{3.4.2}$$

where the first term in equation (3.4.2) is the diffusion term from the carrier density and the second term is due to the external electric field; $f(\vec{k}, T)$ is the Fermi-distribution at the wave vector $(\vec{k})$ and temperature (T); $s(\vec{k'}, \vec{k})$ is the differential scattering rate from the state $\vec{k'}$ to the state characterized by $\vec{k}$ and $v(\vec{k})$ is the carrier's group velocity which is given by;

$$v(\vec{k}) = \nabla_k \epsilon \vec{k}/\hbar. \tag{3.4.3}$$

In practice, Boltzmann transport equations have recently been implemented in various computational packages such as PhonTS, ALAMODE, ShengBTE and PHONO3PY. In this study, we used PHONO3PY [180], which compute lattice thermal conductivity by calculating the anharmonic force constants as well as solving the BTE.

3.5 Relationship between kinetic coefficients and Seebeck coefficient

For a system in which an electric current and heat current flow parallel to the *x*-axis (one dimensional transport), in absence of applied magnetic field, electric current flux (J_e) and heat current flux (J_q) are coupled such that they can be expressed as [181];

$$-J_e = L_{11}\frac{d\Phi}{dx} + L_{12}\frac{dT}{dx}; \tag{3.5.1}$$

$$-J_q = L_{21}\frac{d\Phi}{dx} + L_{22}\frac{dT}{dx}; \tag{3.5.2}$$

where the kinetic coefficients $(L's)$ are properties of the medium studied and are related to electric and heat conductivities. Φ is the electrochemical potential divided by unit charge, which is basically the electromotive force [182].

For a conductor that is at thermal equilibrium, $dT = 0$, hence the second term on the right hand side of equation (3.5.1) and (3.5.2) vanishes. Taking a ratio of the remaining parameters gives;

$$\frac{J_q}{J_e} = \frac{L_{21}}{L_{11}} \implies J_q = \frac{L_{21}}{L_{11}} J_e = \Pi J_e. \tag{3.5.3}$$

equation (3.5.3) implies that the heat current and electrical current are related through the Peltier coefficient, Π. If we then impose a condition $J_e = 0$ by assuming an open circuit, equation (3.5.1) becomes;

$$0 = L_{11}\frac{d\Phi}{dx} + L_{12}\frac{dT}{dx} \implies \left[-\left(\frac{d\Phi}{dx}\right) / \left(\frac{dT}{dx}\right)\right] = \frac{L_{12}}{L_{11}}; \tag{3.5.4}$$

equation (3.5.4) can be re-arranged as;

$$\frac{L_{12}}{L_{11}} = \frac{-d\Phi}{dT} = -\frac{V}{\Delta T} = S; \tag{3.5.5}$$

where S is the Seebeck coefficient and V is the Seebeck voltage between two points of the homogeneous material.

Onsager proposed that there exist a reciprocity relation between the kinetic coefficients such that;

$$L_{21} = TL_{12}; \tag{3.5.6}$$

which is analogous to the expression relating Seebeck and Peltier coefficients;

$$\Pi = TS. \tag{3.5.7}$$

Under the relaxation time approximation, there also exist a relationship between transport coefficients and electronic structure of a material. If we consider an isotropic system with a single band, we obtain the following expressions [183];

$$L_{11} = \frac{-e^2}{3}\int V^2 \tau \frac{\partial f_0}{\partial E}\Delta(E)dE; \tag{3.5.8}$$

$$L_{12} = \frac{e}{3T}\int V^2 \tau [E - E_f]\frac{\partial f_0}{\partial E}\Delta(E)dE; \tag{3.5.9}$$

Substituting equation (3.5.8) and (3.5.9) onto equation (3.5.5) gives;

$$S = -\frac{1}{eT}\ \frac{\int V^2\tau[E-E_f]\frac{\partial f_0}{\partial E}\Delta(E)dE}{\int V^2\tau\frac{\partial f_0}{\partial E}\Delta(E)dE}; \tag{3.5.10}$$

where S is the Seebeck coefficient, $\Delta(E)$ is the electron density of states per unit volume in a given energy interval, E_f is the electrochemical potential and f_0 is the Fermi-Dirac distribution function.

From the above equations, it is visible that the Seebeck coefficient is dependent on the electronic structure of a material around the Fermi-level. In addition, it is sensitive to effective mass, carrier concentration and band shape as briefly discussed in section 3.7, providing useful information beyond resistivity [182].

3.6 Transport and thermoelectric properties

Vital transport parameters like the Seebeck coefficient, electronic contribution to thermal conductivity, electrical conductivity and power factor with respect to temperature were computed after solving the Boltzmann transport equations. Basically, the Seebeck effect entails the conversion of thermal energy onto electrical energy. It is caused by the movement of charge carriers from higher to lower temperature regions, producing a voltage of several microvolts per Kelvin [$S = \frac{\Delta V}{\Delta T}$]. In Figure 3.6, we provide a diagrammatic representation of the Seebeck effect whereby at the heat source, temperature is higher hence electrons and holes move towards the heat sink. Thus, more negative (positive) charges accumulate at the n-type (p-type) section of the heat sink creating a potential difference and consequently, the electric current is generated.

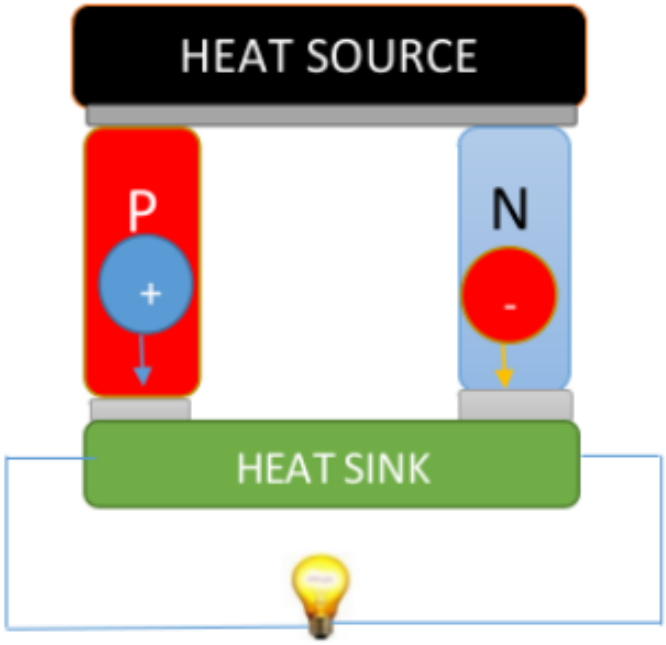

Figure 3.6: Diagrammatic representation of the Seebeck effect.

Being a measure of the magnitude of an induced thermoelectric voltage in response to a temperature difference across that material, Seebeck coefficient is also known as the thermopower and the sign of the Seebeck coefficient denotes the dominant charge carriers, i.e. positive for holes and negative for electrons [184]. Furthermore, Seebeck coefficient and group velocity (where the latter is defined as the gradient of the dispersion relation in the reciprocal space of electrons in the crystals), are related through the following expression [53];

$$S = ek_B\sigma^{-1}\sum_{\vec{k}}\left(\frac{-\partial f_o}{\partial\varepsilon}\right)\vec{v}_{\vec{k}}\vec{v}_{\vec{k}}\vec{\tau}_{\vec{k}}\frac{\varepsilon_{\vec{k}}-\mu}{k_BT} \quad ; \quad \vec{v}_{\vec{k}} = \frac{1}{\hbar}\frac{\partial\varepsilon_{\vec{k}}}{\partial\vec{k}}; \tag{3.6.1}$$

On the other hand, the electrical conductivity and electronic contribution to thermal conductivity are given by;

$$\sigma = e^2\sum_{\vec{k}}\left(\frac{-\partial f_o}{\partial\varepsilon}\right)\vec{v}_{\vec{k}}\vec{v}_{\vec{k}}\vec{\tau}_{\vec{k}} \quad ; \quad \kappa_e = k_B^2T\sum_{\vec{k}}\left(\frac{-\partial f_o}{\partial\varepsilon}\right)\vec{v}_{\vec{k}}\vec{v}_{\vec{k}}\vec{\tau}_{\vec{k}}\left(\frac{\varepsilon_{\vec{k}}-\mu}{k_BT}\right)^2 - T\sigma SS; \tag{3.6.2}$$

where e is the electronic charge, k_B is Boltzmann constant, σ is electrical conductivity, f_o is Fermi-Dirac distribution function, ε is the band energy, $\vec{v}_{\vec{k}}$ is the group velocity, $\hbar$ is the reduced Planck's constant, whereas $\vec{\tau}_{\vec{k}}$ denotes the band dependent relaxation time; which signify the average time between two successive phonon-scattering events. The relaxation time is the characteristic time for a distribution of electrons in a solid to approach or relax to equilibrium after a disturbance is removed. The electrical conductivity of a material is directly proportional to relaxation time, such that a highly conductive material possess relatively long relaxation time.

Power factor specifies how much electricity can be generated whereas the figure of merit (ZT), specifies how efficient electricity is obtained for a given temperature difference [185]. It is composed of a product of Seebeck coefficient squared and electrical conductivity, also expressed as $(P.F = S^2\sigma)$, which is the component of the numerator of equation (2.2.1). Thus, materials with higher power factor are preferred in order to obtain a larger value of dimensionless figure of merit (ZT), since large power factor means that a large voltage and a high current can be generated.

BoltzTraP2 package [186] was used to solve the Boltzmann transport equations resulting in approximate values of various transport coefficients such as S, σ and κ_e as the output. This in turn provides all the ingredients apart from the lattice thermal conductivity that are essential in calculating the thermoelectric figure of merit as indicated in equation (2.2.1) and illustrated in the workflow of Figure 3.7.

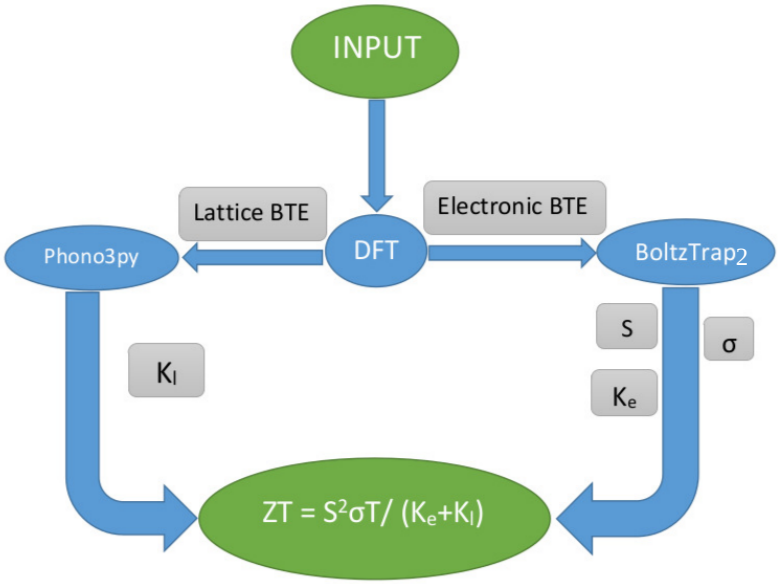

Figure 3.7: Workflow for computing ZT.

3.7 Relationship between effective mass and Seebeck coefficient

Effective mass is a quantity bearing the dimensions of mass, that characterizes the dynamical behavior of a free particle as it moves in presence of an external potential. The second derivative of band energy as a function of the wave vector is related to the inverse of effective mass of electron or hole at the band extremes.

From uncertainty principle, we can obtain the following relations by slight re-adjustment:

$$E = \frac{p^2}{2m^\star} = \frac{\hbar^2 k^2}{2m^\star}; \tag{3.7.1}$$

differentiating equation (3.7.1) twice with respect to the wave vector (k) gives;

$$\frac{\partial^2 E}{\partial^2 k} = \frac{\hbar^2}{m^\star}; \tag{3.7.2}$$

and we can further re-arrange equation (3.7.2) as;

$$\frac{1}{m^\star} = \frac{1}{\hbar^2}\frac{\partial^2 E}{\partial^2 k}. \tag{3.7.3}$$

According to Sundarraj *et al.* [187], for metals or degenerate semiconductors, Seebeck coefficient (S) is related to effective mass ($m^\star$) according to Pisarenko relation that is often used in the field of thermoelectrics as [188];

$$S = \frac{8\pi^2 K_B^2}{3eh^2} m^\star T \left(\frac{\pi}{3n}\right)^{\frac{2}{3}}; \tag{3.7.4}$$

where h and K_B are Planck's and Boltzmann's constant respectively and n is the electron concentration. Effective mass and/or charge mobility play a significant role in the separation and ease of transfer of photo-generated charge carriers to the surface [189]. Zhang *et al.* [190], proposed that photocatalysts with lighter average effective mass results in lowest recombination rate, hence boosting the photocatalytic performance. Also, pursuant to Sundarraj *et al.* [187], the key for achieving higher ZT through band structure engineering should be low effective mass along the transport direction. It is worth noting that the experimental measurement of effective mass of carriers have a number of difficulties. However, the theoretical calculations can provide necessary information to understand the photocatalytic performance [191].

4

COMPUTATIONAL DETAILS

In this Chapter, we present the workflow in form of a schematic diagram indicating the material properties of interest and the simulation steps that were followed. We also describe how convergence was undertaken in line with the underlying scientific principles in order to achieve the optimized values for the properties of interest; all the way from determination of the lattice constant to the peak where we examine the lattice dynamics, transport phenomena and surface properties.

4.1 Workflow

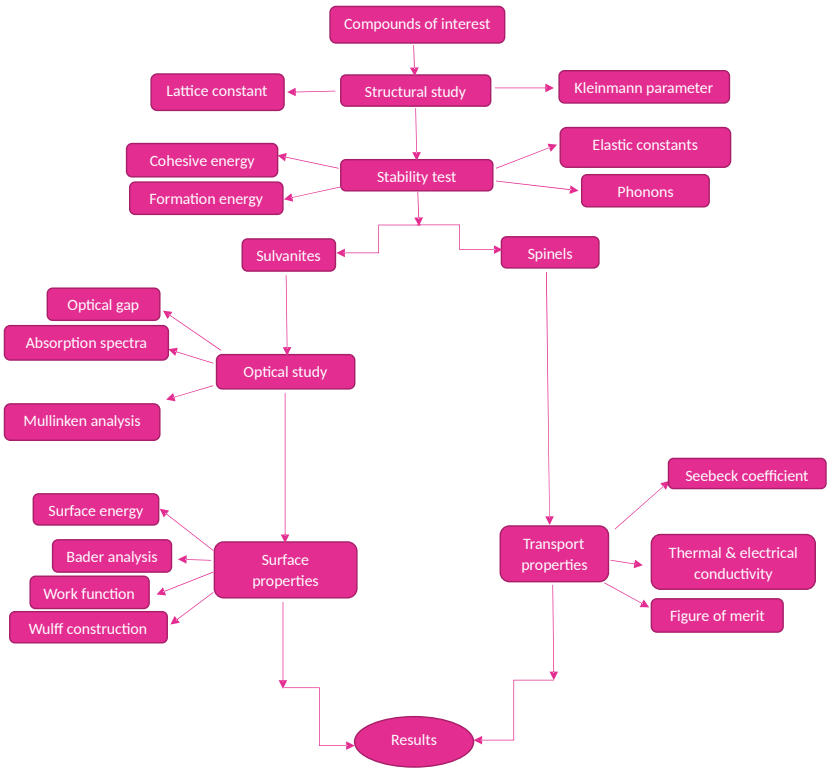

Figure 4.1: Simulation steps.

Figure 4.1 shows a schematic diagram of our simulation steps. At the initial stages, the input files of the selected sulvanite compounds and spinel oxides were obtained from materials project database. Geometry optimization was carried out since the geometrical arrangement of atoms governs the electronic, magnetic, optical and other relevant surface properties, hence we obtained numerical data about their lattice constants and Kleinman parameter using the VASP code [51]. This package is an efficient density functional theory based code for systems with periodic boundary conditions. Secondly, stability studies were carried out to validate their dynamical, energetic and mechanical stability. Thirdly, optical study of the sulvanite compounds was undertaken within many body perturbation theory at Bethe-Salpeter Equation (BSE) [192] level of approximation to obtain their optical band gaps. At this point, the absolute band edges were determined via Mulliken analysis. Thereafter, surface study was undertaken to determine the surface energy, vacuum potential, work function, alignment of band edges via band gap center approach as well as other relevant photocatalytic properties. At the peak of this study, transport properties of spinel oxides were computed by solving Boltzmann transport equations [193] to obtain the Seebeck coefficient, electrical conductivity, thermal conductivity, power factor and consequently the dimensionless figure of merit.

4.2 Convergence in ab initio calculations

Computer simulations can rapidly reduce the number of candidates for a particular application following the desired design criteria based on few descriptors that connect the microscopic quantities to the macroscopic properties, and then suggest potential materials for experimental investigation [194]. In *ab initio* studies, we can loosely state that a parameter is converged when the values of the dependent quantity attains saturation, or is no longer varying with an increase in the values of the dependent parameter. Hence, convergence test is applied, which is a technique used in first principles studies to determine the optimum value of the parameter under consideration such as the behavior of k-point grid with total energy and cut-off energy with respect to slab energy of the surface among others, as discussed briefly below and also outlined in the appendix section.

4.2.1 K-points convergence

Proper selection of the k-points ensures the reciprocal space of the irreducible Brillouin zone is sampled accordingly, resulting in correct numerical integration. Denser grid will most likely lead to an increase in central processing unit (cpu) time required to perform the first principles calculations. For surface studies, the k-point meshes were adjusted depending on the size of the surface models to provide well converged total energies. Since the slabs generated weren't cubic like their bulk counterparts, the k-point values for each supercell axes were scaled inversely with the length of that axis, so as to maintain a similar k-point sampling in the reciprocal space.

4.2.2 Total slab energy convergence versus cut-off energy

If all the plane waves are put into consideration, the simulation process becomes computationally expensive, this has been discussed broadly in the appendix as well. To resolve this problem, upon doing a careful convergence of cut-off energies, we then include only the plane waves whose kinetic energies are smaller than the cut-off in our basis set. This will not only boost the computational feasibility, but also ensures that the accuracy of the obtained numerical values are not compromised. In Figure 4.2,

we show a systematic investigation on the total slab energies calculated using different magnitudes of cut-off energies for the plane waves along three low index orientations of Cu_3TaSe_4. It is clear that total slab energies obtained when the cut-off energies are 400 eV (or above) seems converged.

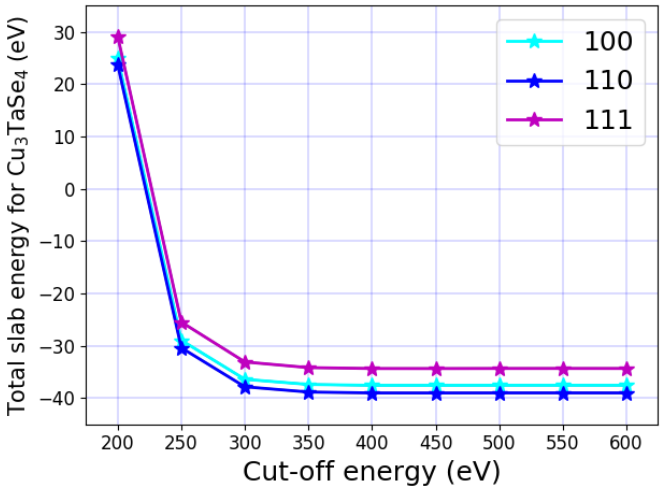

Figure 4.2: Cut-off energy convergence for Cu_3TaSe_4 along various low index surface orientations.

4.3 Structure optimization

Relaxation of the crystal structures were carried out for the cubic sulvanites and spinels of interest using the Vienna *ab initio* Simulation Package (VASP) [51]. The Brillouin zones of the cubic unit cells were sampled by a gamma centered k-mesh of 6×6×6 for the bulk systems, whereas a 2×2×1 grid was used for the slab studies. To examine the effects of different exchange correlation functionals; PBE, LDA and PBEsol [195–197] were employed in order to ascertain which among the three flavors reproduces the ground state properties of a given compound comparably with available experimental data. It is worth noting that all calculations were performed at ground state (0 K). The static first principles calculations were conducted with a precision as high as 10^{-8} eV for the total energy difference between two successive self-consistency steps and 10^{-4} (eV/Å) as the convergence criterion for the forces on atoms. The lattice parameters were then optimized under zero-pressure condition. For the bulk systems, the plane-wave expansion was truncated at a cut-off energy of 520 eV, whereas for the slab surfaces 400 eV was deemed sufficient, and all the calculations were non-spin-polarized.

4.4 Surface energy simulation steps

Upon confirming the stability of the bulk structures of Cu_3QSe_4 sulvanites, we then generated surface slabs with different orientations (as indicated in the workflow provided in Figure 4.3), in order to investigate their surface stability. The methodology is as follows: upon obtaining the bulk crystal structures from the materials project database, a careful structural relaxation of the bulk systems was done using the PBEsol functional to get optimized bulk structures. Thereafter, the automatic flow (AFLOW) package [11] was used to create stoichiometric slabs of varying slab thickness. Convergence

of the slab thickness were then undertaken in order to establish the optimized slab size upon which the vacuum size convergence was initiated, so as to ensure that the interaction between the periodic images is negligible.

This resulted in extraction of the values of converged energies for the geometries of interest, which were then compared so as to ascertain the most relatively stable surface orientation by applying the surface energy as the stability descriptor, where the one with the lowest magnitude of surface energy is relatively the most stable orientation. This in turn facilitated further exploration such as determination of work function, vacuum potential and examination of the alignment of the band edges relative to water redox potential via the band gap center approach, among other properties that are of interest in photocatalysis.

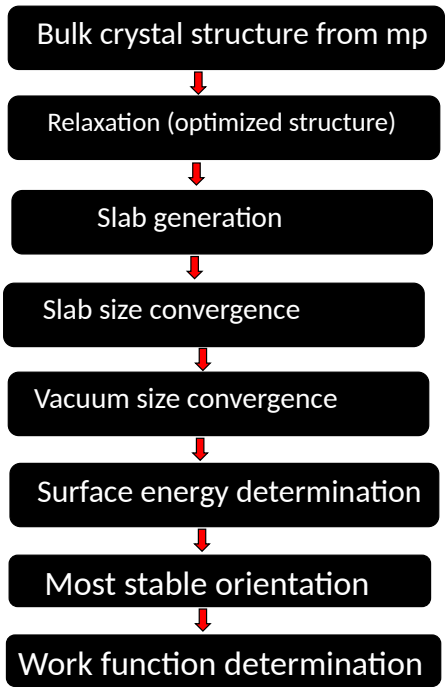

Figure 4.3: Schematic diagram showing surface simulation steps.

4.5 Electronic structure

The electronic band structures and density of states for the bulk systems were obtained using the modified Becke-Johnson exchange potential (mBJ) [198] with the width of the smearing set to 0.01 eV applying the Gaussian smearing technique and selecting a damped velocity friction algorithm as the convenient option to specify the electronic minimization. The energy difference between the conduction band and the valence band is called the band gap. Its magnitude depends mainly on the configuration of its crystal lattice, amount of electrons in the valence shell and hybridization of the orbitals [199].

The position of electronic band edges is one important metric for determining a material's capability to function as a solar energy conversion device [105], among other technological applications. Besides the thermodynamic stability, the electronic structure of photocatalysts is another key factor for their photocatalytic performances [200].

4.6 Midgap surface states

These are deep surface states that are often located in the middle of the band gap [201]. According to Gang *et al.*, the surface states in the forbidden zone arises from the sharp transition from solid material that occurs at the atomic layer closest to the surface due to incomplete covalent bonds at the surface of the semiconductor [202]. For periodic systems, one can explore its electronic and vibrational properties with ease using density functional theory approaches by taking advantage of its 3D periodicity. However, for the surface studies (2D), the periodicity is broken in one direction resulting in structural changes hence introducing localized electronic and vibrational states [203]. Atoms on the surface of a material have fewer neighbors than atoms in the bulk implying their equilibrium positions, energies and most of their properties are different from those of the bulk atoms [204]; because during surface relaxation, atoms loose some neighbors and move from their ideal positions.

According to Lüth [205], the localized surface states are produced by either a discontinuity provided by the surface of the solid (intrinsic surface states with 2D periodicity of the surface), or by imperfections near the surfaces such as adsorbed atoms (extrinsic states). This in long run is very instrumental in photocatalytic related applications in that these surface states act as trapping centers for the photogenerated charge carriers as the spatial overlap of the charge carriers is reduced, hence suppressing their recombination due to the localized nature of the surface states. In addition, the electronic properties of the surfaces of a material are important in order to understand its suitability as a photo electrode [206]. In this work, the surface electronic states were identified by comparing the surface and bulk electronic spectrum, especially the partial density of states.

According to Berkovits *et al.* [207], it was difficult initially to detect the presence of surface states in the electronic properties of a semiconductor experimentally, as it was challenging to distinguish a weak optical signal originating from the surface against a strong background of much more intense signals from the bulk part of the system being probed. Fortunately, new techniques with such capability have emerged over the years such as the surface differential reflectivity and photo-thermal displacement spectroscopy.

4.7 Vibrational properties

A collective vibration of atoms in the crystals forms a wave with a given wavelength and amplitude. The quantum of lattice vibrations is called the phonon. These quantized lattice vibrations in turn provides a platform to examine some solid state phenomena which cannot be explained by the static lattice theory [208] such as temperature dependence of specific heat in solids, thermal expansion and thermal conductivity. The allowed frequencies of a propagation wave can be classified into two, that is an upper branch known as the optical branch, and a lower branch called the acoustical branch. To differentiate between the two; the acoustic modes dominate the low frequency region, they also play a crucial role in Brillouin scattering process. Moreover, the atoms in the unit cell vibrate in the same direction and the adjacent atoms often vibrates in-phase. On the other hand, optical modes that occurs

in the high frequency region, are involved in Raman scattering processes, atoms in the unit cell vibrate in the opposite directions and the adjacent atoms vibrate out-of-phase.

These vibrational states are crucial for characterizing the bulk materials and the relationship between the vibrational energy/frequency (ω) and the wave vector (k) is known as the phonon dispersion. The study of phonon vibration is important for understanding how energy is absorbed in solids. In our study, the dynamical properties were calculated within the harmonic approximation; whereby parameters like density of states, Helmholtz free energy and specific heat capacity were extracted alongside the frequencies of the phonon vibrations. A phonon calculation was undertaken using a finite displacement approach as implemented in PHONOPY [209], where a symmetry reduced set of atomic displacements was generated. Afterwards, all the elements of force constants between atoms in a primitive cell and the supercell were fitted to the symmetry expanded forces of atoms in the supercell [210]. Preferably, in this approach, the supercell has to be sufficiently large to prevent artificial forces due to the periodic boundary conditions used in DFT calculations.

4.8 Mechanical properties

Mechanical properties of solid materials are primarily dependent on the elastic constants which determine the response of the crystal to external forces that subject its atoms to strain or stress as characterized by the bulk modulus, shear modulus, Young's modulus and Poisson's ratio. In addition, having accurately established values of the independent elastic constants enables one to deduce other mechanical properties of a material such as its stability, anisotropy, ductility/brittleness, hardness, sound velocity and Debye temperature among others as briefly discussed below.

4.8.1 Born stability criterion for cubic systems

Elastic properties are determined by forces acting on atoms when they are perturbed from their equilibrium positions. A strain-stress method was applied in computing the elastic constants. All the bulk compounds of interest in this study are cubic, hence have high symmetry. Generally, cubic crystal structures have three independent elastic coefficients. Thus, to evaluate their mechanical stability, we have to examine if they fulfill three of the following Born stability criteria [211];

$$C_{11} - C_{12} > 0; \quad C_{11} + 2C_{12} > 0; \quad C_{44} > 0; \tag{4.8.1}$$

4.8.2 Zener anisotropy factor

Zener anisotropy factor denoted by A, is a pointer to the degree of anisotropy in a solid structure. For a completely isotropic material where the mechanical properties are independent of direction, the Zener anisotropy factor takes the value of 1, whereas when the value of A is smaller or greater than unity, it indicates elastic anisotropy [212]. For cubic systems, it is expressed as;

$$A = \frac{2C_{44}}{C_{11} - C_{12}}. \tag{4.8.2}$$

The elastic anisotropy of crystals is correlated with the possibility to induce micro-cracks in a material, which has an important implication in engineering [213].

4.8.3 VRH averaging schemes

Upon determining the values of the independent elastic constants; other mechanical properties such as the bulk modulus, shear modulus, Young's modulus and Poisson's ratio among others can be directly calculated via the Voight-Reuss-Hill method. Although there are basically three averaging schemes often used to compute the shear and bulk moduli that applies elastic constants namely Voight [214], Reuss [215] and Hill [216]; in this study we adopted the Hill's approach which frequently gives the mean of the Voight and Reuss values, whereby the Voight scheme often overestimates numerical data as it assumes a uniform strain whereas the Reuss method underestimates numerical data since it presume a uniform stress. According to Voight's scheme, from elastic constants, one can compute the bulk and shear modulus as;

$$B_V = \frac{1}{9}[2(C_{11} + C_{12}) + 4C_{13} + C_{33}]; \qquad G_V = \frac{1}{30}[M + 12C_{44} + 12C_{66}] \tag{4.8.3}$$

Reus's scheme is given by;

$$B_R = \frac{C^2}{M}; \qquad G_R = \frac{5}{2}[C^2 C_{44} C_{66}]/[3B_V C_{44} C_{66} + C^2(C_{44} + C_{66})] \tag{4.8.4}$$

$$\text{where} \quad M = C_{11} + C_{12} + 2C_{33} - 4C_{13}; \qquad C^2 = C_{33}(C_{11} + C_{12}) - 2C_{13}^2 \tag{4.8.5}$$

Diversely, Hill's scheme is an average of both;

$$B_H = \frac{1}{2}(B_V + B_R); \qquad G_H = \frac{1}{2}(G_V + G_R) \tag{4.8.6}$$

4.8.4 Brittleness and ductility

Pugh proposed that if the ratio of the bulk to shear modulus (B/G) value is less than the critical value (1.75), the material is considered brittle, otherwise it is ductile [217]. The reciprocal of Pugh ratio (B/G) is known as the Frantsevich's ratio (G/B) [218], where a value less than 0.571 pinpoint ductility whereas for brittle materials the Frantsevich's ratio is greater than 0.571. Ductile materials have relatively small Young's modulus and can withstand large strains and large energy absorption before fracture, e.g., steel and aluminium. Conversely, brittle materials have relatively large Young's modulus and fracture at a much lower strain, e.g., glass and cast iron.

4.8.5 Poisson's ratio

The characteristics of a given material is also dictated by the strength of its bonds which can be described based on its value of Poisson's ratio; whereby for covalently bonded materials $\nu \approx 0.1$ whereas for ionic materials $\nu \approx 0.25$ and for metallic ones $\nu \approx 0.33$ [219].

4.8.6 Kleinman parameter

Kleinman parameter denoted by ζ, describes the relative positions of the cation and anion sublattices under volume conserving strain distortions for which positions are not fixed by symmetry. For cubic systems, the Kleinman parameter can be computed from the independent elastic coefficients as [213];

$$\zeta = \frac{C_{11} + 8C_{12}}{7C_{11} + 2C_{12}}. \tag{4.8.7}$$

Basically, the Kleinman parameter describes the ease of bond bending to the bond stretching in cubic materials, whereby minimizing the bond bending leads to $\zeta = 0$, and minimizing the bond stretching leads to $\zeta = 1$.

4.8.7 Vicker's hardness index

Vicker's hardness index (H_{v}) points out the resistance of a material to deformation. It links both the elastic and the permanent plastic properties of a material and is defined as [220];

$$H_{\mathrm{v}} = 2\Big(K^2 G\Big)^{0.585} - 3; \tag{4.8.8}$$

where K is the Frantsevich's ratio (G/B), that is often used to indicate if a material is brittle or ductile as discussed in section 4.8.4.

4.8.8 Sound velocity

The propagation velocity of longitudinal and transverse waves along different crystal directions is related to the elastic constants, whereby the wave velocity of a longitudinal wave (v_{l}) and transverse wave (v_t) as well as the average velocity (v_{m}) can be deduced from the values of bulk moduli, shear moduli and material's density based on Navier's equation as follows [221];

$$v_{\mathrm{l}} = \sqrt{\frac{1}{3\rho}[3B + 4G]}; \quad v_{\mathrm{t}} = \sqrt{\frac{G}{\rho}}; \quad v_{\mathrm{m}} = \left[\frac{1}{3}\left(\frac{2}{v_{\mathrm{t}}^3} + \frac{1}{v_{\mathrm{l}}^3}\right)\right]^{-1/3}; \quad \Theta_{\mathrm{D}} = \frac{h}{k_{\mathrm{B}}}\left[\frac{3n}{4\pi}\left(\frac{N_A \rho}{M}\right)\right]^{1/3} v_{\mathrm{m}}; \tag{4.8.9}$$

In principle, determination of sound velocity provides crucial information about the rate at which sound travels through a given medium.

4.8.9 Debye temperature

Thermal properties of a material are related to Debye temperature (Θ_{D}) as indicated in equation (4.8.9), where k_{B} is the Boltzmann constant, h is the Plank constant, n is the number of atoms in its chemical formula, N_A is the Avogadro constant, ρ is the density of the material and M is the molecular weight. Debye temperature is used to assess the temperature above which all modes begin to be excited and below which modes begin to be frozen out [222]. Debye temperature is of central importance when describing the thermal behavior of solids that is involved in all physical phenomena that are concomitant to the lattice vibrations i.e lattice thermal conductivity, specific heat capacity, melting temperatures and sound velocity. The knowledge of such a numerical entity (Θ_{D}), is useful for developing and manufacturing electronic devices by providing information about the characteristics of a solid material under the effect of temperature.

4.8.10 Transport phenomena

All the necessary crystal eigen-energies for transport calculations were obtained from VASP. The deformation potential constants and elastic constants were used to obtain a set of charge carrier relaxation times that were energy and k-point dependent as per the approach proposed by Bardeen and Shockley [223]. We followed the implementation as outlined by Xi *et al.* [224]. These relaxation times were used in determining the electronic transport coefficients, where the BoltzTraP2 package [186] was used to solve the Boltzmann transport equations resulting in the approximate values of various transport coefficients such as S, σ and κ_e as the output. This in turn provided all the ingredients apart from the lattice thermal conductivity that are essential in calculating the thermoelectric figure of merit, as indicated in equation (2.2.1) and illustrated in the workflow of Figure 3.7.

4.8.11 Lattice thermal conductivity

The lattice dynamics are crucial to both the cooling and transport of photo-excited charge carriers because these phenomena are influenced by the coupling between electronic excitations and the lattice vibrations such as the electron-phonon interactions [225]. It is noteworthy that lattice thermal conductivity is not only a crucial parameter in thermo-electricity, it is also of primary importance in technologies such as heat sinks [226], rewritable density scanning probe phase-change memories [227], power electronics (where heat dissipation is of critical importance) [228] and thermal devices for therapies [229], just to mention a few. In this study, PHONO3PY package [180] was applied in determination of the third order inter-atomic force constants. Full nearest neighbors were considered, implying all the triplet displacements in the supercell were included and a mesh size of 20×20×20 was found sufficient for obtaining well converged values of lattice thermal conductivity, group velocities, phonon lifetime, Grüneisen parameter and mean free path. Generally, lattice thermal conductivity is calculated when anharmonic interactions are considered, hence providing some insights on the phonon-phonon scattering mechanisms, which are not captured within the harmonic approximations [230].

4.8.12 Correlation between lattice thermal conductivity, group velocity and phonon lifetime

Boltzmann transport equations in the single mode relaxation time approximations were applied in determining the phononic contribution to thermal conductivity (κ_l) as implemented in the PHONO3PY and expressed in equation (4.8.10) of phonon conductivity tensor [180];

$$\kappa_l = \frac{1}{NV_o} \sum_{\lambda} c_\lambda \mathbf{v}_\lambda \otimes \mathbf{v}_\lambda \tau_\lambda; \tag{4.8.10}$$

where $\mathbf{v}_\lambda$, c_λ, τ_λ, N and V_o are the group velocity, mode heat capacity, single mode relaxation time of the phonon mode λ, number of unit cells in the crystal and volume of the primitive cell, respectively. To obtain accurate values of thermal conductivities, both acoustic contributions and the contributions from optical phonon branches were considered with all the mode-dependent entities on the right hand side of equation (4.8.10) calculated using the second-order and third-order force constants as implemented in the PHONO3PY. From equation (4.8.10); it is visible that although several parameters come to play when computing the lattice thermal conductivity of a material; group velocity and phonon lifetime are directly proportional to κ_l. This signifies that materials which possess large values of group velocity and

phonon lifetime at lower frequency ranges often have a higher values of lattice thermal conductivity, which automatically translates to low values of the dimensionless figure of merit.

4.8.13 Helmholtz free energy

Helmholtz free energy tends to describe the thermodynamical stability of a system, as it indicates how phonons determine the relative stability at finite temperatures [231]. Helmholtz free energy of phonon vibration (F) and specific heat capacity were extracted from the thermal calculations as functions of temperatures at a constant volume by applying the thermodynamic relations as implemented in the PHONOPY code and described by Togo and Tanaka [209]. According to Togo *et al.* [232]; the phonon contribution to the Helmholtz free energy at a constant volume is defined as;

$$F_{\text{phonon}} = \frac{1}{2}\sum_{\mathbf{q},\,\text{v}} \hbar\omega_{\mathbf{q},\,\text{v}} + k_{\text{B}}T\sum_{\mathbf{q},\,\text{v}} ln[1-\exp(-\hbar\omega_{\mathbf{q},\,\text{v}}/k_{\text{B}}T)]; \tag{4.8.11}$$

where $\hbar$, $\mathbf{q}$, v, $\omega_{\mathbf{q}\text{v}}$, T and k_{B} are reduced Planck's constant, wave vector, band index, phonon frequency at $\mathbf{q}$ and v, temperature and Boltzmann constant, respectively. Note that, the first term on the right hand side of equation (4.8.11) is the sum of the modal contributions to the zero-point vibrational energy and the second term is the contribution of each mode of the free energy due to thermal occupation of the phonon energy levels [233].

4.8.14 Specific heat capacity

The specific heat capacities of the three ternary compounds increases with temperature and tends to reach the saturation limit known as the Dulong-Petit limit [234], which is a prevalent property of all solids. Specific heat capacity is basically from the contributions from the individual modes, that is often expressed at a constant volume as;

$$C_{\text{v}} = \sum_{\mathbf{q},\,\text{v}} k_{\text{B}}\left(\frac{\hbar\omega_{\mathbf{q},\,\text{v}}}{k_{\text{B}}T}\right)^2 \frac{\exp(\hbar\omega_{\mathbf{q},\,\text{v}}/k_{\text{B}}T)}{\left[\exp(\hbar\omega_{\mathbf{q},\,\text{v}}/k_{\text{B}}T)-1\right]^2}; \tag{4.8.12}$$

4.8.15 Phonon group velocity and phonon lifetimes

Lifetime is related to equilibrium properties of the material, whereas the relaxation time relates to the thermal and electrical transport. Lifetime is defined as the mean time that an electron will reside in a given quantum state as a result of collision with another particle. Mean free path is the average distance that an electron travels before a collision. Phonon group velocity and phonon lifetimes are directly proportional to the magnitude of the lattice thermal conductivity as indicated in equation (4.8.10), hence an increase in group velocity or phonon lifetimes results in an increase in lattice thermal conductivity. The phonon mean free path can be evaluated as the product of the momentum-resolved phonon group velocity and phonon lifetime [225].

4.8.16 Grüneisen parameter

The Grüneisen parameter is a quantity that characterizes the degree of anharmonicity of a crystal. It describes the effect that changing the volume (V) of a crystal lattice has on its vibrational properties, such as frequency of the ith mode of vibration and is often expressed as;

$$\gamma_i(\mathbf{q}) = -\frac{\partial\ ln\,\omega(\mathbf{q})_i}{\partial\ ln\,V}. \tag{4.8.13}$$

It also acts as a descriptor on the effect that changing temperature has on the size or dynamics of the crystal lattice [235] and is a dimensionless quantity. Fortunately, Slack [236] postulated a rather simple relationship that can help uncover the correlation between the total Grüneisen parameter and the lattice thermal conductivity, such that the magnitude of the following four parameters namely the average atomic mass, interatomic bonding, crystal structure and lattice thermal conductivity determine the degree of anharmonicity in a given material since;

$$\kappa_l = A\frac{M\delta n^{1/3}\Theta^3}{\gamma^2 T};\quad \text{where}\quad A = \frac{2.43\times10^{-8}}{1-\frac{0.514}{\gamma}+\frac{0.228}{\gamma^2}}; \tag{4.8.14}$$

by which M and δ^3 are the average atomic mass and the volume per atom respectively, whereas n is the number of atoms in the primitive unit cell and Θ is the acoustic Debye temperature. Therefore, equation (4.8.14) signify that the lattice thermal conductivity and the total Grüneisen parameter have an inverse relationship. Thus, one of the criterion for obtaining a low thermal conductivity is by seeking materials with ordered crystal structures exhibiting strong lattice anharmonicity.

5

RESULTS AND DISCUSSION

In this chapter, we present, evaluate and discuss the obtained results in detail. As previously stated, the main goal of this work was to investigate the photocatalytic properties of the sulvanite type compounds $Cu_3(Ta,Nb,V)Se_4$ and thermoelectric properties of $Cd(Ga,Al)_2O_4$ spinel oxides in line with clean energy production via photocatalysis and thermoelectricity respectively. It is also worth mentioning that in this chapter only the results and analyses are reported, whereas the details of the techniques, material aspects and applications have been given in previous chapters. Hence, in section 5.1, we provide the obtained results about the structural, energetic, electronic, mechanical, dynamical and thermal properties as well as the lattice dynamics alongside the transport and thermoelectric properties of $Cd(Ga,Al)_2O_4$ spinel oxides with an interest in thermoelectricity, where the dimensionless figure of merit was determined, that describes how efficient a material could be in line with thermoelectricity, where thermal energy is converted to electrical energy and vice versa.

In section 5.2; we focus on the $Cu_3(Ta,Nb,V)Se_4$ sulvanites where results on their structural, energetic, electronic, mechanical, dynamical and thermal properties are reported alongside their lattice dynamics for the bulk systems. Since our presupposed area of application for the sulvanite compounds is in photocatalysis, where materials having some specific qualities are preferred, we delved onto their optical studies in which their optical gaps were determined by applying the approach of Tauc fitting as provided in section 5.3.1. Furthermore, bearing in mind that photocatalytic reactions often occurs at the surface of a material, we also did some surface calculations as indicated in the workflow presented in Figure 4.3, upon which we determined its surface energies, work function, Wulff construction and other relevant properties for the most stable surface orientation. We also computed the density of states for the relatively stable surface geometries for each compound, in order to detect the presence of the surface states. Additionally, we determined the charge density differences via the Bader charge analysis approach and finally used the obtained results to gauge the viability of Cu_3TaSe_4, Cu_3NbSe_4 and Cu_3VSe_4 sulvanites for single photon water splitting through photocatalysis.

5.1 $Cd(Ga,Al)_2O_4$ spinel oxides

With an interest in thermoelectric application in mind, we explored the structural, energetic, mechanical, dynamical, lattice dynamics, transport and thermoelectric properties of $CdGa_2O_4$ and $CdAl_2O_4$ spinels as discussed below.

5.1.1 Structural and energetic properties

In first principles studies, one has to ensure that the model being used to mimic any compound of interest conforms with the experimentally verified sample where possible. This is often verified based on the ability of the model to reproduce some of the basic experimentally reported structural and physical properties such as lattice constant, volume and density among others. Additionally, metastability of a compound can be easily detected based on numerical values of its formation and cohesive energies. This then justifies why structural and energetic behavior of any material has to be carried out prior any in-depth studies.

Table 5.1 shows the lattice constant (a), equilibrium volume (V_o), density (ρ), cohesive (E_{coh}) and formation energies (E_{form}) in Å, Å^3, g/cm^{-3} and eV/atom respectively for $Cd(Ga,Al)_2O_4$ spinels, calculated using three functionals in comparison with the existing experimental data where possible.

Table 5.1: Structural and energetic properties of $Cd(Ga,Al)_2O_4$ spinel oxides.

	$CdGa_2O_4$					$CdAl_2O_4$				
	a	V_o	ρ	E_{coh}	E_{form}	a	V_o	ρ	E_{coh}	E_{form}
PBE	8.78	676.84	6.19	-4.08	-1.63	8.51	616.30	4.97	-5.11	-2.43
PBEsol	8.67	651.71	6.45	-4.54	-1.68	8.42	596.95	5.12	-5.55	-2.48
LDA	8.58	631.62	6.64	-4.97	-1.80	8.34	580.09	5.27	-5.98	-2.64
Expt.	8.59[a]	633.84	6.62	-	-	8.36[b]	584.28	5.24	-	-

a = Ref. [237], b = Ref. [238]

For $Cd(Ga,Al)_2O_4$ spinel oxides, LDA functional reproduced its structural properties better than PBE and PBEsol in comparison with the existing experimental information. This ability of LDA functional to reproduce the ground state properties of spinels has been reported before [239]. The negative values of both cohesive and formation energies obtained, attest that these compounds are energetically stable, thus cannot dissociate into their elemental solids. PBE and PBEsol functionals overestimated the lattice parameter (a) and volume (V_o), resulting in underestimation of density (ρ) when compared with the existing experimental values.

5.1.2 Electronic properties

Figure 5.1 and 5.2 displays the electronic band structures of cubic $CdGa_2O_4$ and $CdAl_2O_4$ spinels computed using LDA and mBJ functionals. This is because among the various functionals applied, LDA produced the ground state properties of $CdGa_2O_4$ and $CdAl_2O_4$ spinels that have better agreement with the experimental data as tabulated in Table 5.1. But as it is well known, the LDA functional often underestimates the fundamental gaps of semiconductors and insulators by approximately 40% due to the existence of a derivative discontinuity of the energy with respect to the

number of electrons [148]. Thus, to counter the shortcoming of DFT in predicting the fundamental gaps, we also employed the modified Becke-Johnson exchange potential (mBJ) [198].

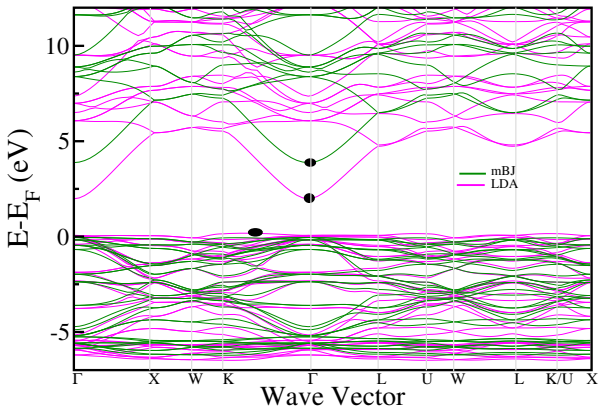

Figure 5.1: The electronic band structure for $CdGa_2O_4$.

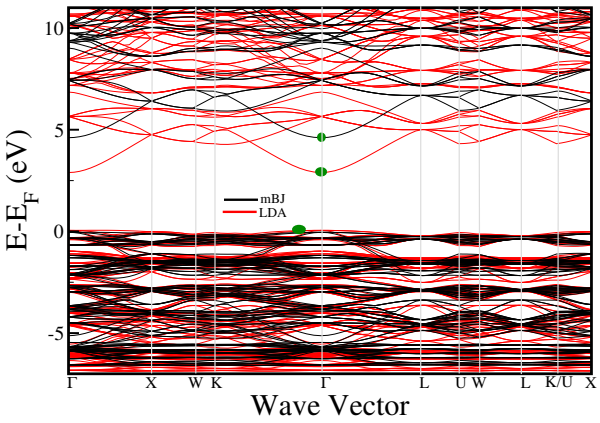

Figure 5.2: The electronic band structure for $CdAl_2O_4$.

In both systems, the top of the valence band is located between K and Γ point along the high symmetry directions of the Brillouin zone, whereas the bottom of the conduction band is located at Γ point. This indicates that these two ternary compounds have indirect band gaps. Table 5.2 gives our calculated values of the fundamental gaps in comparison to other reported theoretical values, which indicates that our findings are in accord with the previously reported data.

Table 5.2: Fundamental gaps (eV).

Compound	LDA	mBJ	PBE[c]	PBE[d]	mBJ[c]
$CdAl_2O_4$	2.84	4.65	2.70	2.90	4.70
$CdGa_2O_4$	1.81	3.92	1.50	1.92	3.70

c = Ref. [44], d = Ref. [25]

From the tabulated values, it is visible that the size of the gap decreases as we move down the group 13 elements from aluminium (Al) to gallium (Ga). Moreover, we can see that the band structures determined using LDA have a relatively smaller gap size than those obtained using mBJ. This is because the LDA often underestimates the fundamental band gaps of materials due to the existence of a derivative discontinuity of the energy with respect to the number of electrons [148] as stated earlier. On the other hand, being a semi-local exchange potential-only functional, mBJ [198] incorporates some exact Hartree-Fock exchange in the exact functional which is not present in the local density approximation.

5.1.3 Mechanical properties

In Table 5.3, we present the computed values of mechanical properties of $Cd(Ga,Al)_2O_4$ spinel oxides such as their bulk (B), shear (G) and Young's modulus (E), independent elastic coefficients (C_{ij}), Frantsevich's ratio (G/B), Zener anisotropic factor (A), Kleinman internal-displacement parameter

(ζ) as well as Poisson's ratio (ν), sound velocity (v_m) and Debye temperature (Θ_D) together with the Vicker's hardness index (H_v), alongside other existing theoretical data where possible.

The values of the computed mechanical properties are comparable to other existing theoretical findings. From the data of the independent elastic coefficients provided in Table 5.3, it is visible that the necessary and sufficient Born stability conditions were fulfilled, implying that $CdGa_2O_4$ and $CdAl_2O_4$ spinels are mechanically stable. $CdGa_2O_4$ spinel possess slightly lower values of both the bulk and shear modulus relative to $CdAl_2O_4$. Based on the deduced values of the Frantsevich's ratio (G/B), which are between 0.34 and 0.40, we can confirm that $CdGa_2O_4$ and $CdAl_2O_4$ are ductile since their G/B values are less than 0.571 across all the functionals considered.

All the values of Zener anisotropy factor (A) are greater than unity indicating that these two spinels possess elastic anisotropy implying that when they are subjected to stress or strain, their mechanical properties vary depending on the direction along which the forces are applied. Moreover, their Kleinman parameter (ζ) values lie between 0.74 and 0.78 implying that in both systems, the magnitude of bond stretching is much smaller compared to bond bending. Since the obtained values of Poisson's ratio (ν) lies between 0.32 and 0.33, it pinpoints that the dominant bonding type in $CdGa_2O_4$ and $CdAl_2O_4$ is metallic in nature.

The range of the obtained values of Vicker's hardness index (H_v) obtained, that is (3.02 - 3.80) GPa for $CdGa_2O_4$ and (5.00 - 5.37) GPa for $CdAl_2O_4$, indicate that $CdAl_2O_4$ displays a greater resistance to deformation as compared to $CdGa_2O_4$ and also suggests that materials with higher bulk or shear modulus may be likely harder, as can be seen in Table 5.3. Taking a closer look at the values of the computed sound velocities attest that $CdGa_2O_4$ has higher values of longitudinal, transverse as well as the average sound velocities than $CdAl_2O_4$, implying that sound travels faster in $CdGa_2O_4$ than $CdAl_2O_4$. This could be attributed to the fact that $CdGa_2O_4$ possess a higher density than $CdAl_2O_4$ as shown in Table 5.1. By virtue of being a mechanical wave, sound travels by compression and rarefaction of the medium under consideration. Generally, the sound velocity increases with an increase in density because a higher density leads to more elasticity in the medium and hence the ease by which compression and rarefaction occurs translating to a higher sound speed.

On average, $CdAl_2O_4$ has a higher value of Debye temperature than $CdGa_2O_4$, this could be associated with the reason that aluminium (Al) has a smaller standard atomic weight of about 26.98 as compared to gallium (Ga) whose standard atomic weight is 69.72. Since Debye temperature and atomic mass are inversely proportional as indicated in equation (4.8.9), a smaller mass (and consequently weight) will translate to a higher value of Debye temperature and vice versa. According to the predicted mechanical properties of $CdGa_2O_4$ provided in Table 5.3 especially the bulk modulus, these spinels are soft when compared to diamond [240]. Moreover, since the Debye temperature is a measure of the temperature above which all modes begin to be excited and below which modes begin to be frozen out, it signify that the low Θ_D in $CdGa_2O_4$ pinpoint that the lattice thermal conductivity in $CdGa_2O_4$ will be more likely lower than that of $CdAl_2O_4$.

Table 5.3: Mechanical properties of $Cd(Ga,Al)_2O_4$ spinel oxides.

		$CdGa_2O_4$			$CdAl_2O_4$			
Parameter	**Functional**	**Present**	**Theory** [e]	**Theory** [f]	**Present**	**Theory** [e]	**Theory** [f]	**Theory** [g]
B (GPa)	LDA	182.21	-	-	196.02	-	-	-
	PBE	149.08	154	158.36	167.86	180	190.69	-
	PBEsol	166.49	-	-	180.99	-	-	187
G (GPa)	LDA	61.45	-	-	75.93	-	-	-
	PBE	56.05	-	-	68.06	-	-	-
	PBEsol	56.85	-	-	70.19	-	-	78
G/B	LDA	0.34	-	-	0.39	-	-	-
	PBE	0.38	-	-	0.40	-	-	-
	PBEsol	0.34	-	-	0.39	-	-	0.31
E (GPa)	LDA	165.71	-	-	201.73	-	-	-
	PBE	149.43	102	-	179.87	114	-	-
	PBEsol	153.13	-	-	186.47	-	-	206
C_{11} (GPa)	LDA	229.38	-	-	257.01	-	-	-
	PBE	190.00	203	257.90	219.74	231	277.25	-
	PBEsol	208.45	-	-	234.95	-	-	292
C_{12} (GPa)	LDA	158.63	-	-	165.52	-	-	-
	PBE	128.62	130	108.59	141.92	149	147.40	-
	PBEsol	145.51	-	-	154.01	-	-	134
C_{44} (GPa)	LDA	88.92	-	-	106.62	-	-	-
	PBE	83.83	91	72.96	98.95	115	113.55	-
	PBEsol	84.42	-	-	101.49	-	-	78
A	LDA	2.51	-	-	2.33	-	-	-
	PBE	2.73	2.49	-	2.54	2.80	-	-
	PBEsol	2.68	-	-	2.51	-	-	-
ζ	LDA	0.78	-	-	0.74	-	-	-
	PBE	0.77	-	-	0.74	-	-	-
	PBEsol	0.78	-	-	0.75	-	-	-
ν	LDA	0.35	-	-	0.33	-	-	-
	PBE	0.33	0.39	-	0.32	0.39	-	-
	PBEsol	0.35	-	-	0.33	-	-	-
H_v (GPa)	LDA	3.30	-	-	5.37		-	-
	PBE	3.80	-	-	5.09	-	-	-
	PBEsol	3.02	-	-	5.00	-	-	-
v_t (m/s)	LDA	3042	-	-	3796	-	-	-
	PBE	3009	-	-	3701	-	-	-
	PBEsol	2969	-	-	3703	-	-	3888
v_l (m/s)	LDA	6307	-	-	7213	-	-	-
	PBE	6013	-	-	7510	-	-	-
	PBEsol	6129	-	-	7323	-	-	7495
v_m (m/s)	LDA	3419	-	-	4245	-	-	-
	PBE	3375	-	-	4155	-	-	-
	PBEsol	3337	-	-	4151	-	-	4352
Θ_D (K)	LDA	453.80	-	-	579.53	-	-	-
	PBE	437.60	-	-	556.26	-	-	-
	PBEsol	438.65	-	-	561.30	-	-	591

e = Ref. [27], f = Ref. [25] g = Ref. [33]

5.1.4 Dynamical properties of $Cd(Ga,Al)_2O_4$ spinels

By probing the vibrational properties of a given material, one may obtain a complete macroscopic characterization of the studied systems [241]. In both spinels, the phonon dispersion curves had no soft phonon modes along the symmetry directions in the Brillouin zone as provided in Figure 5.3 and 5.4, which confirms their dynamical stability. Generally, a phonon of imaginary frequency over much of the Brillouin zone indicates that the structure is unstable.

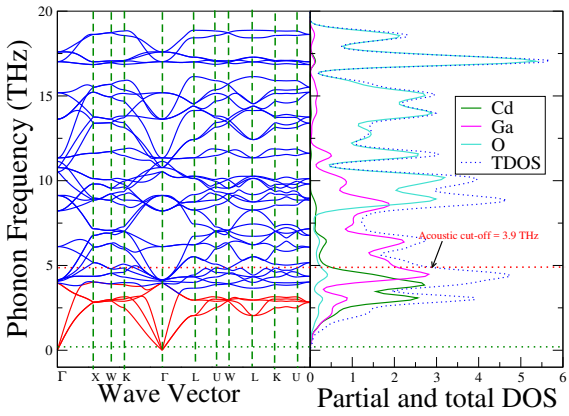

Figure 5.3: The phonon band structure together with partial and total density of states for $CdGa_2O_4$.

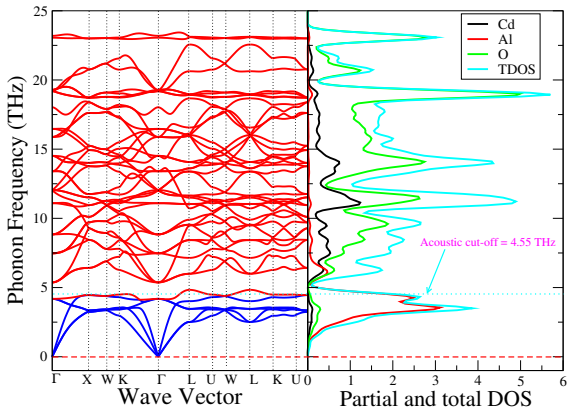

Figure 5.4: The phonon band structure together with partial and total density of states for $CdAl_2O_4$.

The acoustic cut-off frequency, which marks the maxima of the acoustic phonon modes was determined to be approximately 3.9 THz for $CdGa_2O_4$ and 4.55 THz for $CdAl_2O_4$. For the case of $CdGa_2O_4$, the partial phonon density of states indicates that the primary element contributing to the acoustic phonon modes is cadmium, whereas gallium states dominates the region between 5 and 8 THz, the upper states of the optical region above 8 THz are dominated by states of oxygen. For the case of $CdAl_2O_4$, partial density of states display that aluminium monopolize the acoustic region suppressing the contribution from the other two elements whereas in the optical regime, the dominant states arises from oxygen and cadmium. Also, from the phonon dispersion plots provided in Figure 5.3 and 5.4, we can see that the values of the highest frequencies in the optical region decrease as we progress down the periodic table from aluminium ($\approx$ 23 THz) to gallium ($\approx$ 18 THz) due to increase in atomic weight, and the heavier atoms usually vibrate at a slower rate leading to reduced frequencies.

5.1.5 Thermal properties of $Cd(Ga,Al)_2O_4$ spinel oxides

Since first-principles calculations are often done at the absolute zero temperature (T = 0 K); examining the temperature dependence of thermodynamic properties of a material via probing their phonon vibrational behavior at finite temperatures is crucial. Atoms constituting a crystal vibrate about their mean positions, generating thermal energy arising from the vibrational motion. As expected, thermal energy increases with an increase in temperature and dictates the thermal properties of a given material. For $CdGa_2O_4$ ($CdAl_2O_4$), specific heat capacity at a constant volume, approaches a constant value of about 340 (336) $J(mol\ K)^{-1}$ at high temperature. This value is known as the Dulong-Petit limit [242]. From Figure 5.5, 5.6 and 5.7, we predicted that at 300 K, specific heat capacity, Helmholtz free energy and entropy of $CdGa_2O_4$ ($CdAl_2O_4$) are 271.70 (248.03) $J(mol\ K)^{-1}$, 50.29 (78.17) $kJmol^{-1}$ and 274.42 (214.27) $J(mol\ K)^{-1}$, respectively.

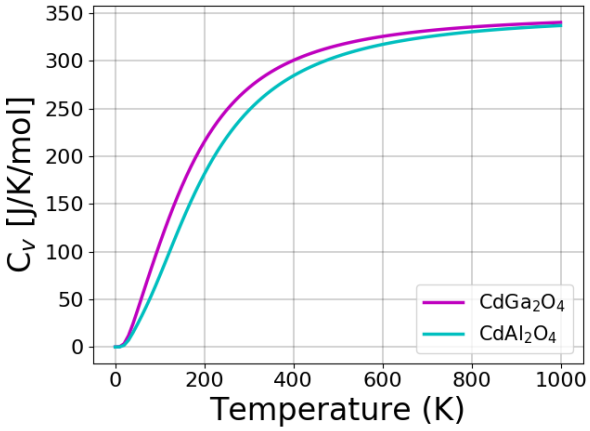

Figure 5.5: Specific heat capacity of $Cd(Ga,Al)_2O_4$.

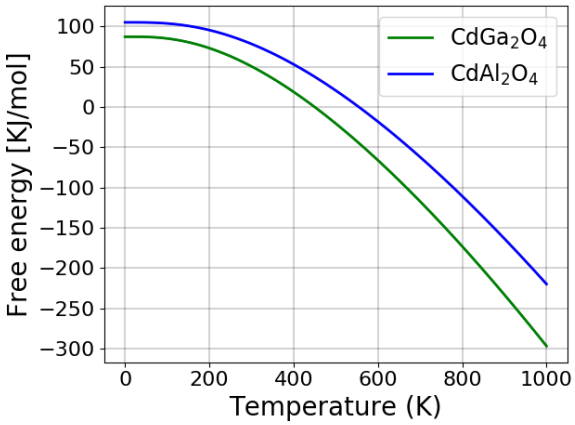

Figure 5.6: Helmholtz free energy of $Cd(Ga,Al)_2O_4$.

It is evident from Figure 5.7 that the degree of disorderness (entropy), increases with an increase in temperature whereas the reverse is true for the Helmholtz free energy. Both $CdGa_2O_4$ and $CdAl_2O_4$ show isotropic thermal properties in that their lattice thermal conductivity is similar in all the directions. This could be attributed to the fact that these compounds are highly symmetric having a cubic structure. Recall that, Helmholtz free energy is related to thermal stability of any given material. From our findings, the Helmholtz free energy of $CdAl_2O_4$ is smaller in magnitude than that of $CdGa_2O_4$ as supported by Figure 5.6, meaning that $CdAl_2O_4$ is relatively more stable thermally. Across the considered temperature range, that is (0 to 1000) K, $CdGa_2O_4$ has higher values of specific heat capacity compared to $CdAl_2O_4$, implying that more heat energy is required to raise the temperature of $CdGa_2O_4$ per unit of mass relative to $CdAl_2O_4$, as supported by Figure 5.5.

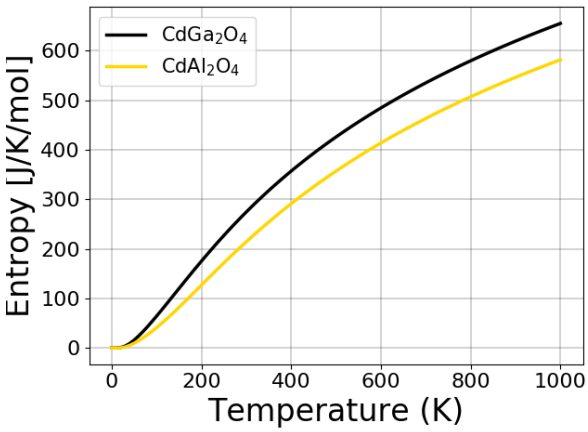

Figure 5.7: Entropy of $Cd(Ga,Al)_2O_4$.

5.1.6 Lattice dynamics in $Cd(Ga,Al)_2O_4$ spinel

The lattice thermal conductivity κ_l, is a necessary additive in order to evaluate the ZT of a given material, hence was examined hereby. $Cd(Ga,Al)_2O_4$ spinel oxides display thermal isotropy in that the behavior of lattice thermal conductivity is independent of the crystal axis. This is because its phonon coupling is similar in the *x*-, *y*- and *z*-directions. This could be because the spinels under consideration

have cubic symmetry. Figure 5.8 depicts that lattice thermal conductivity is less temperature dependent at high temperatures due to increase in anharmonicity. At 300 K, $CdGa_2O_4$ and $CdAl_2O_4$ possess lattice thermal conductivity values of 9.381 and 10.485 W/mK respectively, which are unfortunately not promising for applications related to thermoelectricity, where smaller κ_l are desirable.

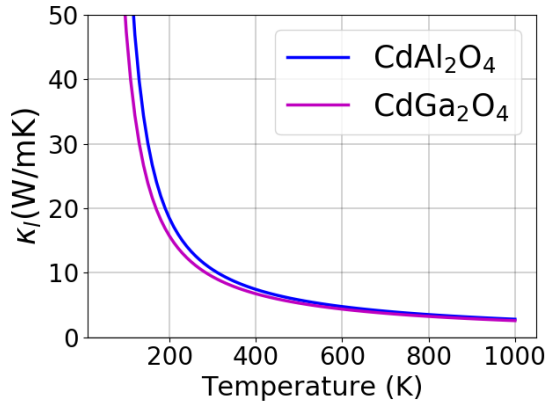

Figure 5.8: Lattice thermal conductivity of $Cd(Ga,Al)_2O_4$.

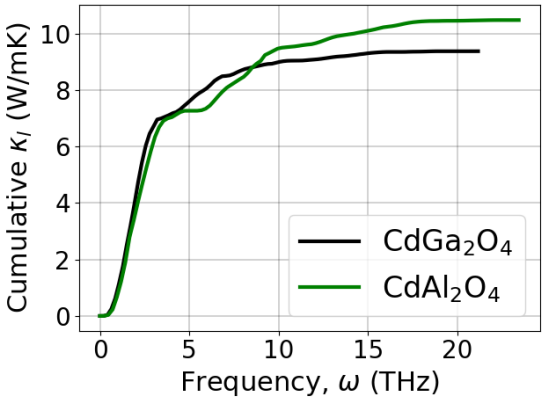

Figure 5.9: Cumulative lattice thermal conductivity of $Cd(Ga,Al)_2O_4$ at 300K.

The cumulative lattice thermal conductivity provided in Figure 5.9 attest that the dominant contributor to κ_l is the acoustic phonon modes, possibly due to short lifetimes. This is reinforced by the view that below their respective acoustic cut-off limits (that is 3.9 THz for $CdGa_2O_4$ and 4.55 THz for $CdAl_2O_4$), there is a sizable increase in the cumulative lattice thermal conductivity at 300 K with an increase in frequency. The low-frequency phonons contribute most to the lattice thermal conductivity due to their higher magnitude of group velocities indicated by strong dispersion in the acoustic regime, as observed in the phonon dispersion curves provided in section 5.1.4.

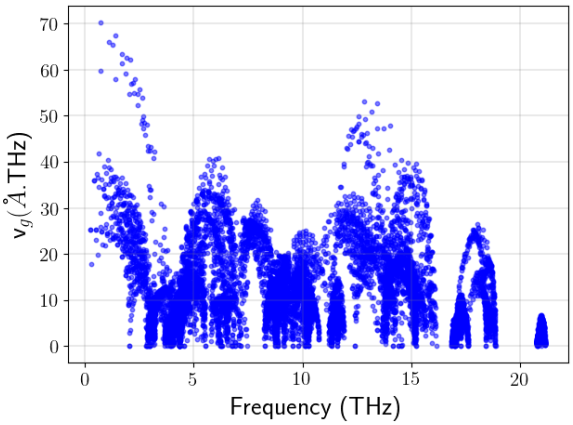

Figure 5.10: Group velocity of $CdGa_2O_4$.

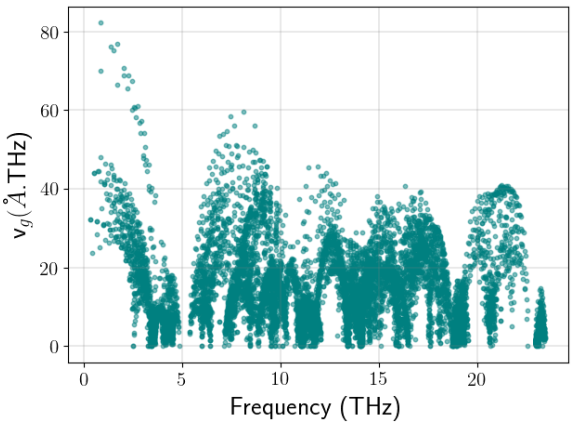

Figure 5.11: Group velocity of $CdAl_2O_4$.

Since $CdGa_2O_4$ and $CdAl_2O_4$ spinels exhibited almost comparable behavior regarding their group velocities as shown in Figure 5.10 and 5.11, we therefore analyzed other intrinsic lattice properties such as the phonon lifetimes, mean free path as well as the total Grüneisen parameters to see if there are any sizable differences between the two compounds that could justify the differences in their lattice thermal conductivity values. From Figure 5.12 and 5.13, for the spinel oxides of interest, the phonon

lifetimes at 300 K can reach as high as approximately 143 and 268 picoseconds (ps) for $CdGa_2O_4$ and $CdAl_2O_4$, respectively, below the 2 THz frequency. In addition, below their acoustic cut-off limits, relatively long phonon lifetimes are observed as compared to that in the high frequency regime where very short phonon lifetimes are recognized. This signifies that the degree of heat transport mechanism is much intensified at the lower frequency region, i.e in the 15 THz region, the average value of phonon lifetime is roughly 3 ps for both spinels; implying that their lifetimes becomes relatively short at higher frequencies.

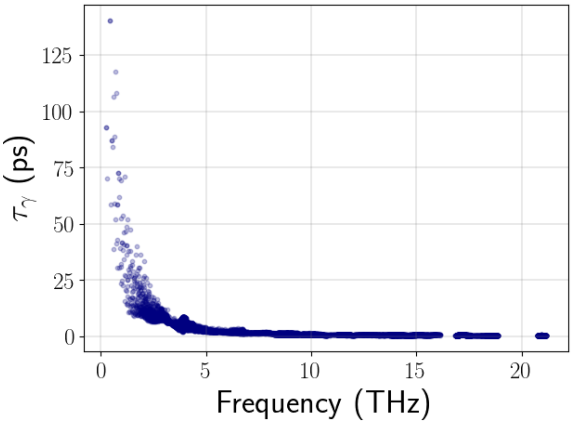

Figure 5.12: Phonon lifetime of $CdGa_2O_4$.

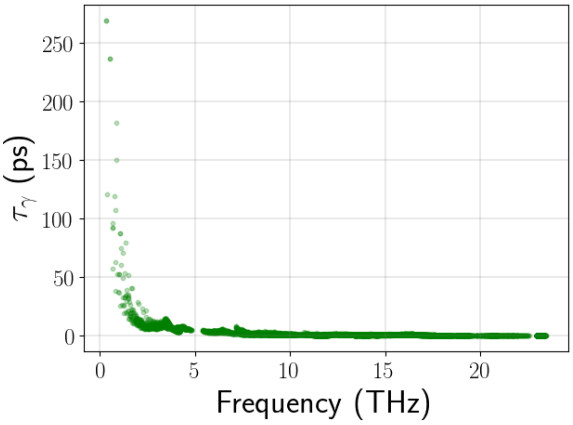

Figure 5.13: Phonon lifetime of $CdAl_2O_4$.

The phonon mean free path can be evaluated as the product of the momentum-resolved phonon group velocity and phonon lifetime [225]. From Figure 5.14, within the acoustic regime (0 - 5 THz), $CdAl_2O_4$ has a larger magnitude of the mean free path as compared to $CdGa_2O_4$. This could be attributed to their substantial variations in their phonon lifetimes. The aforementioned can help uncover the reason why $CdAl_2O_4$ has a larger value of lattice thermal conductivity than $CdGa_2O_4$, as presented in Figure 5.8 and supported by equation (4.8.10).

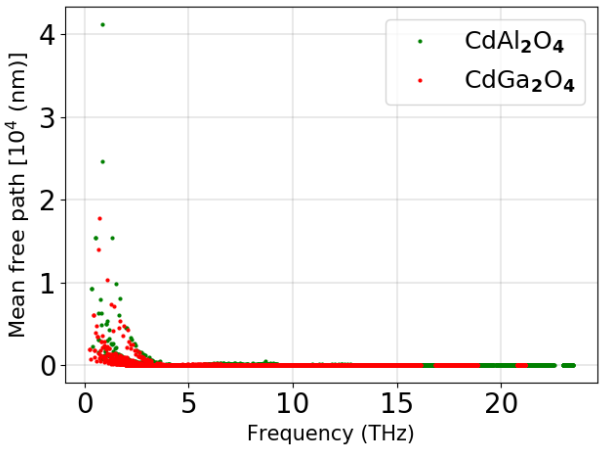

Figure 5.14: Mean free path of $Cd(Ga,Al)_2O_4$.

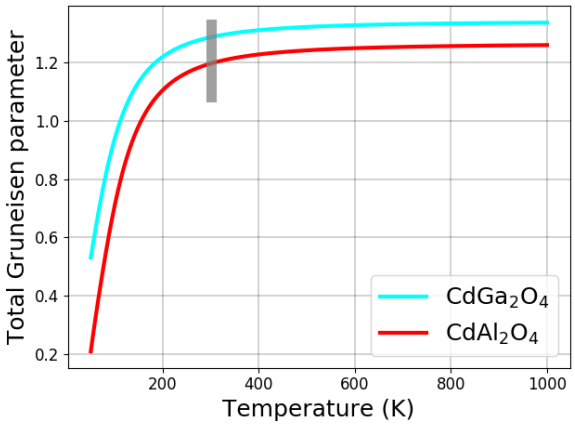

Figure 5.15: Total modal Grüneisen parameter of $Cd(Ga,Al)_2O_4$.

The Grüneisen parameter characterizes the anharmonicity of a material as discussed in section 4.8.16, where a larger value of Grüneisen parameter indicates a strong degree of anharmonicity of a material, which results in a smaller value of the lattice thermal conductivity. This is valid for the case of spinel

oxides in that from the average values of total Grüneisen parameter extracted within the considered temperature range, $CdGa_2O_4$ has a relatively larger value of γ than $CdAl_2O_4$ as indicated in Figure 5.15, whereas according to Figure 5.8, $CdGa_2O_4$ has lower value of lattice thermal conductivity than $CdAl_2O_4$ within the considered temperature range. This affirms the validity of our earlier statement that there is an inverse relationship between the lattice thermal conductivity and the Grüneisen parameter, as previously demonstrated using the Slack's equation (4.8.14). At 300 K, the obtained values of the total Grüneisen parameters are 1.29 and 1.20 for $CdGa_2O_4$ and $CdAl_2O_4$ respectively (indicated by the grey background) in Figure 5.15, which are comparable to that of lithium fluoride reported to be 1.24 by Liang *et al.* [243].

5.1.7 Transport properties of $CdGa_2O_4$

The thermal energy can be converted into electrical energy by the thermoelectric materials, hence a comprehensive study of the transport phenomena in spinel compounds is worth investigating, whereby a variation in temperature and/or carrier concentration leads to an immense change in the magnitude of the transport coefficients such as Seebeck, electrical conductivity, power factor and thermal conductivity. Thus, we hereby considered the stated coefficients within temperature range of 200 and 1000 K. We considered the carrier concentration of 10^{20} and 10^{21} cm^{-3} because the optimum carrier concentrations for high efficiencies are often observed within this range for heavily doped semi-conductors. In accordance with Figure 5.16, it is clear that in $CdGa_2O_4$ spinel, when majority charge carrier are electrons, a very small magnitude of the Seebeck coefficient is attained as compared to the case when the majority charge carriers are holes. The maximum value of 457 μV/K for the Seebeck coefficient is obtained at 1000 K when the hole concentration is 10^{20} cm^{-3}.

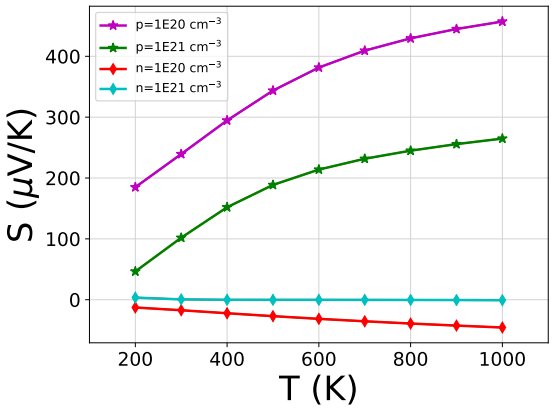

Figure 5.16: Seebeck coefficient of $CdGa_2O_4$.

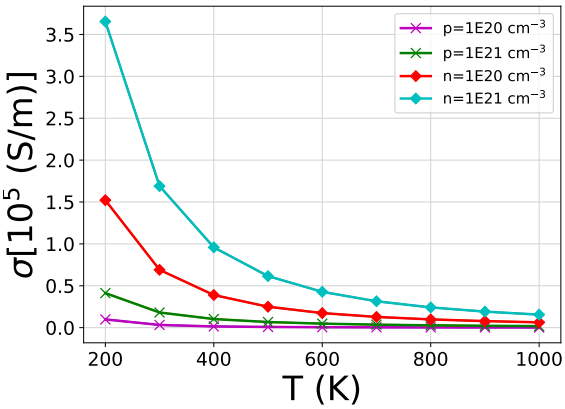

Figure 5.17: Electrical conductivity of $CdGa_2O_4$.

The maximum value of the electrical conductivity is 3.65×10^5 S/m at 200 K, and for all the considered carriers concentrations, σ decreases with an increase in temperature and attains saturation at around 900 K as indicated in Figure 5.17. This behavior can be elucidated using the Wiedemann-Franz law, whereby an increase in temperature results in a decrease in electrical conductivity due to their inverse relationship. Moreover, we recognized that the highest values of electrical conductivity are achieved when majority charge carriers are electrons than holes, which is converse to what was observed for the case of Seebeck coefficient in Figure 5.16.

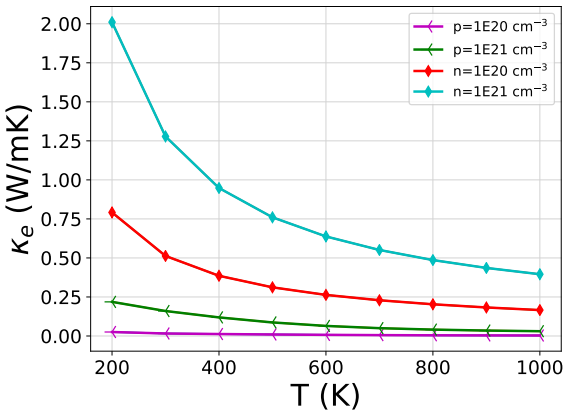

Figure 5.18: Electronic contribution to thermal conductivity of $CdGa_2O_4$.

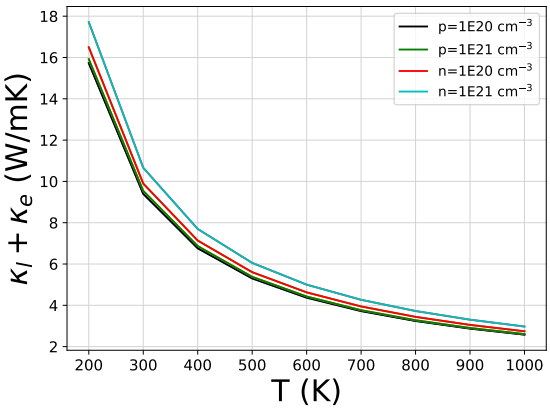

Figure 5.19: Total thermal conductivity of $CdGa_2O_4$.

Contrary to the trend that was observed in Figure 5.17, when majority charge carriers are electrons, the electronic component to thermal conductivity is suppressed as compared to the case when majority charge carriers are holes. Also, based on the magnitudes of the obtained electronic contribution to total thermal conductivity in $CdGa_2O_4$ spinel as compared to the magnitudes of the lattice contribution to total thermal conductivity provided in Figure 5.8; we realized that indeed the lattice component dominates the thermal conductivity in $CdGa_2O_4$ since $\kappa_l > \kappa_e$, this is also in line with Figure 5.19.

Power factor is a parameter used to measure the ability of electric power generation of a material. According to Figure 5.20, it is apparent that the minimum values of the power factor are achieved when the majority charge carriers are electrons as compared to holes. This could be attributed to the fact that when majority charge carriers are electrons, the Seebeck coefficient is very low as discernible in Figure 5.16, although they possess slightly higher values of electrical conductivity as compared to that of holes as supported by Figure 5.17. This is justified since the power factor is the product of Seebeck coefficient squared and electrical conductivity ($S^2\sigma$).

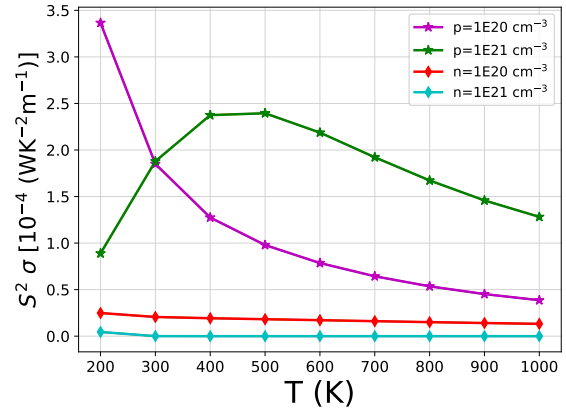

Figure 5.20: Power factor of $CdGa_2O_4$.

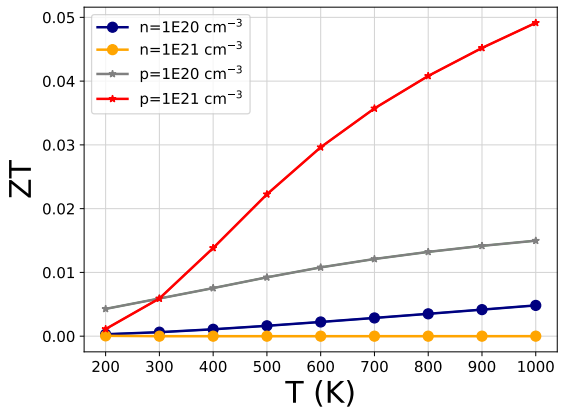

Figure 5.21: Figure of merit of $CdGa_2O_4$.

For the case of holes, when the carrier concentration is 10^{20} cm^{-3}, maximum value of power factor is attained to be 3.36×10^{-4} WK^{-2}m^{-1} at 200 K and decreases in an exponential manner with an increase in temperature. When the hole concentration is 10^{21} cm^{-3}, there is an increase in the

proportion of the power factor between 200 and 400 K above which it saturates all the way to 500 K, then starts decreasing steadily with further increase in temperature. Coincidentally, at 300 K, the values of power factor when charge carriers are holes (with concentration of 10^{20} and 10^{21} cm^{-3}) are both comparable, having an approximate value of 1.85×10^{-4} $WK^{-2}m^{-1}$.

For the case of the dimensionless figure of merit; considering that when the charge carriers are electrons their power factor intensity is suppressed as indicated in Figure 5.20, it consequently leads to very small values of ZT as compared to the case when the dominant charge carriers are holes as can be seen in Figure 5.21. In addition, at 300 K; the values of ZT when majority charge carriers are holes are comparable and the maximum value of the dimensionless figure of merit is attained to be 0.049 at 1000 K, when hole concentration is 10^{21} cm^{-3}. This low value of ZT could be associated with higher values of lattice thermal conductivities reported in section 5.1.6, which indicates that $CdGa_2O_4$ isn't a promising material for thermoelectric applications.

5.1.8 Transport properties of $CdAl_2O_4$

Transport behavior in $CdAl_2O_4$ spinel resembles that observed in the preceding $CdGa_2O_4$ to some extent. The highest value of the Seebeck coefficient of 294 μV/K is attained at 1000 K when hole concentration is 10^{20} cm^{-3} as shown in Figure 5.22. Moreover, for all the considered carrier concentrations, the Seebeck coefficient increases with an increase in temperature. From Figure 5.23, the highest value of 3.78×10^5 S/m for electrical conductivity is achieved at 200 K when the hole concentration is 10^{21} cm^{-3}.

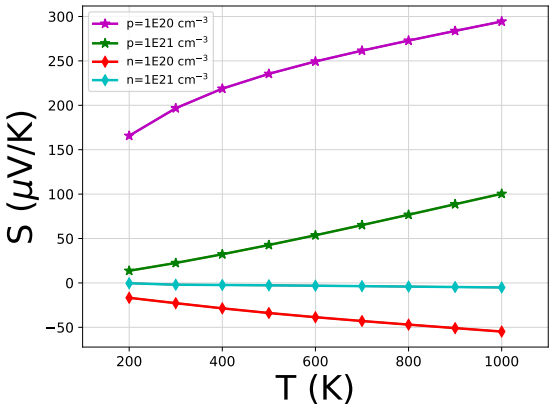

Figure 5.22: Seebeck coefficient of $CdAl_2O_4$.

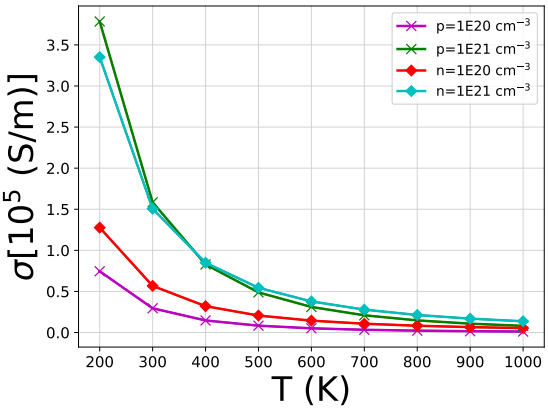

Figure 5.23: Electrical conductivity of $CdAl_2O_4$.

Based on the magnitudes of the electronic contribution to the total thermal conductivity provided in Figure 5.24 in comparison to the contribution from the lattice provided in section 5.1.6, it is evident that lattice transport is the major source of heat transmission as compared to that arising from the electronic transport mechanism. This is notable in Figure 5.25 as well, suggesting that the lattice heat transport carries the majority of heat while electronic part has negligible contributions to the thermal conductivity in $CdAl_2O_4$ spinel.

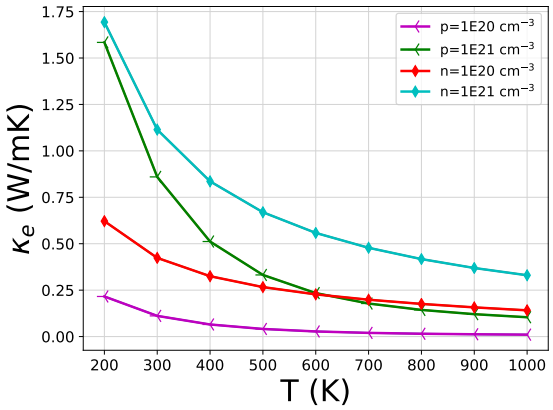

Figure 5.24: Electronic contribution to thermal conductivity of $CdAl_2O_4$.

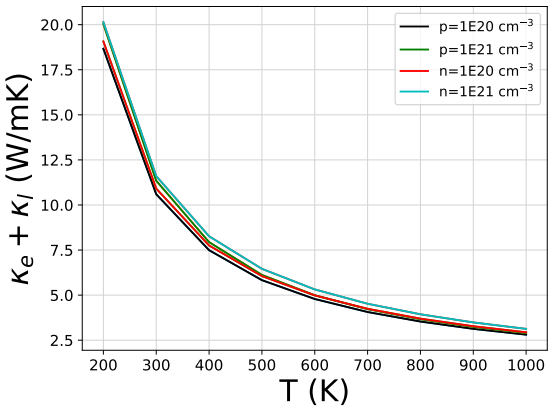

Figure 5.25: Total thermal conductivity of $CdAl_2O_4$.

In the case of the power factor, it is only when the hole concentration is 10^{20} cm^{-3}, when appreciable value of the power factor is detected to be about 20.4×10^{-4} $WK^{-2}m^{-1}$ at 200 K as displayed in Figure 5.26, which decays steadily with an increase in temperature whereas for other intensities of carrier concentrations, the obtained power factors are dismal. In accordance with Figure 5.27, when electrons are dominant charge carriers as well as when hole concentration is 10^{21} cm^{-3}, there is an increase in the value of dimensionless figure of merit with an increase in temperature between 200 K and 1000 K.

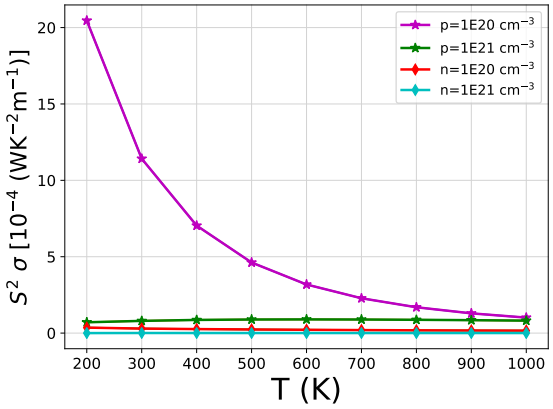

Figure 5.26: Power factor of $CdAl_2O_4$.

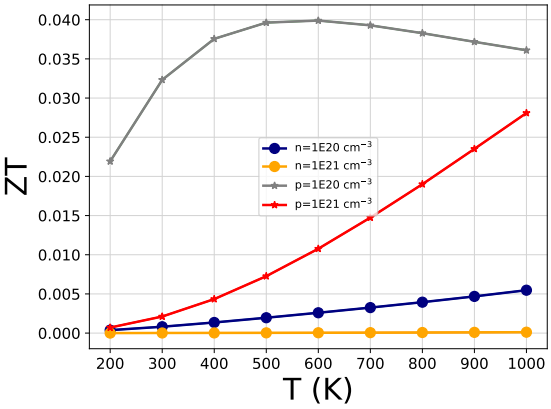

Figure 5.27: Figure of merit of $CdAl_2O_4$.

For the case when hole concentration is 10^{20} cm^{-3}, there is an increase in ZT between 200 K and 600 K at which a maximum value of ZT of 0.04 is attained. Thereafter, beyond 600 K, the value of ZT starts to decrease. The reason why ZT is high when the hole concentration is 10^{20} cm^{-3} compared to others could be associated with its relatively high magnitude of Seebeck coefficient, reduced electrical conductivity as well as minimal value of electronic contribution which consequently translates to reduced value of total thermal conductivity, which in turn boosts its power factor together with ZT, though still not sufficient for the design of more efficient thermoelectric device.

5.2 Cu_3QSe_4 sulvanites

In this section, we discuss the structural, mechanical, dynamical and thermal properties of Cu_3QSe_4 sulvanites. Although our interest is in their photocalytic applications, we realized that in-depth study of lattice dynamics of these compounds is still missing, hence we delved onto it as well. Our primary goal besides stability was to ascertain the possibility of using Cu_3QSe_4 sulvanites in photocatalytic applications. Thus, alongside the above mentioned properties of interest, we also analyzed their electronic properties at the DFT level and optical properties at BSE level of approximation. We also deduced several properties that are related to their surface phenomena such as surface energy, work function and vacuum potential among others, that are relevant for accurate determination of the location of the band edges, which provides viability test for potential materials that can be used in photocatalytic applications.

5.2.1 Structural and energetic properties

Table 5.4 shows the lattice constant (a), equilibrium volume (V_o), density (ρ), cohesive (E_{coh}) and formation energies (E_{form}) in Å, Å^3, g/cm^{-3} and eV/atom respectively for Cu_3QSe_4 calculated using three functionals in comparison with the existing experimental data.

Table 5.4: Structural and energetic properties of Cu_3QSe_4 sulvanites.

	Cu_3TaSe_4					Cu_3VSe_4					Cu_3NbSe_4				
	a	V_o	ρ	E_{coh}	E_{form}	a	V_o	ρ	E_{coh}	E_{form}	a	V_o	ρ	E_{coh}	E_{form}
PBE	5.75	190.11	6.02	-4.16	-0.52	5.68	183.25	5.06	-3.82	-0.49	5.74	189.12	5.25	-4.02	-0.52
PBEsol	5.62	177.50	6.45	-4.62	-0.51	5.53	169.11	5.48	-4.25	-0.49	5.61	176.56	5.63	-4.47	-0.51
LDA	5.54	170.03	6.71	-5.13	-0.50	5.45	161.88	5.71	-4.75	-0.49	5.54	170.03	5.86	-4.98	-0.51
Expt.[h]	5.67	182.28	6.26	-	-	5.57	172.81	5.35	-	-	5.65	180.36	5.55	-	-

h = Ref. [12]

For the case of Cu_3QSe_4 sulvanites, PBE functional overestimated the lattice parameter and consequently volume whereas the LDA underestimated them by a larger margin. Due to overestimation (underestimation) of volume by PBE (LDA), the density is underestimated by PBE and overestimated by LDA as compared with experimental. On the other hand, PBEsol described its structural properties such as lattice constants, volume and density consistently with experimental data than other exchange correlation functionals. Essentially, PBEsol is a functional that is specifically written to describe the behavior of solids with good accuracy as it minimizes their reliance on error cancellation between the exchange part and the correlation part [244]. Based on their negative formation and cohesive energies obtained, these materials are thermo-dynamically stable with respect to decomposition into atoms or elemental solids. Furthermore, the excellent representation of bulk properties by PBEsol gives us confidence to employ it in the surface calculations.

5.2.2 Electronic properties of the bulk Cu_3QSe_4 sulvanites

Figure 5.28, 5.29 and 5.30 illustrates the band structure and density of states for the bulk sulvanite compounds calculated using the mBJ functional. Note that for the case of Cu_3QSe_4 sulvanites, we opted to present their electronic structure in a different pattern to that used for the case of $Cd(Ga,Al)_2O_4$ spinels provided in Figure 5.1, simply because apart from obtaining the values of their fundamental gaps, we are also interested in the partial density of states of Cu_3QSe_4 sulvanites, which

are crucial when carrying out photocatalytic studies of a material. By probing their surface and bulk density of states, one can detect if the localized surface states are present in the surface density of states that were absent in the bulk density of states, which acts as the trapping centers for the photogenerated charge carriers, as previously discussed in section 4.6 and 5.7.1.

Besides, mBJ functional often gives improved values of the fundamental gaps of semiconductors relative to PBEsol, due to the existence of the derivative discontinuity of the energy with respect to the number of electrons in the latter as previously mentioned. The gaps obtained using PBEsol are tabulated in Table 5.5 for comparison purposes, bearing in mind that PBEsol reproduced the ground state properties of Cu_3QSe_4 sulvanites better than PBE and LDA as can be seen in Table 5.4. From our findings, the obtained values of the fundamental gaps from the band structure plots using mBJ functional are 1.87, 1.56 and 1.14 eV for Cu_3TaSe_4, Cu_3NbSe_4 and Cu_3VSe_4, respectively, which are comparable to those reported by Hong *et al.* [14] as provided in Table 5.5.

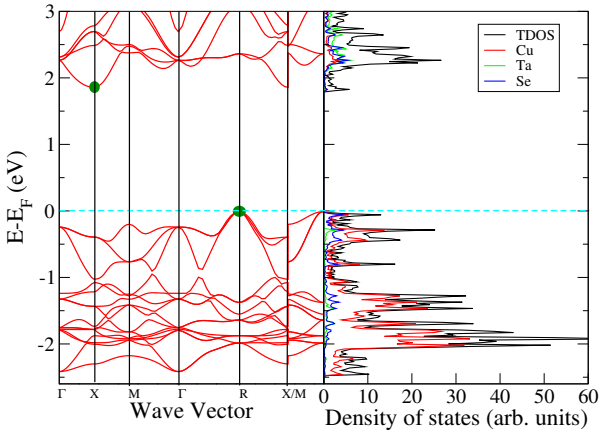

Figure 5.28: The electronic band structure together with partial and total density of states for Cu_3TaSe_4.

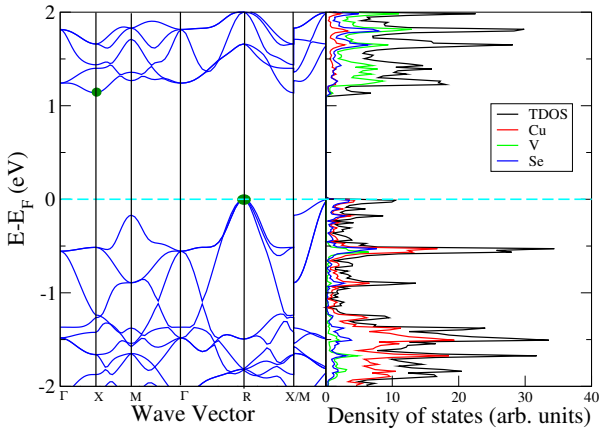

Figure 5.29: The electronic band structure together with partial and total density of states for Cu_3VSe_4.

The nature of their band gap is indirect, where the valence band maxima is at R whereas the conduction band minima is located at point X in their Brillouin zone.

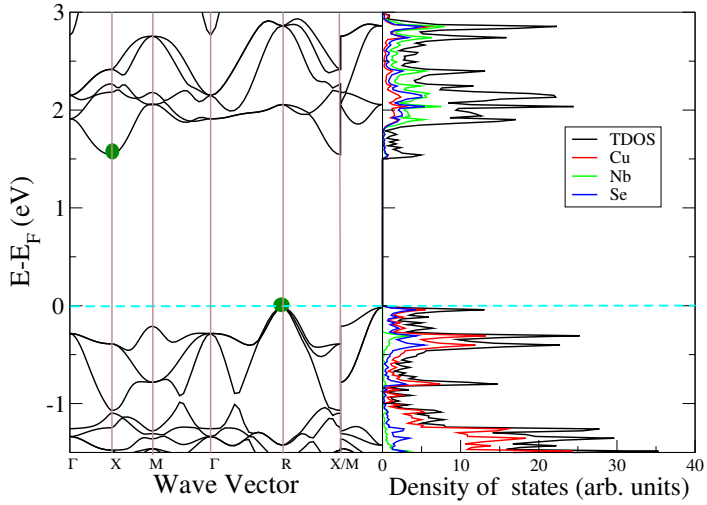

Figure 5.30: The electronic band structure together with partial and total density of states for Cu_3NbSe_4.

Table 5.5: Fundamental gaps (eV).

Compound	PBEsol	mBJ	PBE[i]	mBJ[i]
Cu_3VSe_4	0.90	1.14	0.83	1.06
Cu_3NbSe_4	1.42	1.56	1.38	1.52
Cu_3TaSe_4	1.63	1.87	1.61	1.83

i = Ref. [14]

For the bulk systems, it is visible that copper (Cu) states predominate the valence bands, whereas selenium (Se) and the transition metals (V, Nb,Ta) states dominate the conduction bands. Also the magnitude of the gaps obtained increases as we move down from vanadium (V) through niobium (Nb) to tantalum (Ta) in group 5 elements of the periodic table.

5.2.3 Mechanical properties

Table 5.6 gives the predicted mechanical properties of the sulvanite compounds ranging from the bulk (B), shear (G) and Young's modulus (E), independent elastic coefficients (C_{ij}), Frantsevich's ratio (G/B), Zener anisostropic factor (A), Kleinman internal-displacement parameter (ζ) as well as Poisson's ratio (ν), sound velocity (v_m) and Debye temperature (Θ_D) along with the Vicker's hardness index (H_ν) in comparison with other existing theoretical values. The computed mechanical properties of Cu_3QSe_4 sulvanites such as bulk, shear and Young's modulus as well as the independent elastic coefficients are in agreement with those reported by Espinosa-García *et al.* [5].

These three materials are relatively soft compared to diamond based on their bulk modulus and elastic coefficients. It is evident from Table 5.6 that LDA gives an upper limit value of the mechanical properties of these sulvanites probably because of its overbinding nature, whereas PBE gives the lower limit. On the other hand, the PBEsol values are in between the LDA and PBE values. If the determined values of the independent elastic coefficients i.e C_{11}, C_{12} and C_{44} are substituted onto equation (4.8.1), it is clear that all the Born stability conditions for cubic systems will be fulfilled suggesting that Cu_3TaSe_4, Cu_3VSe_4 and Cu_3NbSe_4 are all mechanically stable.

Poisson's ratio (ν) is the proportion of the transverse compression to longitudinal extension strain in the direction of the stretching force. A value of between 0.22 and 0.28 of Poisson's ratio was attained implying that the quantity of longitudinal strain exceeds the transverse strain in Cu_3QSe_4 sulvanites. Since $\nu \approx 0.25$, these sulvanite compounds would likely experience the ionic type of bonding. Based on the obtained values of Frantsevich's ratio, Cu_3QSe_4 sulvanites are brittle ternary compounds, this is in line with what was reported before by Espinosa-García *et al.*, as previously stated in section 1.4. For all the three sulvanite compounds, across all the functionals considered, the values of the Zener anisotropy factor obtained are all less than unity implying that although these sulvanites are cubic by symmetry, they indeed possess some degree of elastic anisotropy, signifying that they respond differently to the applied strain along the various axes.

Low values of Kleinman parameter (ζ) obtained suggest that Cu_3QSe_4 shows a large resistance against bond-angle distortion [245]. From the values of Vicker's hardness index deduced across all the functionals, Cu_3TaSe_4 and Cu_3NbSe_4 have comparable values of ζ, that are slightly higher than those of Cu_3VSe_4, implying that Cu_3VSe_4 shows less resistance to deformation relative to Cu_3TaSe_4 and Cu_3NbSe_4. Remarkably, it was difficult to compare the sound velocities and the Debye temperatures of the three compounds due to the inconsistent trend of the data obtained as presented in Table 5.6.

Table 5.6: Mechanical properties of Cu_3QSe_4 sulvanites.

		Cu_3TaSe_4		Cu_3VSe_4		Cu_3NbSe_4	
Parameter	**Functional**	**Present**	**Theory** [j]	**Present**	**Theory** [j]	**Present**	**Theory** [j]
B (GPa)	LDA	45.18	44.20	49.76	46.80	46.46	44.90
	PBE	30.87	33.60	34.42	34.40	30.87	33.90
	PBEsol	39.76	39.10	40.45	40.50	39.51	39.60
G (GPa)	LDA	26.45	27.23	25.64	26.02	27.12	25.88
	PBE	20.61	21.99	21.75	21.10	20.74	22.50
	PBEsol	23.36	24.57	21.73	22.80	23.44	24.91
G/B (GPa)	LDA	0.59	0.62	0.52	0.56	0.58	0.58
	PBE	0.67	0.65	0.63	0.61	0.67	0.67
	PBEsol	0.59	0.63	0.54	0.56	0.59	0.63
E (GPa)	LDA	66.40	67.76	65.65	65.88	68.11	65.14
	PBE	50.58	54.14	53.90	52.54	50.83	55.26
	PBEsol	58.61	60.94	55.29	57.59	58.70	61.76
C_{11} (GPa)	LDA	93.44	93.20	92.93	92.10	97.11	95.70
	PBE	68.30	72.40	70.17	69.80	70.04	74.60
	PBEsol	84.60	83.50	80.69	81.10	86.47	85.90
C_{12} (GPa)	LDA	21.06	19.70	28.18	24.20	21.14	19.40
	PBE	12.16	14.10	16.55	16.30	11.28	13.50
	PBEsol	17.35	16.90	20.33	20.20	16.02	16.40
C_{44} (GPa)	LDA	21.40	22.20	21.93	21.70	21.59	19.9
	PBE	16.73	18.20	18.91	18.10	16.37	18.30
	PBEsol	18.24	20.0	17.40	18.80	17.74	19.90
A	LDA	0.59	0.60	0.67	0.60	0.57	0.50
	PBE	0.33	0.60	0.71	0.70	0.56	0.60
	PBEsol	0.54	0.60	0.57	0.60	0.50	0.60
ζ	LDA	0.38	-	0.45	-	0.37	-
	PBE	0.60	-	0.39	-	0.31	-
	PBEsol	0.36	-	0.40	-	0.34	-
ν	LDA	0.26	-	0.28	-	0.26	-
	PBE	0.23	-	0.24	-	0.22	-
	PBEsol	0.25	-	0.27	-	0.25	-
H_v (GPa)	LDA	4.33	-	3.21	-	4.29	-
	PBE	4.35	-	4.06	-	4.38	-
	PBEsol	3.82	-	2.89	-	3.83	-
v_t (m/s)	LDA	1985	2385	2119	2641	2151	2583
	PBE	1850	1933	2073	2047	1988	2096
	PBEsol	1903	2319	1991	2534	2040	2575
v_l (m/s)	LDA	3463	4068	3834	4644	3755	4463
	PBE	3113	3247	3540	3505	3339	3503
	PBEsol	3316	3933	3560	4433	3545	4358
	Others[k] (PBE)	3382	-	-	-	3651	-
v_m (m/s)	LDA	2205	2644	2361	2936	2390	2867
	PBE	2048	2140	2299	2270	2200	2320
	PBEsol	2114	2570	2216	2816	2265	2853
Θ_D (K)	LDA	236.94	285.00	257.82	321.00	256.96	309.00
	PBE	212.25	222.00	241.14	239.00	228.02	241.00
	PBEsol	224.19	273.00	238.69	304.00	240.29	303.00

j = Ref. [5] k = Ref. [52]

5.2.4 Dynamical properties of Cu_3QSe_4 sulvanites

Optimized structures were used in examining the vibrational properties since high precision in the structural relaxation with vanishing internal forces on each ion are essential to calculate reliable phonons within the harmonic approximation. According to our findings, Cu_3(Ta,V,Nb)Se_4 are all dynamically stable due to presence of only the positive vibrational frequencies (hard modes). Besides, Cu_3TaSe_4, Cu_3NbSe_4 and Cu_3VSe_4 have an acoustic cut-off limit of about 2.0, 2.0 and 2.1 THz respectively. This is the upper limit value of phonon frequency below which we have the acoustic phonon vibration modes and above which we have the optical phonon modes.

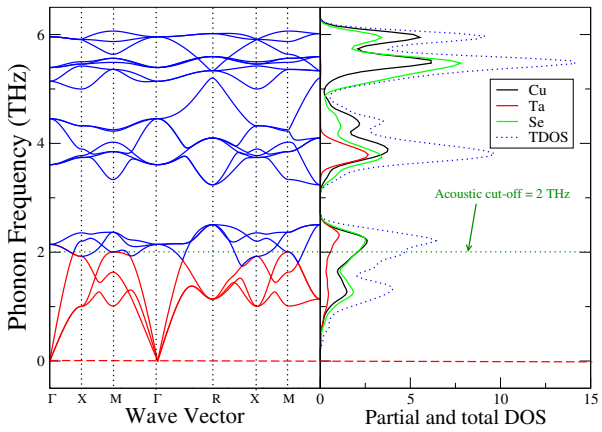

Figure 5.31: The phonon band structure together with partial and total density of states for Cu_3TaSe_4.

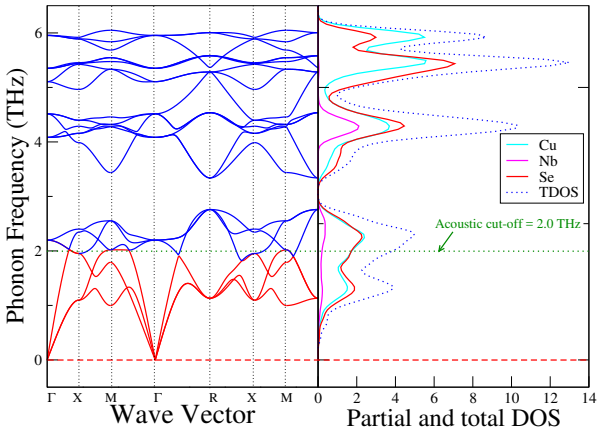

Figure 5.32: The phonon band structure together with partial and total density of states for Cu_3NbSe_4.

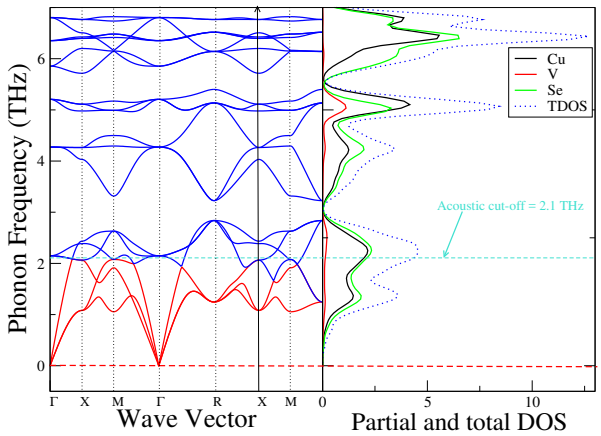

Figure 5.33: The phonon band structure together with partial and total density of states for Cu_3VSe_4.

In all the three sulvanites, copper and chalcogens (S, Se, Te) states dominates both the acoustic and the optical regions whereas the transition metals (Ta, V, Nb) contribution is suppressed especially at the acoustic zone. Furthermore, although the phonon band structures of Cu_3TaSe_4, Cu_3NbSe_4 and Cu_3VSe_4 are similar since they have the same crystal structures, some obvious difference is also noticeable in that there exist a phonon band gap at around 3 THz frequency whose size vary. We note that Cu_3TaSe_4 has a larger phonon band gap followed by Cu_3NbSe_4 whereas Cu_3VSe_4 shows the least. This could be attributed to the fact that the mass disparity of Ta and Se atom is quite large,

while it is relatively small in V and Se.

5.2.5 Thermal properties of Cu_3QSe_4 sulvanites

According to Figure 5.34, entropy increases as we move down the group 5 elements of the periodic table which consists of vanadium, niobium and tantalum that belongs to the transition metals; in that Cu_3TaSe_4 has the highest values of entropy (more disordered) followed by Cu_3NbSe_4, whereas Cu_3VSe_4 has the lowest values (less disordered) within the considered temperature range. From Figure 5.34, 5.35 and 5.36, at 300 K, the predicted values of entropy, Helmholtz free energy and specific heat capacity are 290.82 J/K/mol, -23.98 KJ/mol and 188.63 J/K/mol respectively for Cu_3TaSe_4.

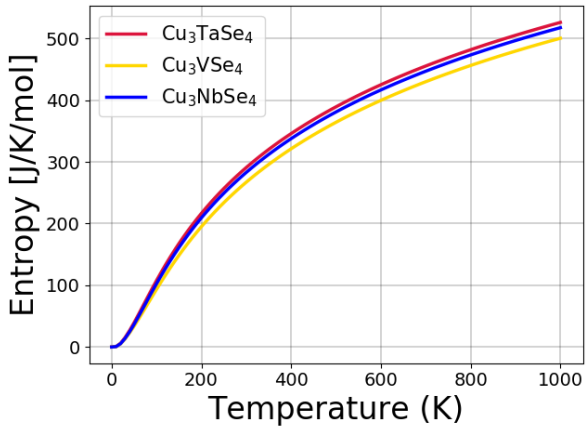

Figure 5.34: Entropy of Cu_3QSe_4.

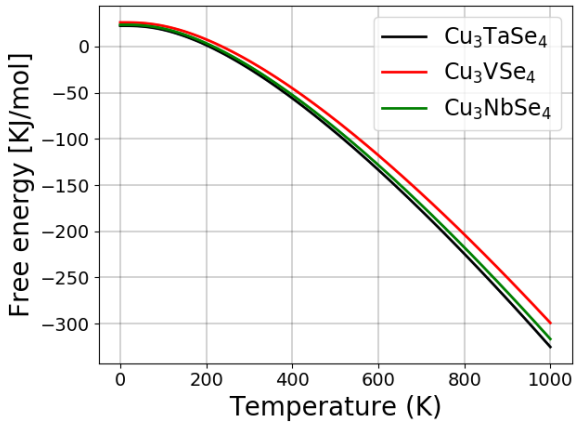

Figure 5.35: Helmholtz free energy of Cu_3QSe_4.

The values of entropy, Helmholtz free energy and specific heat capacity are 282.90 J/K/mol, -21.20 KJ/mol and 187.44 J/K/mol respectively for Cu_3NbSe_4 at room-temperature (300 K), whereas Cu_3VSe_4 had values of 267.06 J/K/mol, -15.56 KJ/mol and 184.77 J/K/mol for entropy, Helmholtz free energy and specific heat capacity respectively at 300 K. Additionally, below 600 K, specific heat capacity also increases as we move down the group 5 elements whereas at 800 K, the specific heat capacities of the three compounds attains saturation, whereby the Dulong-Petit limit is obtained be approximately 197.93 J/K/mol as shown in Figure 5.36.

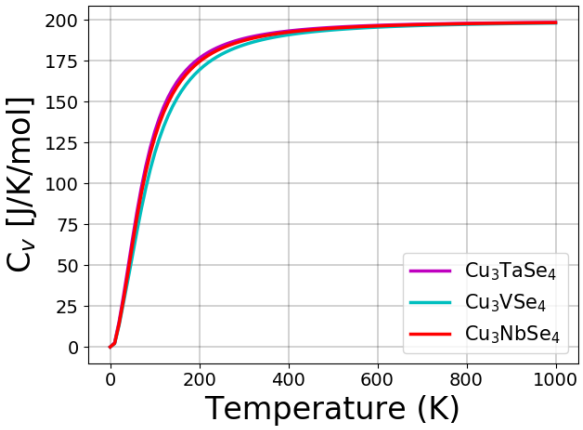

Figure 5.36: Specific heat capacity of Cu_3QSe_4.

In Figure 5.36, we see that the specific heat capacity is saturated at high temperatures (above Dulong-Petit limit), as compared to that at low temperatures which is associated with their vibrational behavior, in that at low temperatures the amount of generated heat energy could be insufficient to excite many high frequency phonons. On the other hand, most of the available phonon modes are already active in the high temperature range leading to the saturation of the specific heat capacity.

5.2.6 Lattice thermal conductivity of Cu_3QSe_4 sulvanites alongside its cumulative values

During the course of our study, we realized that the lattice dynamics of Cu_3QSe_4 sulvanites of interest have not yet been fully explored; hence besides evaluating their lattice thermal conductivity, we also assessed their group velocities, phonon lifetimes, mean free path as well as the Grüneisen parameters. Hence, we believe our findings will serve as a useful guide to lattice vibrations in these sulvanite compounds. Figure 5.37 indicates that lattice thermal conductivity in Cu_3QSe_4 sulvanites display similar behavior as that of entropy provided in Figure 5.34, in that the lattice thermal conductivity increases as we move down the group 5 elements of the transition metals, since Cu_3TaSe_4 possess slightly higher values of lattice thermal conductivity within (100-1000) K followed by Cu_3NbSe_4, whereas Cu_3VSe_4 had the least. We can also see from Figure 5.37 that the lattice thermal conductivity somewhat follows the T^{-1} relationship, decreasing with an increase in temperature.

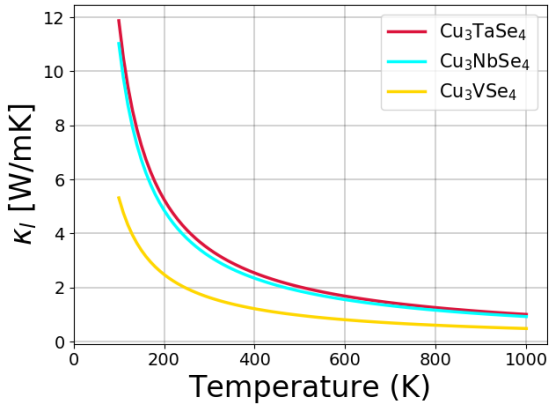

Figure 5.37: Calculated κ_l of Cu_3QSe_4.

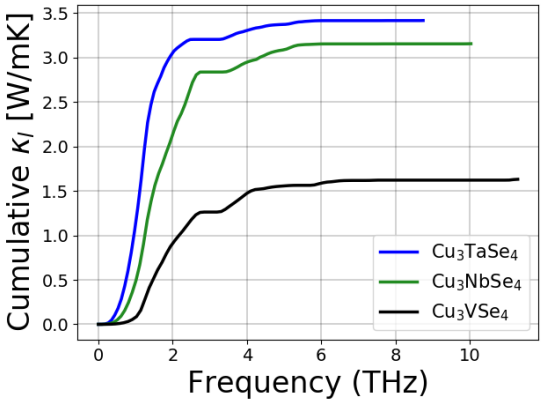

Figure 5.38: Cumulative κ_l of Cu_3QSe_4 at 300 K.

Additionally, Figure 5.38 of the cumulative lattice thermal conductivity against frequency (at 300 K) confirms that the lattice vibrations within the Cu_3QSe_4 sulvanites are primarily influenced by the acoustic modes in that above the acoustic cut-off limits (provided in section 5.2.4), the cumulative lattice thermal conductivity of the three ternary compounds becomes almost flat, implying the optical modes contribute mildly to the overall heat transfer mechanism in Cu_3QSe_4 sulvanites.

5.2.7 Group velocity, phonon lifetimes, mean free path and Grüneisen parameters of Cu_3QSe_4 sulvanites

The distribution of group velocities can explain the relative contributions of every acoustic and optical phonon mode to the total lattice thermal conductivity. According to Figure 5.39, we couldn't get a consistent trend of the behavior of group velocities for the three compounds as we traverse from Cu_3TaSe_4 to Cu_3VSe_4, but one striking feature that cuts across is that, the low frequency acoustic phonons had larger values of group velocity relative to the optical phonons, which backs our earlier statement that the acoustic modes predominates their heat transport. Hence, to get some insights on heat transport mechanisms in sulvanite compounds, we further examined their phonon lifetimes and mean free path.

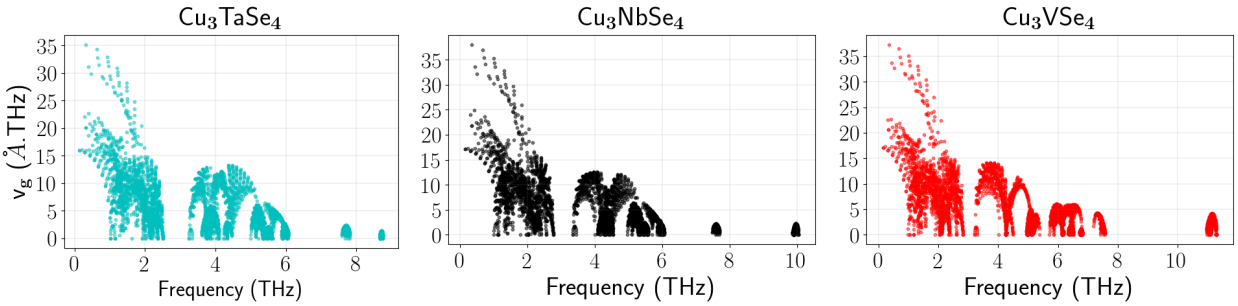

Figure 5.39: Group velocities of Cu_3QSe_4.

From Figure 5.40 and 5.41, there is a decrease in the magnitude of the phonon lifetimes and mean free path as we move from Cu_3TaSe_4 through Cu_3NbSe_4 to Cu_3VSe_4; with the maximum lifetimes being about 66, 44 and 38 picoseconds respectively. For the case of the mean free path, the highest values

are approximately 2375, 680 and 320 nanometers (nm) for Cu_3TaSe_4, Cu_3NbSe_4 and Cu_3VSe_4 respectively signifying that at the low frequency regime, atoms of Cu_3TaSe_4 travels a larger distance before colliding with each other as compared to the case of Cu_3VSe_4, this might have emerged due to mass differences between Ta and V. These can provide some insights on why Cu_3TaSe_4 possess a higher thermal conductivity followed by Cu_3NbSe_4 and Cu_3VSe_4 bearing the least value, possibly due to direct proportionality between the lattice thermal conductivity and phonon lifetimes and consequently the mean free path, as discussed in section 4.8.12.

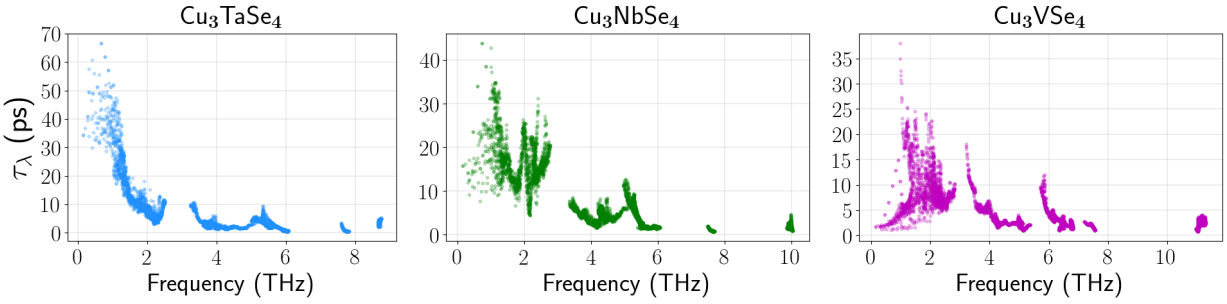

Figure 5.40: Phonon lifetimes of Cu_3QSe_4.

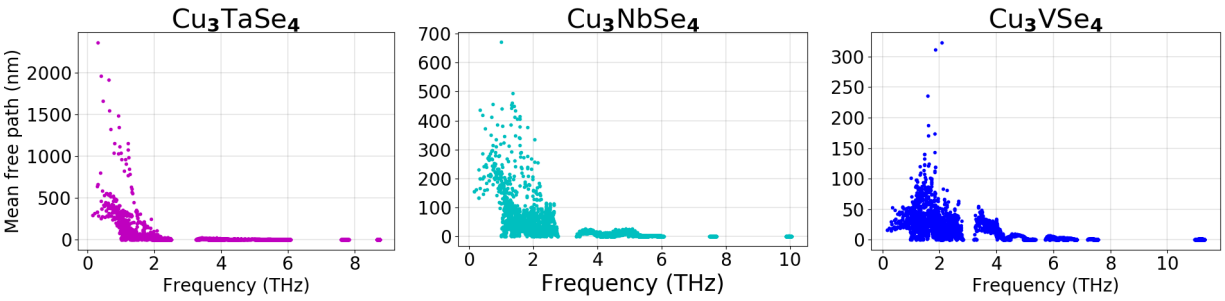

Figure 5.41: Comparison of mean free path of Cu_3QSe_4.

Considering that the lattice thermal conductivity is mainly an anharmonic phenomenon, we provide in Figure 5.42 the analysis of the mode resolved Grüneisen parameters in Cu_3QSe_4 sulvanites. The small Grüneisen parameter in Cu_3VSe_4 relative to Cu_3NbSe_4 and Cu_3TaSe_4 indicates a weak anharmonicity, leading to the high thermal conductivity as approved by Figure 5.37; as a larger γ signifies strong anharmonicity resulting in a lower lattice thermal conductivity. Besides, according to Figure 5.43, below 3 THz (acoustic regime), Cu_3TaSe_4 has a larger degree of mean free path as compared to the other two sulvanites, which also substantiate why the lattice thermal conductivity of Cu_3TaSe_4 exceeds the other two.

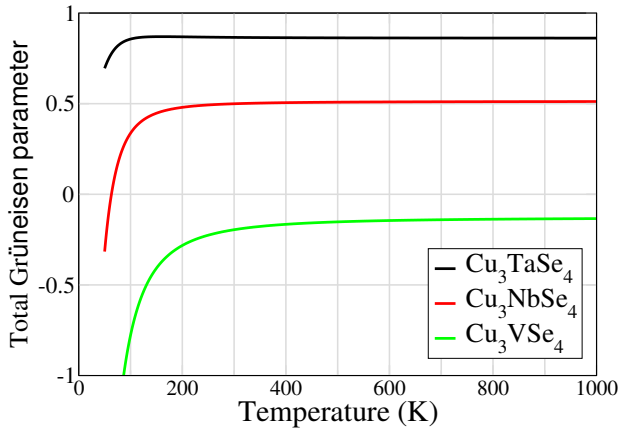

Figure 5.42: Total Grüneisen parameter of Cu_3QSe_4.

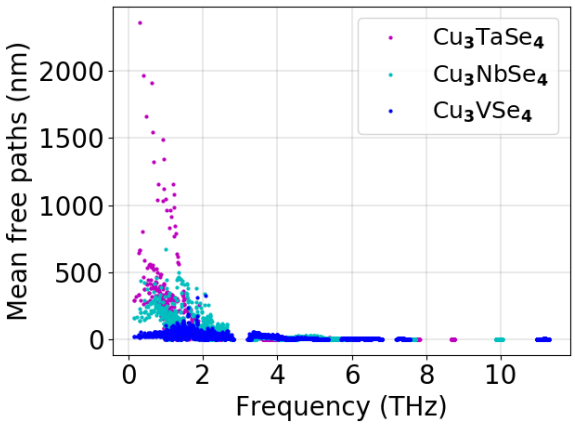

Figure 5.43: Mean free path of Cu_3QSe_4.

5.3 Optical properties

Typically, the electronic behavior of a material can be categorized into two types; that is the electronic ground states which can be well replicated at the DFT level and the electronic excited states which are obtained more accurately at the BSE level of approximation. The latter describes the demeanor of the electron-hole pair (exciton), upon being optically excited when the material being probed absorbs a photon. In this study, the DFT eigen-energies were used to initiate the GW calculations and subsequently the BSE within the many body pertubation theory approach, since DFT fails to accurately describe the excited state behavior of materials [246].

In this thesis, the main goal of carrying out the BSE calculations is to obtain the optical gaps of the Cu_3QSe_4 sulvanites, which is a crucial additive when determining the location of the band edges of potential photocatalytic material as outlined in section 3.1. Upon obtaining the real and imaginary parts of the dielectric function after doing the optical calculations, one can extract the values of the optical spectra such as the absorption coefficient, refractive index, extinction coefficient and reflectivity among others. Our main focus is to deduce the optical gaps of the three sulvanite compounds as discussed in section 5.3.1 underneath, a detailed procedure and description of the optical behavior of materials is also provided in our previous work [142].

5.3.1 Determination of optical gaps for bulk sulvanites using Tauc fits

Equation (5.3.1) provides the relationship between the absorption strength, photon energy and optical band gap of a material [247]. The region near the band edge region of the optical spectra is fitted into a simple expression in order to extract the band gap size from the intercept.

$$[\alpha h\nu]^{\frac{1}{n}} = A(h\nu - E_g); \tag{5.3.1}$$

where α denotes the absorption coefficient, h is the Planck's constant, ν is the photon's frequency, n stands for the nature of the electronic transition, A is a constant of proportionality and E_g is the optical band gap. The parameter n can take several values depending on the nature of electronic transition; such that $n = \frac{1}{2}$ implies direct allowed transition, $n = \frac{3}{2}$ implies direct forbidden transition,

$n = 2$ implies indirect allowed transition whereas $n = 3$ is for indirect forbidden transition. Thus, when the photon energy, which is a product of Planck's constant and the photon frequency ($E = h\nu$) is zero in the optical spectra, one can extract the value of the optical gap of the material under study using Tauc fits since all the other components of equation (5.3.1) vanishes except E_g. Therefore, the intercept of the *x*-axis of Tauc plot gives the optical band gap value.

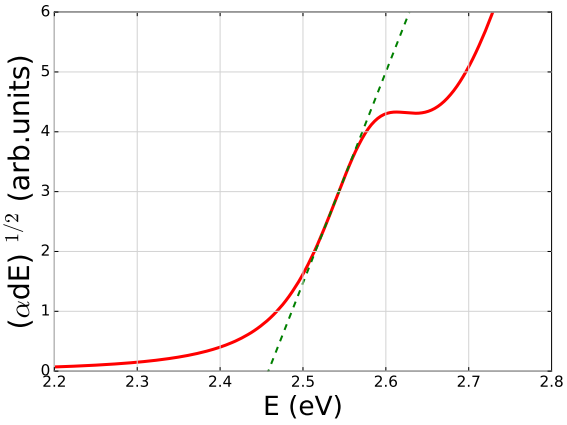

Figure 5.44: Determination of optical gap of Cu_3TaSe_4.

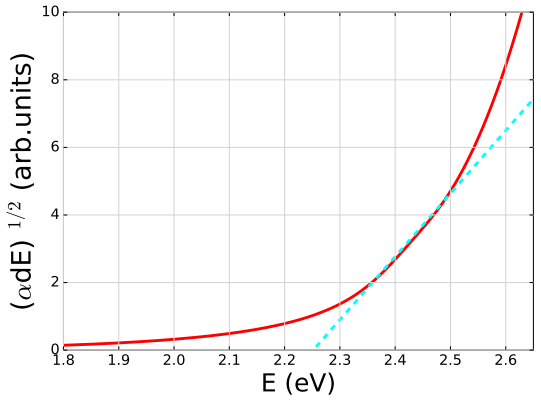

Figure 5.45: Determination of optical gap of Cu_3NbSe_4.

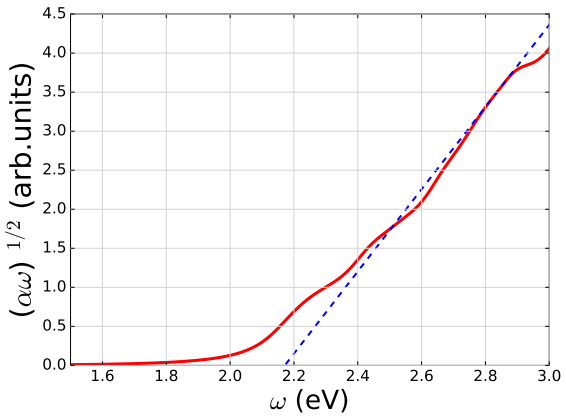

Figure 5.46: Determination of optical gap of Cu_3VSe_4.

Upon applying the Tauc procedures, the obtained values of the calculated optical gaps at BSE level of approximation are 2.17, 2.26 and 2.46 eV for Cu_3VSe_4, Cu_3NbSe_4 and Cu_3TaSe_4 respectively as shown by Figure 5.44, 5.45 and 5.46, where the intercept of the straight line portion with the abscissa defines the optical gap. The values of the optical gaps obtained from our Tauc plots are comparable to the ones reported experimentally for the case of Cu_3TaSe_4 and Cu_3NbSe_4 [7]. Conversely, the optical gap of Cu_3VSe_4 has not been reported so far, hence this study will serve as the first attempt. Moreover, the optical band gaps of Cu_3QSe_4 sulvanites lies within the visible range of the electromagnetic spectrum, which is desirable in photocatalytic applications as it leads to improved efficiency by harvesting a large portion of the solar spectrum.

5.4 Determination of surface energy in Cu_3TaSe_4

Apart from obtaining the surface energy from the differences between slab and bulk energies according to equation (3.2.1), one can as well obtain the bulk total energy from the slope of the slab total energy versus the number of layers in the slab, thus ensuring that the surface and bulk energies are extracted with the same accuracy as proposed by Fiorentini and Methfessel [248]. The latter approach is what we applied, in which the bulk total energies of the 100, 110 and 111 surface slabs of Cu_3TaSe_4 were deduced from Figure 5.47.

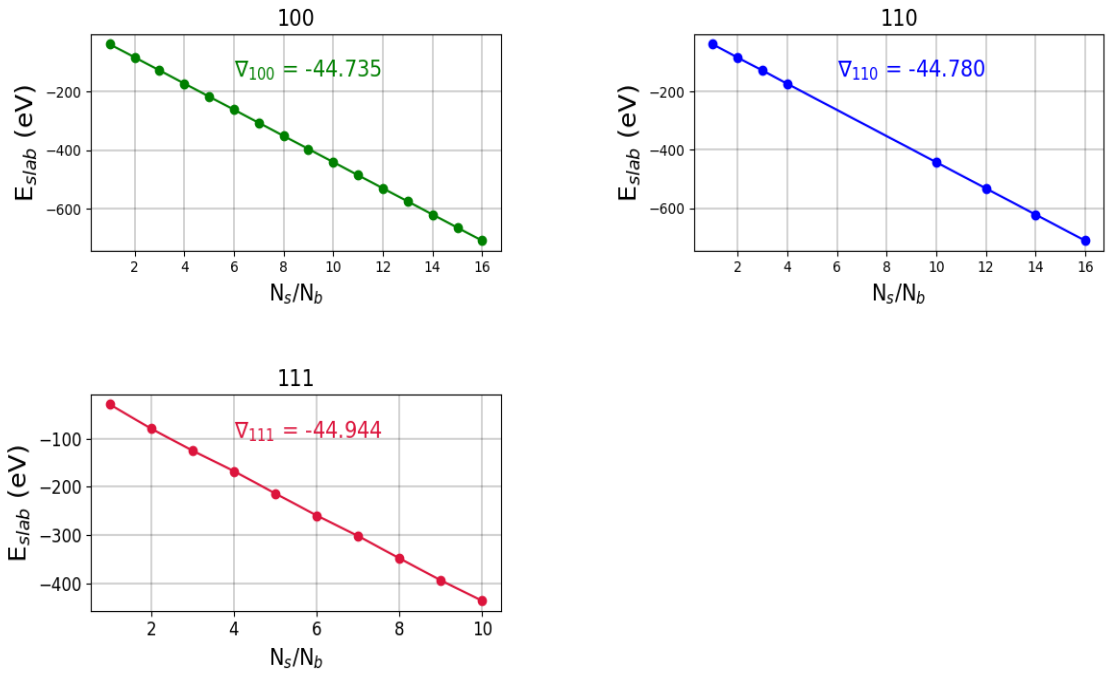

Figure 5.47: Determination of the bulk energy of Cu_3TaSe_4 from linear plots for various surface orientations.

The evaluated values of bulk energies obtained from the slopes along the various orientations were -44.735, -44.780 and -44.944 eV respectively for 100, 110 and 111 slabs. These values were applied in computing the surface energy for their respective crystal orientations as per equation (3.2.1). Upon determining the respective values of total energies of the bulk system of Cu_3TaSe_4, the next task is to carry out the slab size convergence.

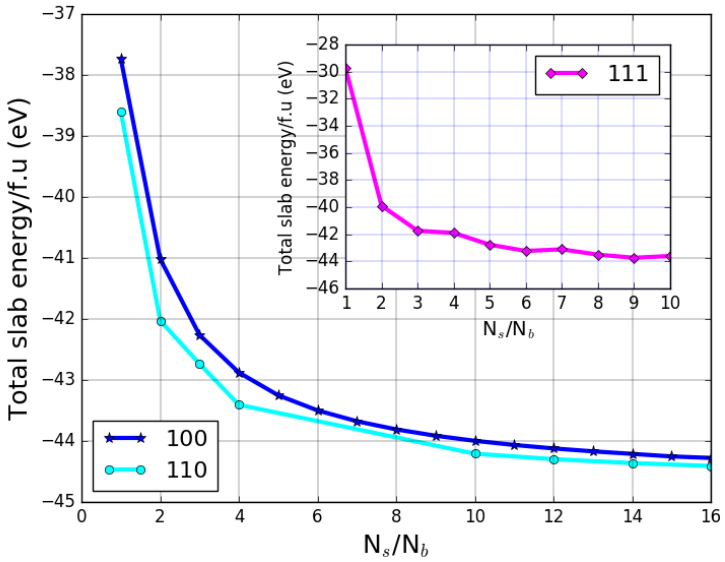

Figure 5.48: Total slab energy per formula unit convergence with respect to the slab size.

According to Figure 5.48; 14, 14 and 10 filled slab layers were found sufficient for surface study of Cu_3TaSe_4 along the 100, 110 and 111 orientations respectively as backed by their corresponding plots consisting of 112, 112 and 80 atoms in the same order within the slab, since each filled slab had 8 atoms. At this stage, the next task is to compute the optimal value of the vacuum to be imposed in the study of the three low index surface orientations of Cu_3TaSe_4, keeping the value of slab size strictly to the converged ones for each orientation. Upon doing this, we obtained the displayed surface energies as well.

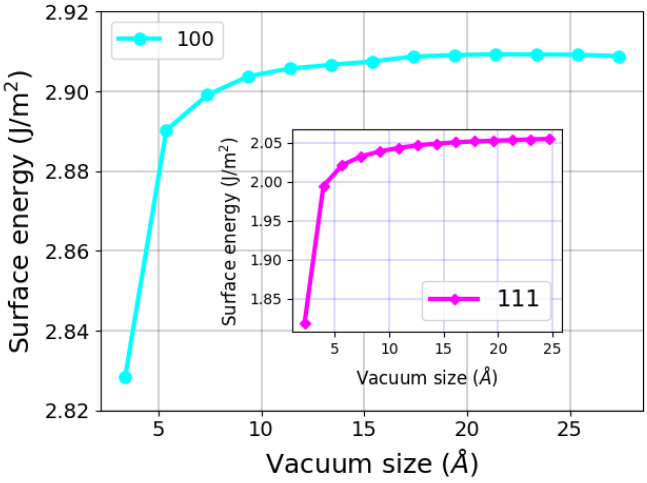

Figure 5.49: 100 and 111 surface energy convergence.

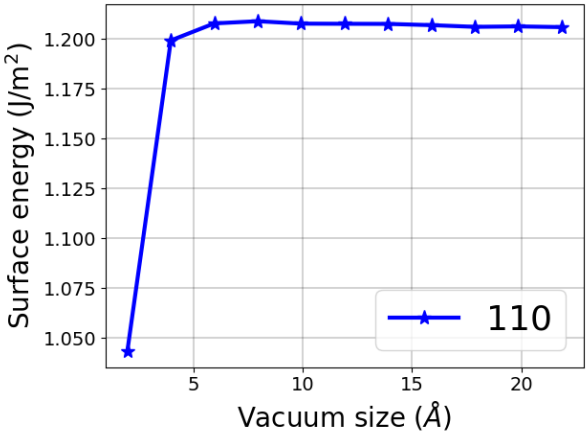

Figure 5.50: 110 surface energy convergence.

From Figure 5.49 and 5.50, 110 surface orientation had the lowest surface energy, hence more stable as compared to 100 and 111 orientations ($\gamma_{110} < \gamma_{111} < \gamma_{100}$) with their corresponding surface energies being 1.21, 2.05 and 2.91 J/m^2. Based on our numerical data, it takes relatively less energy of about 1.21 J/m^2 to create a 110 surface compared with 2.91 J/m^2 to create 100 surface and 2.05

J/m^2 to create 111 surface of Cu_3TaSe_4. The stability of a particular surface depends on the interplay of the surface characteristic quantities, such as the surface energy, surface stress and surface elastic constants [249]. Therefore, further surface studies on Cu_3TaSe_4 were conducted for only 110 orientation consisting of 14 filled slab layers with 112 atoms in total, for which a vacuum size of 16 Å was found to be sufficient to separate the periodic images along the direction perpendicular to the surface as per Figure 5.50.

5.5 Determination of surface energy in Cu_3VSe_4

For the case of Cu_3VSe_4 sulvanite, the values of total energy of the bulk systems were obtained from the linear fits of Figure 5.51 to be -41.620, -44.663 and -41.731 eV for the low index 100, 110 and 111 orientations respectively. This provided the first ingredient required for determination of the surface energies via the first principles approach.

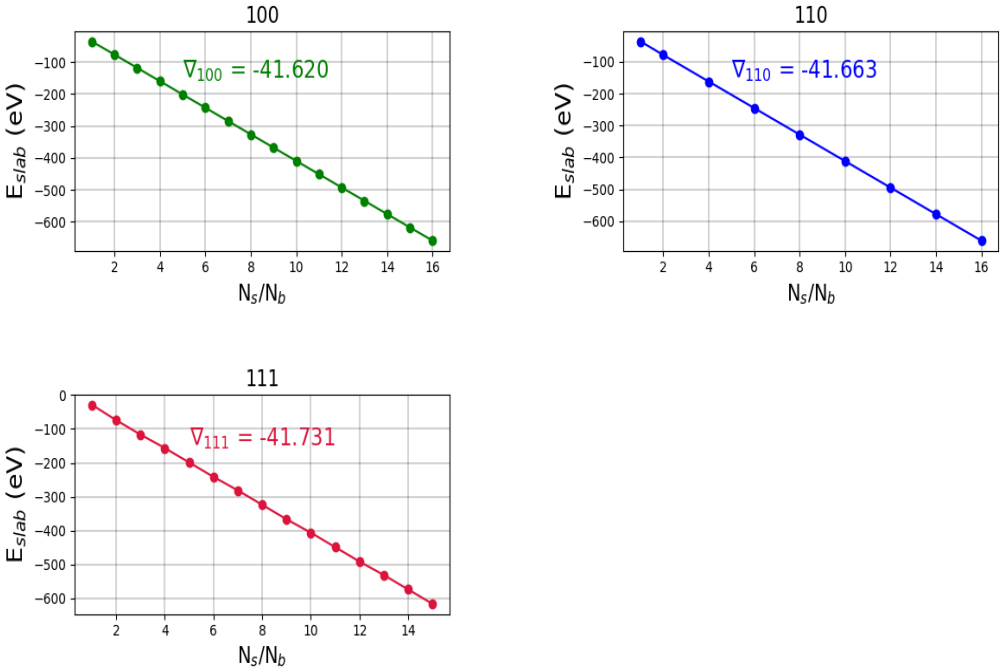

Figure 5.51: Determination of the bulk energy of Cu_3VSe_4 from linear plots for various surface orientations.

Having achieved this, we then examined the behavior of total slab energy (for the three orientations) with varying number of slab thickness as presented in Figure 5.52.

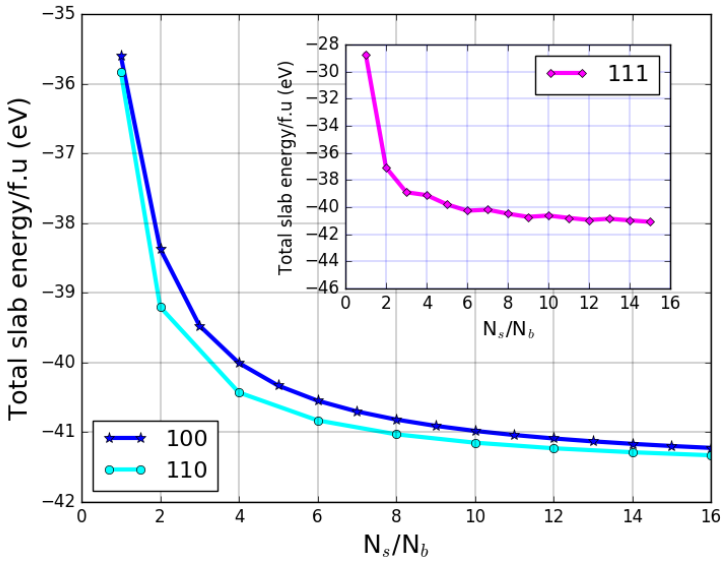

Figure 5.52: Total slab energy per formula unit convergence with respect to the slab size.

From the convergence test; 14, 14 and 10 filled slabs were deemed sufficient, having 112, 112 and 80 atoms respectively for 100, 110 and 111 surface geometries of Cu_3VSe_4. By ensuring that the converged values of slab thickness are adhered to, we then assessed the behavior of surface energies upon increasing the vacuum size for the orientations of interest, where a value of 18 Å was found sufficient to ensure that the interactions between the layers are negligible for the case of 111 geometry, whereas a vacuum size of about 10 Å was believed to be sufficient for both the 100 and 110 orientations. The obtained optimized values of the surface energies were 2.71, 1.13 and 1.78 J/m^2 respectively for 100, 110 and 111 surfaces as supported by Figure 5.53 and 5.54. This signify that relatively small energy is required to slice the bulk system of Cu_3VSe_4 sulvanite along the 110 direction than slicing it along 100 and 111 low index orientations. It also affirm that, 110 surface is relatively more stable than the other two.

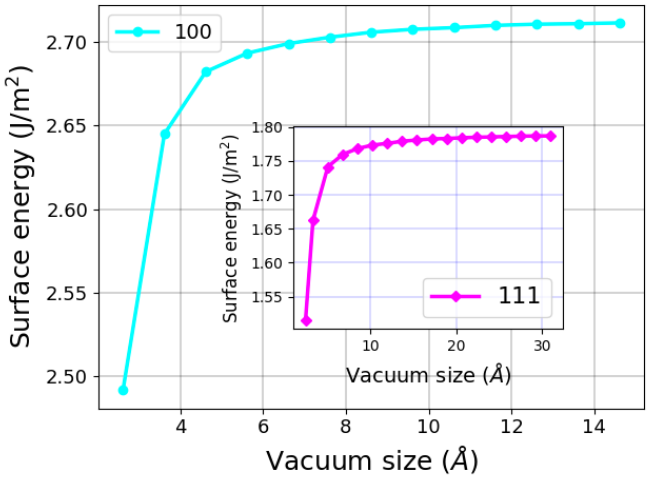

Figure 5.53: 100 and 111 surface energy convergence.

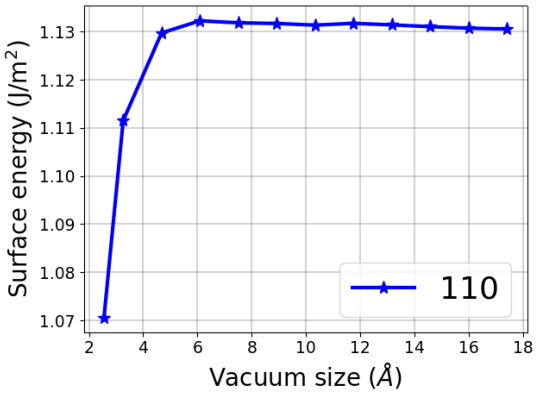

Figure 5.54: 110 surface energy convergence.

5.6 Determination of surface energy in Cu_3NbSe_4

Figure 5.55 present the values of the total slab energies against the number of filled slab layers, upon which the corresponding values of the bulk energy of the Cu_3NbSe_4 sulvanite were determined from their corresponding slopes to be -43.015, -43.054 and -43.202 eV along the 100, 110 and 111 orientations, respectively.

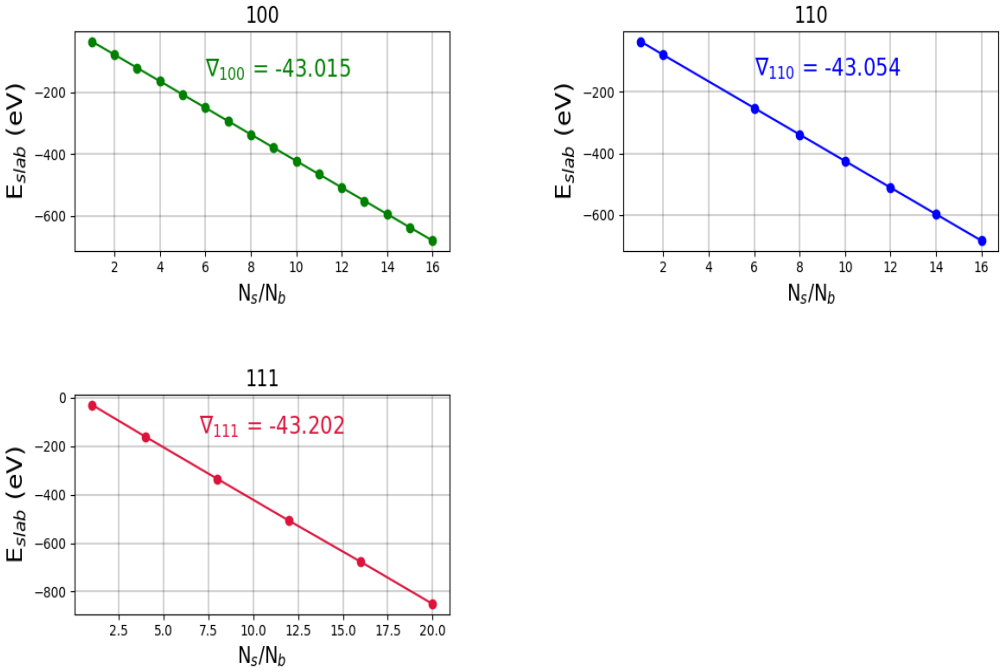

Figure 5.55: Determination of the bulk energy of Cu_3NbSe_4 from linear plots for various surface orientations.

Figure 5.56 display the convergence of the total slab energy per formula unit with respect to the slab sizes for Cu_3NbSe_4. We determined that at least 14, 14 and 12 filled slab layers corresponding to 112, 112 and 96 atoms are required along 100, 110 and 111 surface orientation to ensure that the slab is thick enough to avoid interaction between the two surfaces of one slab.

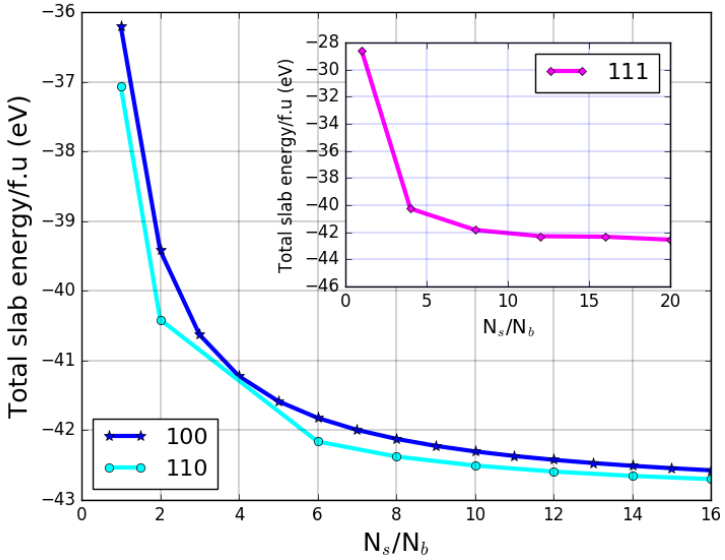

Figure 5.56: Total slab energy per formula unit convergence with respect to the slab size.

Subsequently, having obtained an optimized value of the filled layers for each orientation, we thereafter evaluated the behavior of the surface energies of various orientations upon increasing the vacuum size until we reach the point where the slabs decouple such that they are no longer interacting with each other, which is the point beyond which the surface energy becomes independent of the vacuum size. For Cu_3NbSe_4, vacuum sizes of 12, 16 and 8 Å were established to be satisfactory for separating slabs from their periodic images along the 100, 110 and 111 orientations as supported by Figure 5.57 and 5.58. By resolving the optimized vacuum size, it also culminated to determination of surface energies of Cu_3NbSe_4, where values of 2.77, 1.16 and 2.07 J/m^2 were extracted for 100, 110 and 111 surface geometries, respectively.

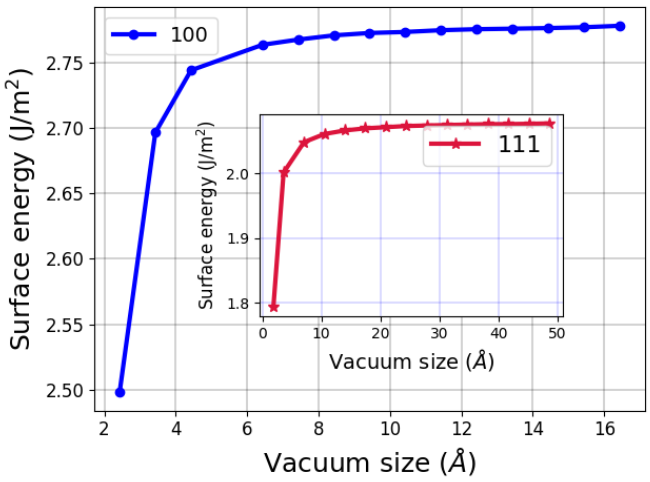

Figure 5.57: 100 and 111 surface energy convergence.

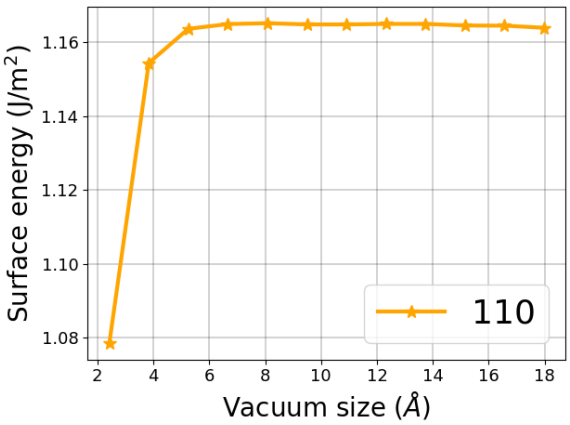

Figure 5.58: 110 surface energy convergence.

5.7 Wulff construction

Wulff theorem states that the distance from the center of a particle to the surface is proportional to the surface energy. Thus, the equilibrium shape of a crystal is related to the surface energies through the Wulff construction. This is a standard way of quantifying information of surface energies in different orientations to depict thermodynamic stability by displaying relative energetics of surfaces and the lower in energy a surface is, the more area the facet contributes to the Wulff shape [250]. The smaller the surface energy is, the easier the surface will form. The Wulff construction yields the equilibrium shape of a particle of fixed volume embedded in a single phase at a constant temperature [251]. Besides being a descriptor of relative surface stability, surface energy also plays a crucial role in controlling the rate of sintering, growth of particles as well as determining their morphology. It is also a vital entity in industrial applications such as adhesion, lubrication and protective coating [252].



(a) Cu_3TaSe_4 **(b)** Cu_3VSe_4 **(c)** Cu_3NbSe_4

Figure 5.59: Predicted equilibrium shape of sulvanite crystals using Wulffman program. Due to large differences in the predicted values of surface energies, only 110 facet appears in the morphology.

Wulff construction dictates a particle shape given its orientation-dependent surface free energy [253]. The Wulffman program along with the Geomview interactive 3D visualization software was used to reveal the theoretical equilibrium shape of the sulvanite crystals as provided in Figure 5.59. Note that the Wulff construction represents the ideal shape that the crystal would take in the absence of other possible constraints [254].

5.7.1 Mid gap states in Cu_3QSe_4 sulvanites along the 110 surface

We also computed the total as well as the partial density of states for the most stable surface geometries in order to deeply verify if indeed the surface states are present, which could be attributed to the disruption of the three-dimensional periodicity of the crystal along the direction perpendicular to the surface. This had been elaborated in section 4.6. From Figures 5.60, 5.62 and 5.64, bulk- and surface-related spectral features are easily distinguishable (indicated with the grey background), it is evident that there is surface transitions from the localized surface states of the 110 surfaces of Cu_3QSe_4 sulvanites.

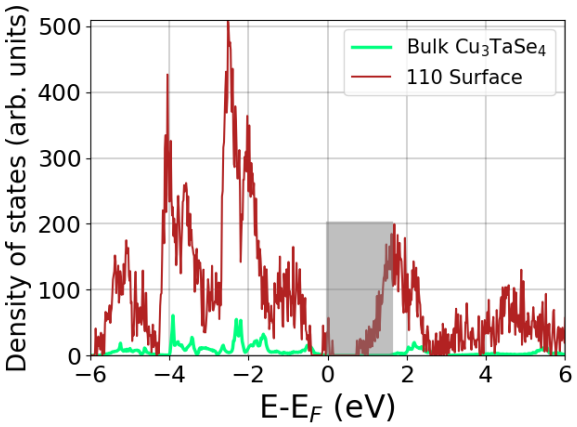

Figure 5.60: Surface and bulk DOS for Cu_3TaSe_4.

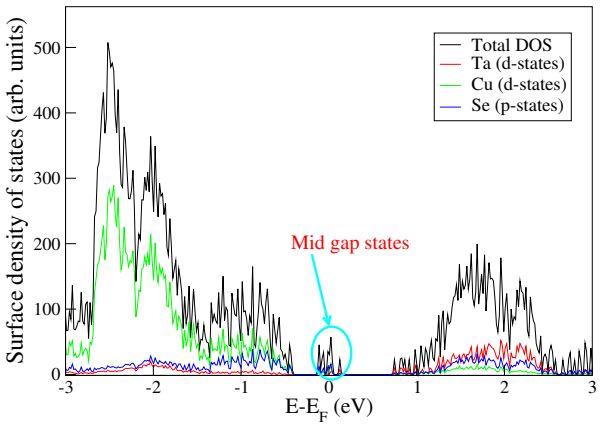

Figure 5.61: Surface density of states for Cu_3TaSe_4.

In the field of solid states physics, it is worth exploring the electronic properties of the surface from the density functional theory approach to get in-depth information about the elemental states responsible for the creation of the localized surface states. From Figure 5.61, we observe that there are midgap states existing in 110 surface of Cu_3TaSe_4 that were absent in the bulk counterparts and the major contributors to these surface states are from d-states of tantalum and copper as well as p-states of selenium. Similar behavior is noticeable in Figures 5.63 and 5.65.

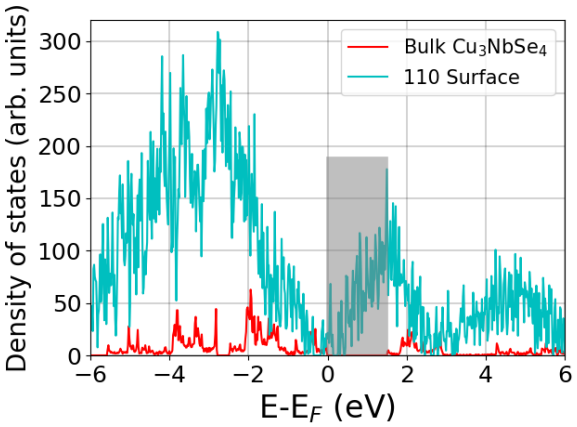

Figure 5.62: Surface and bulk DOS for Cu_3NbSe_4.

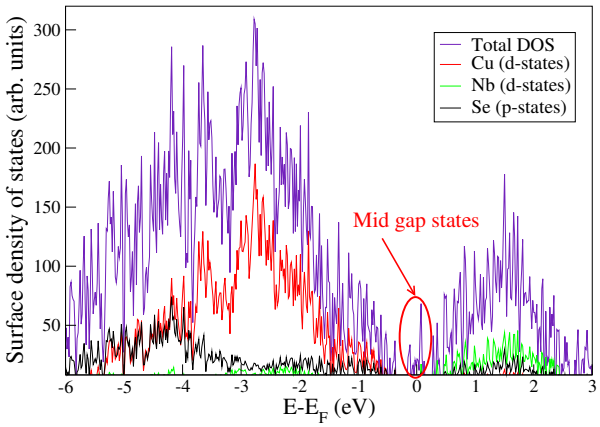

Figure 5.63: Surface density of states for Cu_3NbSe_4.

These gap states present at the surface band structures of Cu_3QSe_4 sulvanites are considered to be the active sites for photocatalytic reaction [255], in that they act as the trapping centers for the photogenerated charge carriers. Thus, minimize the chances of recombination occurring hence ensuring that the electron and hole have more possibility to interact with the reactant. Consequently, by retarding the recombination, presence of abundant localized surface states boosts the overall photocatalytic activity of a system by prolonging the lifetime of the carriers [256].

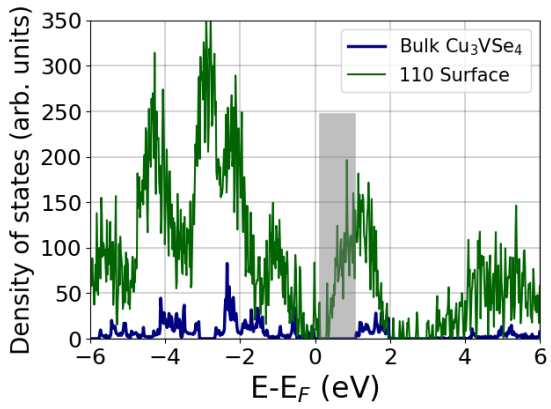

Figure 5.64: Surface and bulk DOS for Cu_3VSe_4.

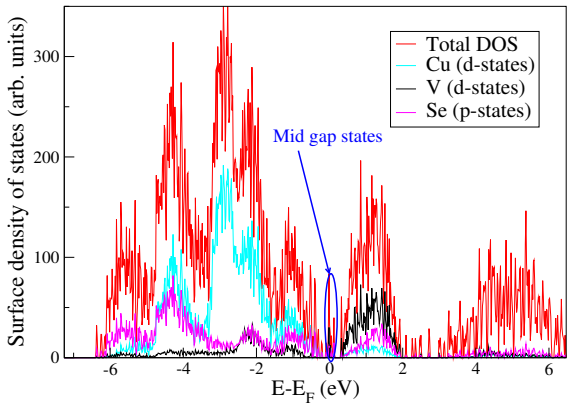

Figure 5.65: Surface density of states for Cu_3VSe_4.

5.8 Charge density difference via Bader analysis

As stated in section 3.3.2, in this study, Bader analysis was used to examine the electron density distribution on the most stable surface of the sulvanite compounds, that is the 110 orientation. The knowledge of charge distributions can be used to resolve how molecules interact with one another. The mechanism of charge migration from the interior to the surface of the semiconductor is quite complicated because it is dominated by many factors such as the crystal structures together with crystallinity, lattice vibration modes, electronic structures, lifetime of the photo-generated carriers and grain boundary effects among others [257].

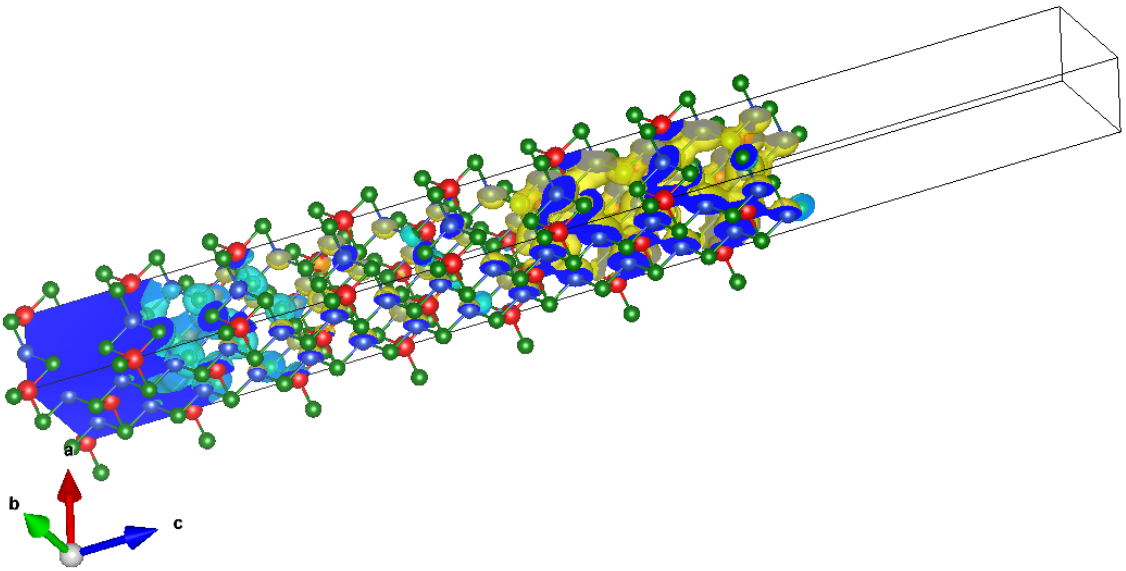

Figure 5.66: The charge density difference in Cu_3QSe_4 with the volumetric sections.

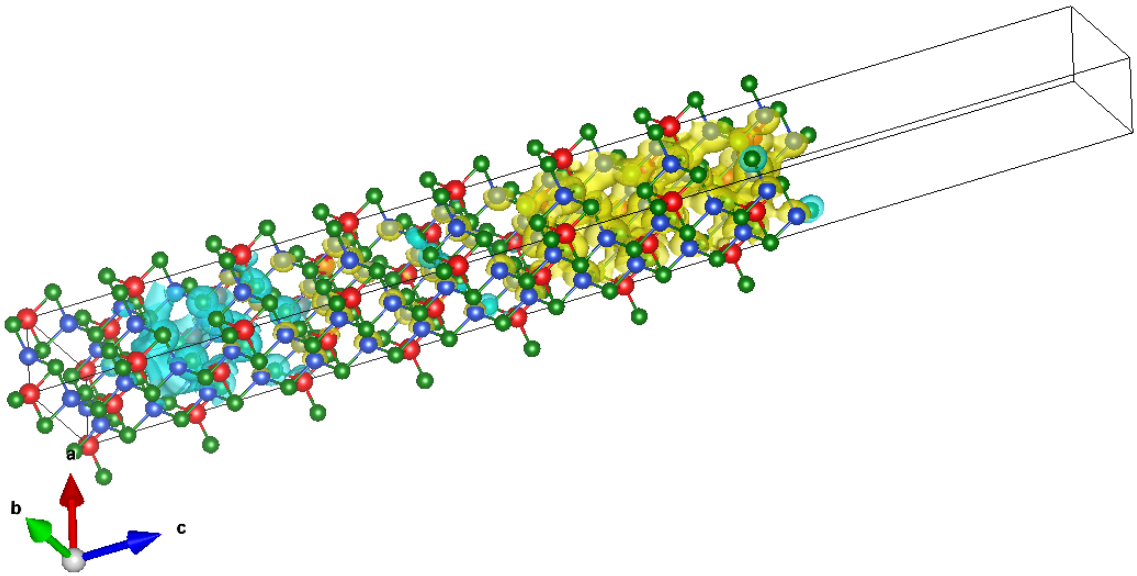

Figure 5.67: The charge density difference in Cu_3QSe_4 without the volumetric sections.

The above Figures (5.66 and 5.67) show the charge density difference of Cu_3QSe_4 as created using Visualization for Electronic and Structural Analysis program (VESTA) [258] when the iso-surface level is set to 0.05 e/Bohr^3. The red atoms are for transition metals (i.e Ta, V, Nb), the blue atoms are for copper whereas the green atoms are for the selenium. It is visible that the charge is mainly concentrated on copper atoms at the top of the surface along the z-axis as indicated by the yellow color. On the other hand, a lot of charge is depleted on the transition metal and selenium atoms at the lower part as indicated by the cyan color. According to Simfukwe *et al.* [259], the accumulation of charges on the surface of a material is likely to decrease the recombination rate of the photogenerated charge pairs, which in turn boosts its photocatalytic activity in the Cu_3QSe_4 sulvanite compounds.

5.9 Determination of work function in Cu_3QSe_4 sulvanites

For the most stable surface orientation for each of the sulvanite compounds considered, we computed their corresponding vacuum potential, Fermi level and work function along the 110 orientation which is the preferred cleavage plane for the three sulvanite compounds as indicated in Figure 5.68 and summarized in Table 5.7.

Table 5.7: Cu_3QSe_4 surface properties for the stable 110 orientation.

Compound	Fermi level (eV)	vacuum potential (eV)	work function (eV)
Cu_3TaSe_4	0.96	5.91	4.95
Cu_3VSe_4	1.20	6.17	4.97
Cu_3NbSe_4	1.20	6.03	4.83

From Table 5.7, Cu_3NbSe_4 possess a lower magnitude of work function implying that electrons can be dislodged with ease from its surface, as materials that have a low work function emit electrons easily.

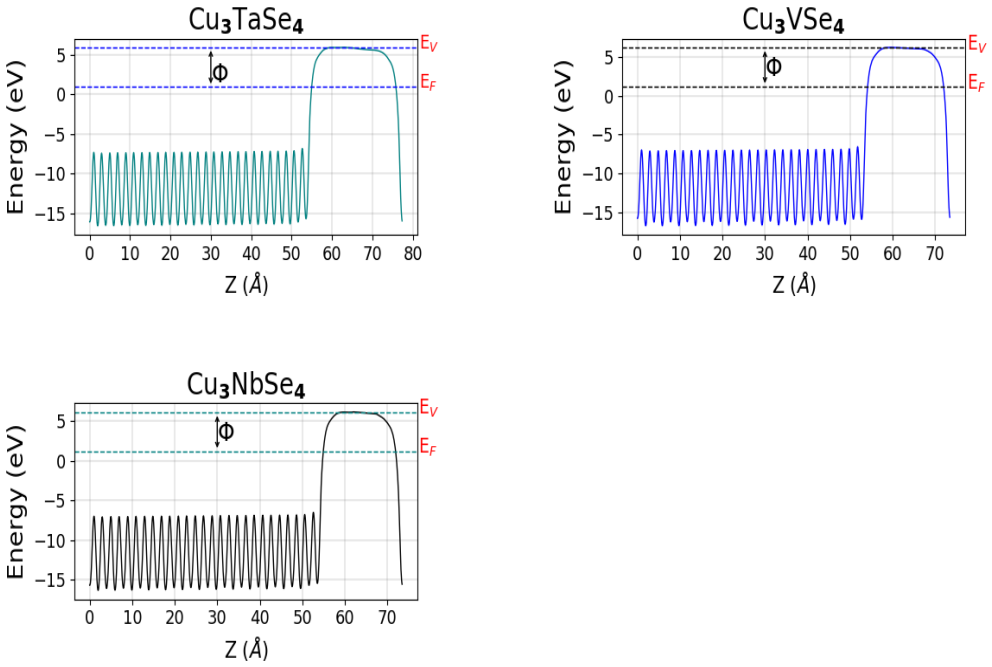

Figure 5.68: Determination of work function of Cu_3QSe_4 from vacuum potential and Fermi level for various surface orientations. The electrostatic potential was averaged in the *x*- and *y*-directions to get the potential along the *z*-direction.

5.10 Determination of band edge location using Mulliken approach

The electronegativity of an atom is the arithmetic mean of the atomic electron affinity and the first ionization energy [260].

Table 5.8: Pearson absolute electronegativity values for elements of interest.

Element	Absolute electronegativity, χ (eV) [145]
Copper	4.48
Tantalum	4.11
Vanadium	3.60
Niobium	4.00
Selenium	5.89

The values of the absolute electronegativities of the individual elements provided in Table 5.8 were applied in determining the values of the absolute electronegativity of their corresponding sulvanite compounds as per equation (3.1.3), where the absolute electronegativities of Cu_3TaSe_4, Cu_3VSe_4 and Cu_3NbSe_4 were obtained to be 5.08, 5.00 and 5.06 eV respectively. These were then applied in determining the band edge locations via the Mulliken approach as tabulated in Table 5.9.

Table 5.9: Band alignment in Cu_3QSe_4 via Mulliken approach.

Compound	χ (eV)	E_e (eV)	E_g (eV)	E_{VB} (V)	E_{CB} (V)
Cu_3TaSe_4	5.08	4.50	2.46[Q]	1.81	-0.62
Cu_3TaSe_4	5.08	4.50	2.43 [7]	1.80	-0.63
Cu_3TaSe_4	5.08	4.50	2.35 [8]	1.76	-0.59
Cu_3VSe_4	5.00	4.50	2.17[Q]	1.59	-0.58
Cu_3NbSe_4	5.06	4.50	2.14 [7]	1.63	-0.51
Cu_3NbSe_4	5.06	4.50	2.26[Q]	1.69	-0.57

[Q] = Optical gaps from Tauc fits in the present study

The calculated band edges were then compared to the redox potentials of the reactions of interest to evaluate their photocatalytic capabilities. The bottom of the conduction band (E_{CB}) is more negative than the H^+/H_2 redox potential [0 V] vs NHE at zero PH (or the electron potential should be more positive than -4.5 eV vs the vacuum level). The top of the valence band (E_{VB}) is more positive than the O_2/OH^- redox potential [+1.23 V] vs NHE at zero PH. (or more negative than -5.73 eV vs the vacuum level). The obtained values of the E_{VB} (E_{CB}) via Mulliken approach relative to NHE potential are 1.81 (-0.62), 1.59 (-0.58) and 1.69 (-0.57) V for Cu_3TaSe_4, Cu_3VSe_4 and Cu_3NbSe_4 respectively, implying the reactions leading to photogeneration of hydrogen and oxygen will be thermo-dynamically favorable as presented in Figure 5.69.

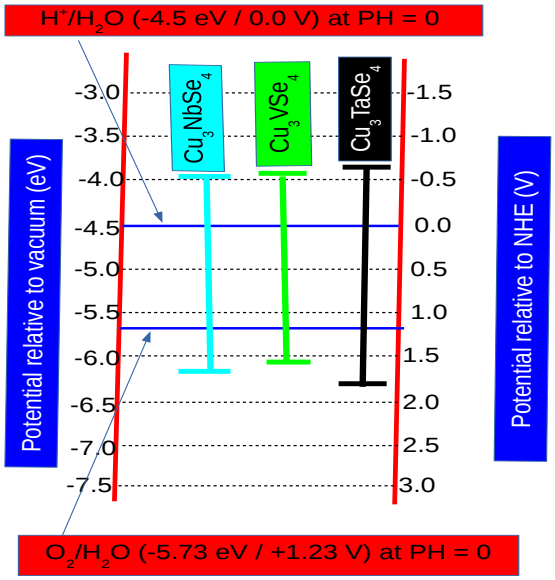

Figure 5.69: Alignment of the band edges using Mulliken approach at PH = 0.

5.10.1 Determination of band edge location via BGC approach

For the case of band gap center approach, Perdew and Levy [148] observed that one can accurately predict the value of the band gap center energy at the DFT level of approximation and reference the

eigenvalues to the computed value of the vacuum potential determined from the surface calculations. Therefore, having already determined the optical band gaps of Cu_3QSe_4 sulvanites of interest as provided in section 5.3.1 along with the values of the vacuum potentials provided in Table 5.7, we then computed carefully the values of the valence band maxima and the conduction band minima at the DFT level for the most stable surface geometries that is 110 for the three sulvanites, from which the obtained results are displayed in Table 5.10.

Table 5.10: Cu_3QSe_4 band edges based on BGC approach.

Compound	E_g (eV)	E_{vac} (eV)	BGC (eV)	E_{VBM} (eV)	E_{CBM} (eV)
Cu_3TaSe_4	2.46	5.91	-4.74	-5.97	-3.51
Cu_3VSe_4	2.17	6.17	-4.76	-5.84	-3.67
Cu_3NbSe_4	2.26	6.03	-4.65	-5.78	-3.52

From our findings, the comparison of the band edges to redox potential reveals that all the three Cu_3QSe_4 sulvanites are certainly thermodynamically viable for photocatalytic applications. This present work indicates that Cu_3QSe_4 sulvanites are promising photocatalysts that are sensitive to sunlight for water splitting to generate hydrogen. Favorably, since these sulvanites have suitable placement of their band edges with respect to the redox (reduction and oxidation) potentials of water as shown in Figure 5.70, there is no need to provide supplementary external bias in order to overcome the thermo-dynamic energy barrier so as to initiate the photocatalytic activity. Besides the appropriately positioned band edges, Cu_3QSe_4 sulvanites absorbs light in the visible region, which in turn ensures that they harvest a large portion of the solar spectrum, leading to enhanced efficiency in photocatalytic generation of H_2O as a useful energy carrier.

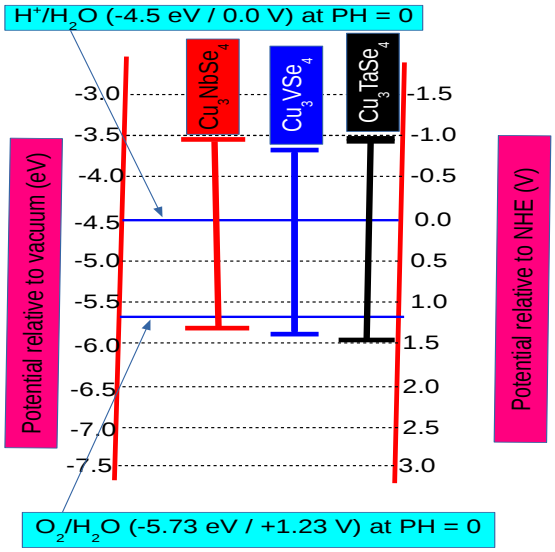

Figure 5.70: Position of the band edges using BGC approach at PH = 0.

6

CONCLUSIONS

In summary, we have successfully carried out extensive studies on the photocatalytic properties of sulvanite-type compounds $Cu_3(V,Nb,Ta)Se_4$ and thermoelectric properties of spinel oxides $Cd(Ga,Al)_2O_4$ in line with clean energy production based on first principles approach. In Chapter 1, we have discussed the dangers posed by the inevitable global energy crisis to humanity which forms the motivation of our current study. We have also provided the aim and the specific objectives which the current study was geared towards achieving. Additionally, we have presented the scope of the thesis as well as what has been explored and the existing gaps to be filled in exploring our compounds of interest - sulvanites and spinels. In Chapter 2, we have discussed the previously reported work on sulvanites and spinels of interest and also deliberated on the basic scientific ideas about photocatalysis and thermoelectricity as well as presented the aspect of material choices to be considered and the possible areas of applications. In Chapter 3, we have delved onto a flavor of density functional theory principles that are directly related to the current study such as lattice dynamics, transport and surface aspect of the study. In Chapter 4, we have furnished a step by step guide on how computations and analysis were carried out. In Chapter 5, we have presented, analyzed and discussed the obtained results as well as compared them with previously reported data.

From our findings; concerning the $Cd(Ga,Al)_2O_4$ spinels, it was recognized that the LDA functional reproduced its ground state properties relative to existing experimental data. Moreover, these spinels are thermodynamically and mechanically stable. They were deduced to be ductile showing some degree of elastic anisotropy and the magnitude of their bond stretching is much smaller compared to bond bending and are dominated by metallic type of bonding. We found out that $CdGa_2O_4$ had higher magnitude of average sound velocity than $CdAl_2O_4$, implying sound travels faster in $CdGa_2O_4$ than in $CdAl_2O_4$. Being cubic by symmetry, these spinels display thermal, lattice and transport isotropy.

At 300 K, $CdGa_2O_4$ and $CdAl_2O_4$ possess lattice thermal conductivity of 9.381 and 10.485 W/mK respectively, which seems not promising for thermoelectric applications, where small values of κ_l are desirable and the dominant contributor to lattice thermal conductivity is acoustic phonon modes. In order to understand their heat transport mechanisms, we have examined their group velocity, phonon lifetimes, mean free path as well as modal Grüneisen parameter. Upon doing the transport analysis, $CdGa_2O_4$ and $CdAl_2O_4$ have low predicted values of dimensionless figure of merit of about 0.049 and 0.040 respectively at higher temperatures (1000 K), implying they have a very low efficiency in converting thermal to electrical energy and vice versa which doesn't call for any further substantial exploration as it is, unless the strategies to reduce κ_l and/or enhance ZT are implemented such as creation of nanostructures, defects and straining among others.

For the case of Cu_3QSe_4 sulvanites, PBEsol functional mimicked their ground state properties well, they are also dynamically and mechanically stable compounds whose bonds are dominated by ionic type. Converse to spinels, Cu_3QSe_4 sulvanites are brittle. Their low values of Kleinman parameter suggest that they have a large resistance against bond-angle distortion. From their electronic band structures, we observed that there are midgap states existing in their stable 110 surfaces that were absent in the bulk counterparts.

These localized surface states acts as trapping centers for the photogenerated charge carriers which in turn minimizes the rate of recombination enhancing the photocatalytic activity. As it is well known that DFT underestimates the bandgaps of semiconductors, to counter this, we computed the optical gaps at the BSE level applying the Tauc procedures. The values of the approximate gaps obtained are 2.17, 2.26 and 2.46 eV for Cu_3VSe_4, Cu_3NbSe_4 and Cu_3TaSe_4 respectively. For the three systems, among their low index orientations, 110 surface had relatively the lowest surface energies of 1.13, 1.16 and 1.21 J/m^2 respectively; with their corresponding values of work function being 4.97, 4.83 and 4.95 eV for Cu_3VSe_4, Cu_3NbSe_4 and Cu_3TaSe_4, respectively. Besides having appropriate gap values for single photon water splitting, these sulvanite compounds have favorably aligned band edges that are able to straddle the water redox potentials in absence of external bias, as substantiated by our results obtained via the band gap center and the Mulliken approach.

In a nutshell, through our first principles studies we have confirmed that our hypotheses were partly true in that from our findings, Cu_3QSe_4 sulvanites indeed show the viability to breakdown water onto hydrogen and oxygen since their band edges bridge the reaction redox potentials of water, which is favorable towards clean energy generation. This calls for further experimental probe, since our *ab initio* analysis gave positive results in this aspect.

APPENDIX

In this section, we provide supplementary information related to our current study such as: the approximations and convergence in density functional theory where we discuss two crucial parameters namely k-points and wave function plane wave expansion. We also look at the importance of incorporating dipole correction when undertaking surface probe, how Bader charge was analyzed and the effect of PH on the redox potential of water, as well as an outline of the few articles that arose during the course of this work.

Approximations and convergence in density functional theory

According to Choudhary and Tavazza [261], although density functional theory is exact in theory, its implementation requires several approximations such as the choice of basis set, exchange-correlation functionals, mesh-size of Brillouin zone integration and plane wave cut-off for plane wave basis. In section 4.2, we have briefly discussed how convergence is done in *ab initio* calculations. We wish to elaborate k-points and cut-off energy herein.

K-points

The Brillouin zone plays a central role in band theory of materials. Hence, one of the objectives when undertaking convergence test is to select a sufficiently dense mesh for the integration of the Brillouin zone as this is in long run crucial for the convergence of the results within the desired precision. Note that the mesh size varies depending on the system under study, for instance metallic systems require more k-points than semiconductors and insulators. According to VASP manual [262], insulators require 100 k-points/per atom in the full Brillouin zone in order to sufficiently reduce the energy error to less than 10 meV, whereas metals require approximately 1000 k-points/per atom to achieve the same accuracy.

Moreover, the k-point grid required depends on the nature of the system under consideration and is dictated by the smearing method chosen. Choudhary and Tavazza [261] also noted that high symmetry systems such as cubic and hexagonal materials require higher k-points, but lower cut-off, whereas low symmetry structures such as triclinic materials require fewer k-points but higher cut-off. Also, for systems with broken symmetry one has to consider dispersion i.e., for slab/surface calculations with the z-axis as the surface normal, one has to ensure the k-point grid lie in xy-plane only since there is no dispersion in the z-axis.

Wave function plane wave expansion

For crystalline systems, it is convenient to choose plane waves as the basis set for expanding their wave functions due to periodicity of the system. According to Bloch theorem [263];

$$\psi(\mathbf{r}) = \sum_{\mathbf{k}} \; exp(i\mathbf{k}.\mathbf{r}) u_{\mathbf{k}}(\mathbf{r}); \tag{6.0.1}$$

where the eigen-states of the wave function of an electron in a periodic potential consists of a cell periodic part denoted by $u_{\mathbf{k}}(\mathbf{r})$ and a varying phase factor. Equation (6.0.1) can be rearranged to form equation (6.0.2), since $u_{\mathbf{k}}(\mathbf{r})$ is periodic hence can be expanded with plane waves.

$$u_{\mathbf{k}}(\mathbf{r}) = \sum_{\mathbf{G}} C_{\mathbf{Gk}} \; exp(i\mathbf{G}.\mathbf{r}); \tag{6.0.2}$$

where **G** are the points on the reciprocal lattice. Then the wave function can be expanded in pure plane waves by summing equation 6.0.1 and 6.0.2 as;

$$\psi(\mathbf{r}) = \sum_{\mathbf{G},\mathbf{k}} C_{\mathbf{Gk}} \; exp[i(\mathbf{G}+\mathbf{k}).\mathbf{r})]. \tag{6.0.3}$$

Due to computational constraints, the summation with respect to **G** cannot be performed to infinity, hence this summation is often truncated after some **G** which is determined to be converged based on the value of cut-off energy.

$$E_{cut} = \frac{|\mathbf{K}+\mathbf{G}|^2}{2}. \tag{6.0.4}$$

In other words, plane waves are infinite in number, hence one has to deduce how many plane waves are sufficient for obtaining accurate eigenvalues. This optimum number of basis functions is determined by the kinetic cut-off energy provided in equation 6.0.4. Truncation becomes handy since computational resources are often inadequate to handle a large number (infinite) of plane waves and one has to trade-off between rigor and computational cost.

According to Sholl and Steckel [264], it is reasonable to expect that the solutions with lower energies are more physically important than solutions with very high energies. Therefore, it is usual to truncate the infinite sum to include only solutions with optimal cut-off value. Additionally, plane wave cut-off are strongly correlated to the chosen pseudo-potential. In principle, pseudo-potentials are used to reduce computation time by replacing the full electron system in the coulombic potential by a system only taking explicitly into account the valence electrons. This not only reduces the electron number but also the energy cut-off [264], which is crucial in plane wave based codes such as VASP [51].

Dipole correction

In *ab initio* calculations, it is not completely possible to impose a sufficient vacuum layer in order to decouple the interactions within the slabs as doing this will make surface studies to be computationally demanding. Moreover, the artificial periodic images may still interact through coulomb interaction as noted by Li [265]. To solve this, we applied the dipole correction as implemented in VASP by invoking the IDIPOL, which switches on monopole/dipole correction to the total energy, ensuring that the latter as well as the forces on the surface atoms within the slab converge more rapidly with respect to the vacuum thickness, since the eigen values and the vacuum potential and consequently the work function changes as a function of the vacuum size.

Effect of PH on redox potential of water

The degree of acidity or basicity of the photocatalytic reaction system also plays a role in water splitting reaction since the band levels often shift with a change in PH, hence is worth to consider so as to ensure that the water oxidation and reduction potential are accurately determined, and are related through the following expressions [266]:

$$E^{\text{red}}_{H^+/H_2} = \Big[(0.059 \star \text{PH}) - E_e\Big]\ eV. \tag{6.0.5}$$

$$E^{\text{ox}}_{O_2/H_2O} = \Big[(0.059 \star \text{PH}) - (E_e + 1.23)\Big]\ eV. \tag{6.0.6}$$

Bearing in mind that water is neither acidic nor basic (neutral), we also cross-checked if the band edges of Cu_3QSe_4 sulvanites are still capable to straddle the redox potential of water when the system is at a neutral environment having a PH of 7, as indicated in Figure 6.1 and 6.2. Which was established to be achievable making them promising candidates for photocatalytic water splitting with no bias voltage required.

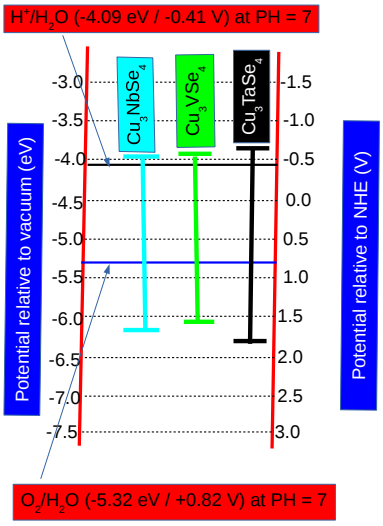

Figure 6.1: The effect of PH on redox potential of water via Mulliken approach at PH of 7.

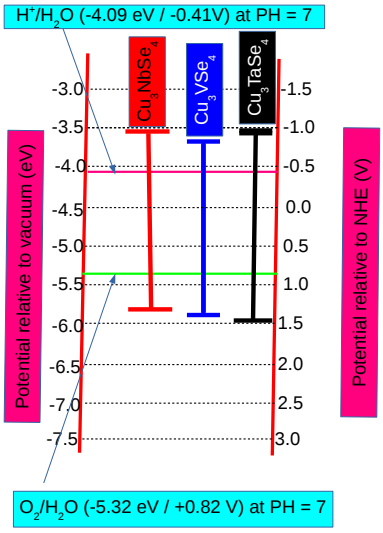

Figure 6.2: The effect of PH on redox potential of water via BGC approach at PH of 7.

Bader analysis

In our case, by adding the LAECHG tag in the INCAR (a cental input file in VASP); we obtained separately the core and valence charges, which were then summed up as indicated in equation (6.0.7) and then visualized using VESTA software as discussed in section 5.8. The charge difference ($\Delta\rho$) was attained by applying equation (6.0.8) as the difference in charge magnitude between the parent compound (that is Cu_3QSe_4) and its fragments which are the constituting elements.

$$\rho^{total} = \rho^{core} + \rho^{valence} \tag{6.0.7}$$

$$\Delta\rho = \rho^{compound} - \rho^{fragments} \tag{6.0.8}$$

Publications

The following articles arose during the course of this work:

1. Elkana Rugut, Daniel Joubert and Glenn Jones, **Numerical simulation of structural, electronic and optical properties of vanadium diselenide (VSe_2)**-South Africa Institute of Physics 2017.
2. Elkana Rugut, Daniel Joubert and Glenn Jones, **Thermoelectric properties of $CdGa_2O_4$ spinel**-South Africa Institute of Physics 2018.
3. Elkana Rugut, Daniel Joubert and Glenn Jones, **First principle studies on lattice thermal conductivity and thermoelectric properties of $LiYSe_2$**-South Africa Institute of Physics 2019.
4. Mahmoud Mahmoud, Elkana Rugut, Mahlaga Molepo and Daniel Joubert, **Study of structural electronic and thermoelectric properties of potassium chalcogens KX (X = S, Se, and Te): Ab-Initio Approach**-*under preparation*.
5. Mahmoud Mahmoud, Elkana Rugut, Mahlaga Molepo and Daniel Joubert, **First-principles study of structural stability, electronic properties and lattice thermal conductivity of KAgX (X= S, Se, Te)**-The European Physical Journal B, **92** (2019).
6. Elkana Rugut, Daniel Joubert and Glenn Jones, **Lattice dynamics and thermoelectric properties of $YCuSe_2$**- Materials Today Communications, **21** (2019).
7. Elkana Rugut, Daniel Joubert and Glenn Jones, **First principle studies on lattice thermal conductivity and thermoelectric properties of $ScCu(S,Se,Te)_2$**-*under preparation*.
8. Elkana Rugut, Daniel Joubert and Glenn Jones, **Structural stability, surface and photocatalytic properties of $CdGeP_2$: A DFT study**-*under preparation*.

References

[1] N. Abas, A. Kalair, and N. Khan, "Review of fossil fuels and future energy technologies," *Futures*, vol. 69, pp. 31–49, 2015.

[2] P. Gautam, S. Kumar, and S. Lokhandwala, "Energy-aware intelligence in megacities," in *Current Developments in Biotechnology and Bioengineering*, pp. 211–238, Elsevier, 2019.

[3] S. Ozturk, A. Sozdemir, and O. Ulger, "The real crisis waiting for the world: Oil problem and energy security," *International Journal of Energy Economics and Policy*, vol. 3, no. 4S, pp. 74–79, 2013.

[4] K. Bhattarai, W. M. Stalick, S. Mckay, G. Geme, and N. Bhattarai, "Biofuel: an alternative to fossil fuel for alleviating world energy and economic crises," *Journal of Environmental Science and Health, Part A*, vol. 46, no. 12, pp. 1424–1442, 2011.

[5] W. Espinosa-García, C. Ruiz-Tobón, and J. Osorio-Guillén, "The elastic and bonding properties of the sulvanite compounds: A first-principles study by local and semi-local functionals," *Physica B: Condensed Matter*, vol. 406, no. 20, pp. 3788–3793, 2011.

[6] G. E. Delgado, A. J. Mora, S. Durán, M. Munoz, and P. Grima-Gallardo, "Structural characterization of the ternary compound Cu_3TaSe_4," *Journal of Alloys and Compounds*, vol. 439, no. 1, pp. 346–349, 2007.

[7] P. Grima-Gallardo, M. Salas, O. Contreras, C. Power, M. Quintero, H. Cabrera, I. Zumeta-Dubé, A. Rodríguez, J. Aitken, and W. Brämer-Escamilla, "Cu_3TaSe_4 and Cu_3NbSe_4: X-ray diffraction, differential thermal analysis, optical absorption and raman scattering," *Journal of Alloys and Compounds*, vol. 658, pp. 749–756, 2016.

[8] P. Newhouse, P. Hersh, A. Zakutayev, A. Richard, H. Platt, D. Keszler, and J. Tate, "Thin film preparation and characterization of wide band gap Cu_3TaQ_4 (Q= S or Se) p-type semiconductors," *Thin Solid Films*, vol. 517, no. 7, pp. 2473–2476, 2009.

[9] R. Nitsche and P. Wild, "Crystal growth and electro-optic effect of copper-tantalum-selenide, Cu_3TaSe_4," *Journal of Applied Physics*, vol. 38, no. 13, pp. 5413–5414, 1967.

[10] A. B. Kehoe, D. O. Scanlon, and G. W. Watson, "The electronic structure of sulvanite structured semiconductors Cu_3MCh_4 (M= V, Nb, Ta; Ch= S, Se, Te): prospects for optoelectronic applications," *Journal of Materials Chemistry C*, vol. 3, no. 47, pp. 12236–12244, 2015.

[11] S. Curtarolo, W. Setyawan, G. L. Hart, M. Jahnatek, R. V. Chepulskii, R. H. Taylor, S. Wang, J. Xue, K. Yang, O. Levy, *et al.*, "AFLOW: an automatic framework for high-throughput materials discovery," *Computational Materials Science*, vol. 58, pp. 218–226, 2012.

[12] A. Van Arkel and C. Crevecoeur, "Quelques sulfures et séléniures complexes," *Journal of the Less Common Metals*, vol. 5, no. 2, pp. 177–180, 1963.

[13] Y. Du, Z. Sun, H. Hashimoto, and W. Tian, "First-principles study on thermodynamic properties of Ti_2AlC and Ti_2SC," *Materials Transactions*, vol. 50, no. 9, pp. 2173–2176, 2009.

[14] A. Hong, C. Yuan, G. Gu, and J.-M. Liu, "Novel p-type thermoelectric materials Cu_3MCh_4 (M= V, Nb, Ta; Ch= Se, Te): high band-degeneracy," *Journal of Materials Chemistry A*, vol. 5, no. 20, pp. 9785–9792, 2017.

[15] R. L. Cunha, I. E. Gouvea, and L. Juliano, "A glimpse on biological activities of tellurium compounds," *Anais da Academia Brasileira de Ciências*, vol. 81, no. 3, pp. 393–407, 2009.

[16] R. M. Navarro Yerga, M. C. Álvarez Galván, F. Del Valle, J. A. Villoria de la Mano, and J. L. Fierro, "Water splitting on semiconductor catalysts under visible-light irradiation," *Chemistry & Sustainability Energy & Materials*, vol. 2, no. 6, pp. 471–485, 2009.

[17] A. M. Y. Mohamed *et al.*, *Photodegradation of malachite green molecules using CuO photocatalyst*. PhD thesis, Sudan University of Science and Technology, 2016.

[18] P. G. Casado and I. Rasines, "The series of spinels $Co_{3-s}Al_sO_4$ (0<s< 2): Study of Co_2AlO_4," *Journal of Solid State Chemistry*, vol. 52, no. 2, pp. 187–190, 1984.

[19] L. Gracia, A. Beltrán, J. Andrés, R. Franco, and J. Recio, "Quantum-mechanical simulation of $MgAl_2O_4$ under high pressure," *Physical Review B*, vol. 66, no. 22, p. 224114, 2002.

[20] T. Irifune, K. Fujino, and E. Ohtani, "A new high-pressure form of $MgAl_2O_2$," *Nature*, vol. 349, no. 6308, p. 409, 1991.

[21] C. O. Arean and E. G. Diaz, "Cation distribution and oxygen parameter in $CdGa_2O_4$-$CoGa_2O_4$ solid solutions," *Materials Chemistry*, vol. 7, no. 5, pp. 675–683, 1982.

[22] J. S. D. Viñuela, C. O. Areán, and F. S. Stone, "Synthesis and structural characterization of $CuAl_2O_4$-$CdAl_2O_4$ spinel solid solutions," *Journal of the Chemical Society, Faraday Transactions 1: Physical Chemistry in Condensed Phases*, vol. 79, no. 5, pp. 1191–1198, 1983.

[23] F. S. Stone, C. O. Areán, J. S. D. Viñuela, and E. E. Platero, "Structural characterization of cadmium-copper gallium oxide ($Cd_xCu_{1-x}Ga_2O_4$) spinels," *Journal of the Chemical Society, Faraday Transactions 1: Physical Chemistry in Condensed Phases*, vol. 81, no. 5, pp. 1255–1261, 1985.

[24] L. K. Kurihara and S. L. Suib, "Sol-gel synthesis of ternary metal oxides. 1. synthesis and characterization of MAl_2O_4 (M= Mg, Ni, Co, Cu, Fe, Zn, Mn, Cd, Ca, Hg, Sr, and Ba) and lead aluminum oxide ($Pb_2Al_2O_5$)," *Chemistry of Materials*, vol. 5, no. 5, pp. 609–613, 1993.

[25] A. Candan and G. Uğur, "First principles study of the structural, elastic, electronic and phonon properties of CdX_2O_4 (X= Al, Ga, In) spinel-type oxides," in *AIP Conference Proceedings*, vol. 1618, pp. 182–185, AIP, 2014.

[26] A. Bouhemadou, R. Khenata, D. Rached, F. Zerarga, and M. Maamache, "Structural, electronic and optical properties of spinel oxides: cadmium gallate and cadmium indate," *The European Physical Journal-Applied Physics*, vol. 38, no. 3, pp. 203–210, 2007.

[27] A. Bouhemadou, R. Khenata, and F. Zerarga, "Prediction study of structural and elastic properties under pressure effect of CdX_2O_4 (X= Al, Ga, In) spinel oxides," *Computational Materials Science*, vol. 39, no. 3, pp. 709–712, 2007.

[28] T. Omata, N. Ueda, N. Hikuma, K. Ueda, H. Mizoguchi, T. Hashimoto, and H. Kawazoe, "New oxide phase with wide band gap and high electroconductivity $CdGa_2O_4$ spinel," *Applied Physics Letters*, vol. 62, no. 5, pp. 499–500, 1993.

[29] H. Kawazoe and K. Ueda, "Transparent conducting oxides based on the spinel structure," *Journal of the American Ceramic Society*, vol. 82, no. 12, pp. 3330–3336, 1999.

[30] S. H. Nguyen and F. Koffyberg, "Optical band gap and electron affinity of semiconducting $CdGa_2O_4$," *Solid State Communications*, vol. 76, no. 11, pp. 1243–1245, 1990.

[31] V. Zhitar, S. Muntean, G. Volodina, E. Arama, and T. Shemyakova, "Photoluminescence in $CdIn_2O_4$ and $CdGa_2O_4$," in *Semiconductor Conference, 2005. CAS 2005 Proceedings. 2005 International*, vol. 2, pp. 301–304, IEEE, 2005.

[32] X. Chu and J. Tamaki, "Dilute CH_3SH sensing characteristics of $CdGa_2O_4$ thick film prepared by sol-gel method," *Electrochemical and Solid-state Letters*, vol. 5, no. 2, pp. H4–H6, 2002.

[33] A. Bouhemadou, F. Zerarga, A. Almuhayya, and S. Bin-Omran, "FP-LAPW study of the fundamental properties of the cubic spinel $CdAl_2O_4$," *Materials Research Bulletin*, vol. 46, no. 12, pp. 2252–2260, 2011.

[34] G. A. Slack and I. C. Huseby, "Thermal Grüneisen parameters of $CdAl_2O_4$, β-Si_3N_4, and other phenacite-type compounds," *Journal of Applied Physics*, vol. 53, no. 10, pp. 6817–6822, 1982.

[35] G. Wu, W. Wang, L. Cai, Y. Hong, Y. Jiang, and C. Wang, "A high performance co-precipitation $CdAl_2O_4$ catalyst for the isomerization of dipotassium 1, 8-naphthalenedicarboxylate," *Reaction Kinetics, Mechanisms and Catalysis*, vol. 119, no. 2, pp. 523–535, 2016.

[36] S. Choi, H. Moon, S.-I. Mho, T. Kim, and H. Park, "Tunable color emission in a $Zn_{1-x}Cd_xGa_2O_4$ phosphor and solid solubility of $CdGa_2O_4$ in $ZnGa_2O_4$," *Materials Research Bulletin*, vol. 33, no. 5, pp. 693–696, 1998.

[37] W. Ran, L. Wang, H. Xu, X. Kong, Y. Sun, D. Qu, and J. Shi, "Nanotunnel structures within metal oxides induce active sites for the strong self-reduction of MnIV to MnII," *Inorganic Chemistry*, vol. 56, no. 6, pp. 3127–3130, 2017.

[38] W. Ran, L. Wang, Q. Liu, G. Liu, D. Qu, X. Pan, and J. Shi, "Mn^{2+} doped $CdAl_2O_4$ phosphors with new structure and special fluorescence properties: experimental and theoretical analysis," *Royal Society of Chemistry Advances*, vol. 7, no. 29, pp. 17612–17619, 2017.

[39] P. M. Keane, Y. J. Lu, and J. A. Ibers, "Copper-containing Group IV and Group V chalcogenides," *Accounts of Chemical Research*, vol. 24, no. 8, pp. 223–229, 1991.

[40] P. Porta, F. Stone, and R. Turner, "Distribution of nickel ions among octahedral and tetrahedral sites in nickel aluminum oxide-magnesium aluminum oxide ($NiAl_2O_4$-$MgAl_2O_4$) solid solutions," *Journal of Solid State Chemistry*, vol. 11, pp. 135–147, 1974.

[41] Z. Yan and H. Takei, "Flux growth of single crystals of spinel $ZnGa_2O_4$ and $CdGa_2O_4$," *Journal of Crystal Growth*, vol. 171, no. 1-2, pp. 131–135, 1997.

[42] M. Segall, P. J. Lindan, M. a. Probert, C. J. Pickard, P. J. Hasnip, S. Clark, and M. Payne, "First-principles simulation: ideas, illustrations and the CASTEP code," *Journal of Physics: Condensed Matter*, vol. 14, no. 11, p. 2717, 2002.

[43] A. Manzar, G. Murtaza, R. Khenata, M. Yousaf, S. Muhammad, *et al.*, "Electronic and optic properties of cubic spinel CdX_2O_4 (X= In, Ga, Al) through Modified Becke-Johnson Potential," *Chinese Physics Letters*, vol. 31, no. 6, p. 067401, 2014.

[44] M. Boujnah, O. Dakir, H. Zaari, A. Benyoussef, and A. El Kenz, "Optoelectronic response of spinels CdX_2O_4 with X=(Al, Ga, In) through the modified Becke-Johnson functional," *Journal of Applied Physics*, vol. 116, no. 12, p. 123703, 2014.

[45] P. Blaha, K. Schwarz, G. K. Madsen, D. Kvasnicka, and J. Luitz, "Wien2K," *An augmented plane wave+ local orbitals program for calculating crystal properties*, 2001.

[46] F. Hulliger, "Neue halbleitende Verbindungen vom Sulvanit-Typ," *Helvetica Physica Acta*, vol. 34, pp. 379–382, 1961.

[47] Y.-J. Lu and J. A. Ibers, "Synthesis and characterization of Cu_3NbSe_4 and KCu_2TaSe_4," *Journal of Solid State Chemistry*, vol. 107, no. 1, pp. 58–62, 1993.

[48] J. Peralta and C. Valencia-Balvín, "Vibrational properties of Cu_3XY_4 sulvanites (X= Nb, Ta, and V; and Y= S, and Se) by *ab initio* molecular dynamics," *The European Physical Journal B*, vol. 90, no. 9, p. 177, 2017.

[49] A. B. Kehoe, D. O. Scanlon, and G. W. Watson, "Modelling potential photovoltaic absorbers Cu_3MCh_4 (M= V, Nb, Ta; Ch= S, Se, Te) using density functional theory," *Journal of Physics: Condensed Matter*, vol. 28, no. 17, p. 175801, 2016.

[50] W. Espinosa-García, S. Pérez-Walton, J. Osorio-Guillén, and C. M. Araujo, "The electronic and optical properties of the sulvanite compounds: a many-body perturbation and time-dependent density functional theory study," *Journal of Physics: Condensed Matter*, vol. 30, no. 3, p. 035502, 2017.

[51] J. Hafner, "Ab-initio simulations of materials using VASP: Density-functional theory and beyond," *Journal of computational Chemistry*, vol. 29, no. 13, pp. 2044–2078, 2008.

[52] Y. Li, M. Wu, T. Zhang, X. Qi, G. Ming, G. Wang, X. Quan, and D. Yang, "Natural sulvanite Cu_3MX_4 (M= Nb, Ta; X= S, Se): Promising visible-light photocatalysts for water splitting," *Computational Materials Science*, vol. 165, pp. 137–143, 2019.

[53] J.-c. Zheng, "Recent advances on thermoelectric materials," *Frontiers of Physics in China*, vol. 3, no. 3, pp. 269–279, 2008.

[54] W. Naffouti, T. B. Nasr, H. Meradji, and N. Kamoun-Turki, "First-principles investigation of structural, thermal and transport properties of anatase TiO_2," *Journal of Electronic Materials*, vol. 45, no. 10, pp. 5096–5103, 2016.

[55] M. W. Gaultois, T. D. Sparks, C. K. Borg, R. Seshadri, W. D. Bonificio, and D. R. Clarke, "Data-driven review of thermoelectric materials: performance and resource considerations," *Chemistry of Materials*, vol. 25, no. 15, pp. 2911–2920, 2013.

[56] P. Vaqueiro, R. A. R. Al Orabi, S. D. Luu, G. Guelou, A. V. Powell, R. Smith, J.-P. Song, D. Wee, and M. Fornari, "The role of copper in the thermal conductivity of thermoelectric

oxychalcogenides: do lone pairs matter?," *Physical Chemistry Chemical Physics*, vol. 17, no. 47, pp. 31735–31740, 2015.

[57] M. K. Yadav and B. Sanyal, "First principles study of thermoelectric properties of Li-based half-heusler alloys," *Journal of Alloys and Compounds*, vol. 622, pp. 388–393, 2015.

[58] C. Wood, "Materials for thermoelectric energy conversion," *Reports on Progress in Physics*, vol. 51, no. 4, p. 459, 1988.

[59] L. Xi, J. Yang, L. Wu, J. Yang, and W. Zhang, "Band engineering and rational design of high-performance thermoelectric materials by first-principles," *Journal of Materiomics*, vol. 2, no. 2, pp. 114–130, 2016.

[60] G. J. Snyder and E. S. Toberer, "Complex thermoelectric materials," in *materials for sustainable energy: a collection of peer-reviewed research and review articles from Nature Publishing Group*, pp. 101–110, World Scientific, 2011.

[61] A. Shakouri, "Recent developments in semiconductor thermoelectric physics and materials," *Annual Review of Materials Research*, vol. 41, 2011.

[62] D. Rowe, "CRC handbook of thermoelectrics CRC Press," *Boca Raton, New York, London, Tokyo*, 1995.

[63] Y. Saeed, A. Kachmar, and M. A. Carignano, "First-principles study of the transport properties in bulk and monolayer MX_3 (M = Ti, Zr, Hf and X= S, Se) compounds," *The Journal of Physical Chemistry C*, vol. 121, no. 3, pp. 1399–1403, 2017.

[64] G. Mahan and J. Sofo, "The best thermoelectric," *Proceedings of the National Academy of Sciences*, vol. 93, no. 15, pp. 7436–7439, 1996.

[65] J. Mao, H. Zhu, Z. Ding, Z. Liu, G. A. Gamage, G. Chen, and Z. Ren, "High thermoelectric cooling performance of n-type Mg_3Bi_2-based materials," *Science*, vol. 365, no. 6452, pp. 495–498, 2019.

[66] Q. Jiang, J. Yang, Y. Liu, and H. He, "Microstructure tailoring in nanostructured thermoelectric materials," *Journal of Advanced Dielectrics*, vol. 6, no. 01, p. 1630002, 2016.

[67] C. Uher, "Skutterudites: Prospective novel thermoelectrics," in *Semiconductors and Semimetals*, vol. 69, pp. 139–253, Elsevier, 2001.

[68] N. P. Blake, S. Latturner, J. D. Bryan, G. D. Stucky, and H. Metiu, "Band structures and thermoelectric properties of the clathrates $Ba_8Ga_{16}Ge_{30}$, $Sr_8Ga_{16}Ge_{30}$, $Ba_8Ga_{16}Si_{30}$, and $Ba_8In_{16}Sn_{30}$," *The Journal of Chemical Physics*, vol. 115, no. 17, pp. 8060–8073, 2001.

[69] B. Sales, D. Mandrus, and R. K. Williams, "Filled skutterudite antimonides: a new class of thermoelectric materials," *Science*, vol. 272, no. 5266, pp. 1325–1328, 1996.

[70] Z. Chen, X. Zhang, and Y. Pei, "Manipulation of phonon transport in thermoelectrics," *Advanced Materials*, vol. 30, no. 17, p. 1705617, 2018.

[71] J. Yang, "Potential applications of thermoelectric waste heat recovery in the automotive industry," in *ICT 2005. 24th International Conference on Thermoelectrics, 2005.*, pp. 170–174, IEEE, 2005.

[72] K. Matsubara, "Development of a high efficient thermoelectric stack for a waste exhaust heat recovery of vehicles," in *Twenty-First International Conference on Thermoelectrics, 2002. Proceedings ICT'02.*, pp. 418–423, IEEE, 2002.

[73] D. Rowe, "Applications of nuclear-powered thermoelectric generators in space," *Applied Energy*, vol. 40, no. 4, pp. 241–271, 1991.

[74] R. L. Heacock, "The Voyager spacecraft," *Proceedings of the Institution of Mechanical Engineers*, vol. 194, no. 1, pp. 211–224, 1980.

[75] S. Mandal and G. Song, "Thermal sensors for performance evaluation of protective clothing against heat and fire: a review," *Textile Research Journal*, vol. 85, no. 1, pp. 101–112, 2015.

[76] M. D. Gilley and R. L. Webb, "Thermoelectric refrigerator with evaporating/condensing heat exchanger," Dec. 21 1999. US Patent 6,003,319.

[77] T. Harman, P. Taylor, M. Walsh, and B. LaForge, "Quantum dot superlattice thermoelectric materials and devices," *Science*, vol. 297, no. 5590, pp. 2229–2232, 2002.

[78] A. M. Curcio, "Portable cooler," Mar. 23 1971. US Patent 3,572,054.

[79] N. Putra, "Design, manufacturing and testing of a portable vaccine carrier box employing thermoelectric module and heat pipe," *Journal of Medical Engineering & Technology*, vol. 33, no. 3, pp. 232–237, 2009.

[80] L. E. Bell, "Cooling, heating, generating power, and recovering waste heat with thermoelectric systems," *Science*, vol. 321, no. 5895, pp. 1457–1461, 2008.

[81] J. J. F. Belton and S. Leo, "Thermoelectric air conditioning apparatus," Aug. 16 1960. US Patent 2,949,014.

[82] A. B. Newton, "Thermoelectric air conditioning systems," May 24 1966. US Patent 3,252,504.

[83] C. F. Alsing, "Thermoelectric air conditioning unit," June 26 1962. US Patent 3,040,538.

[84] A. Boyer and E. Cisse, "Properties of thin film thermoelectric materials: application to sensors using the seebeck effect," *Materials Science and Engineering: B*, vol. 13, no. 2, pp. 103–111, 1992.

[85] M. J. Muehlbauer, E. J. Guilbeau, and B. C. Towe, "Applications and stability of a thermoelectric enzyme sensor," *Sensors and Actuators B: Chemical*, vol. 2, no. 3, pp. 223–232, 1990.

[86] W. Shin, M. Matsumiya, N. Izu, and N. Murayama, "Hydrogen-selective thermoelectric gas sensor," *Sensors and Actuators B: Chemical*, vol. 93, no. 1-3, pp. 304–308, 2003.

[87] C. Acar, I. Dincer, and G. F. Naterer, "Review of photocatalytic water-splitting methods for sustainable hydrogen production," *International Journal of Energy Research*, vol. 40, no. 11, pp. 1449–1473, 2016.

[88] D. L. Stojić, M. P. Marčeta, S. P. Sovilj, and Š. S. Miljanić, "Hydrogen generation from water electrolysis-possibilities of energy saving," *Journal of Power Sources*, vol. 118, no. 1-2, pp. 315–319, 2003.

[89] T. Kodama, N. Gokon, and R. Yamamoto, "Thermochemical two-step water splitting by ZrO_2-supported $Ni_xFe_{3-x}O_4$ for solar hydrogen production," *Solar Energy*, vol. 82, no. 1, pp. 73–79, 2008.

[90] S. Bashi, N. Mailah, and M. Yusof, "Production of hydrogen using photovoltaic electrolysis," in *Proceedings. Student Conference on Research and Development, 2003. SCORED 2003.*, pp. 282–285, IEEE, 2003.

[91] I. Abe, "Photovoltaic cell-water electrolysis system," *Energy Carriers Conversion Systems*, vol. 1, pp. 1–3, 2001.

[92] A. K. Ghosh and H. P. Maruska, "Photoelectrolysis of water in sunlight with sensitized semiconductor electrodes," *Journal of The Electrochemical Society*, vol. 124, no. 10, pp. 1516–1522, 1977.

[93] J. Yu and P. Takahashi, "Biophotolysis-based hydrogen production by cyanobacteria and green microalgae," *Communicating Current Research and Educational Topics and Trends in Applied Microbiology*, vol. 1, pp. 79–89, 2007.

[94] R. Hino, K. Haga, H. Aita, and K. Sekita, "38. R&D on hydrogen production by high-temperature electrolysis of steam," *Nuclear Engineering and Design*, vol. 233, no. 1-3, pp. 363–375, 2004.

[95] H. Iwahara, H. Uchida, and I. Yamasaki, "High-temperature steam electrolysis using $SrCeO_3$-based proton conductive solid electrolyte," *International Journal of Hydrogen Energy*, vol. 12, no. 2, pp. 73–77, 1987.

[96] I. Abe, "Hydrogen production from water," *Energy Carriers Conversion Systems*, vol. 1, pp. 1–3, 2001.

[97] S. Parsons, *Advanced oxidation processes for water and wastewater treatment*. International Water Association (IWA) publishing, 2004.

[98] Y. Wang, H. Suzuki, J. Xie, O. Tomita, D. J. Martin, M. Higashi, D. Kong, R. Abe, and J. Tang, "Mimicking natural photosynthesis: solar to renewable H_2 fuel synthesis by Z-scheme water splitting systems," *Chemical Reviews*, vol. 118, no. 10, pp. 5201–5241, 2018.

[99] L. Duan, L. Tong, Y. Xu, and L. Sun, "Visible light-driven water oxidation-from molecular catalysts to photoelectrochemical cells," *Energy & Environmental Science*, vol. 4, no. 9, pp. 3296–3313, 2011.

[100] U. Gupta and C. Rao, "Hydrogen generation by water splitting using MoS_2 and other transition metal dichalcogenides," *Nano Energy*, vol. 41, pp. 49–65, 2017.

[101] C. Gao, J. Wang, H. Xu, and Y. Xiong, "Coordination chemistry in the design of heterogeneous photocatalysts," *Chemical Society Reviews*, vol. 46, no. 10, pp. 2799–2823, 2017.

[102] N. M. Gupta, "Factors affecting the efficiency of a water splitting photocatalyst: A perspective," *Renewable and Sustainable Energy Reviews*, 2016.

[103] A. Fujishima and K. Honda, "Photolysis-decomposition of water at the surface of an irradiated semiconductor," *Nature*, vol. 238, no. 5385, pp. 37–38, 1972.

[104] K. Maeda and K. Domen, "New non-oxide photocatalysts designed for overall water splitting under visible light," *The Journal of Physical Chemistry C*, vol. 111, no. 22, pp. 7851–7861, 2007.

[105] M. C. Toroker, D. K. Kanan, N. Alidoust, L. Y. Isseroff, P. Liao, and E. A. Carter, "First principles scheme to evaluate band edge positions in potential transition metal oxide photocatalysts and photoelectrodes," *Physical Chemistry Chemical Physics*, vol. 13, no. 37, pp. 16644–16654, 2011.

[106] X. Jiang, P. Wang, and J. Zhao, "2D covalent triazine framework: a new class of organic photocatalyst for water splitting," *Journal of Materials Chemistry A*, vol. 3, no. 15, pp. 7750–7758, 2015.

[107] R. Navarro, F. Del Valle, J. V. de la Mano, M. Álvarez-Galván, and J. Fierro, "Photocatalytic water splitting under visible light: concept and catalysts development," *Advances in Chemical Engineering*, vol. 36, pp. 111–143, 2009.

[108] K. Maeda, "Z-scheme water splitting using two different semiconductor photocatalysts," *American Chemical Society Catalysis*, vol. 3, no. 7, pp. 1486–1503, 2013.

[109] A. O. Ibhadon and P. Fitzpatrick, "Heterogeneous photocatalysis: recent advances and applications," *Catalysts*, vol. 3, no. 1, pp. 189–218, 2013.

[110] Y. Wu, P. Lazic, G. Hautier, K. Persson, and G. Ceder, "First principles high throughput screening of oxynitrides for water-splitting photocatalysts," *Energy & Environmental Science*, vol. 6, no. 1, pp. 157–168, 2013.

[111] A. Kudo and Y. Miseki, "Heterogeneous photocatalyst materials for water splitting," *Chemical Society Reviews*, vol. 38, no. 1, pp. 253–278, 2009.

[112] A. J. Bard, "Photoelectrochemistry and heterogeneous photo-catalysis at semiconductors," *Journal of Photochemistry*, vol. 10, no. 1, pp. 59–75, 1979.

[113] S. Curtarolo, G. L. Hart, M. B. Nardelli, N. Mingo, S. Sanvito, and O. Levy, "The high-throughput highway to computational materials design," *Nature Materials*, vol. 12, no. 3, pp. 191–201, 2013.

[114] P. Liu, J. Nisar, R. Ahuja, and B. Pathak, "Layered perovskite $Sr_2Ta_2O_7$ for visible light photocatalysis: a first principles study," *The Journal of Physical Chemistry C*, vol. 117, no. 10, pp. 5043–5050, 2013.

[115] A. Kudo, "Photocatalyst materials for water splitting," *Catalysis Surveys from Asia*, vol. 7, no. 1, pp. 31–38, 2003.

[116] J. Ye, Z. Zou, H. Arakawa, M. Oshikiri, M. Shimoda, A. Matsushita, and T. Shishido, "Correlation of crystal and electronic structures with photophysical properties of water splitting photocatalysts $InMO_4$ (M = V^{5+}, Nb^{5+}, Ta^{5+})," *Journal of Photochemistry and Photobiology A: Chemistry*, vol. 148, no. 1, pp. 79–83, 2002.

[117] D. Li and H. Haneda, "Morphologies of zinc oxide particles and their effects on photocatalysis," *Chemosphere*, vol. 51, no. 2, pp. 129–137, 2003.

[118] A. Testino, I. R. Bellobono, V. Buscaglia, C. Canevali, M. D'Arienzo, S. Polizzi, R. Scotti, and F. Morazzoni, "Optimizing the photocatalytic properties of hydrothermal TiO_2 by the control of phase composition and particle morphology. A systematic approach," *Journal of the American Chemical Society*, vol. 129, no. 12, pp. 3564–3575, 2007.

[119] H. Bonzel, U. Breuer, B. Voigtländer, and E. Zeldov, "Temperature-dependent morphologies of gold surfaces," *Surface Science*, vol. 272, no. 1-3, pp. 10–16, 1992.

[120] P. Dong, Y. Wang, H. Li, H. Li, X. Ma, and L. Han, "Shape-controllable synthesis and morphology-dependent photocatalytic properties of Ag_3PO_4 crystals," *Journal of Materials Chemistry A*, vol. 1, no. 15, pp. 4651–4656, 2013.

[121] E. D. Williams, "Surface steps and surface morphology: understanding macroscopic phenomena from atomic observations," *Surface Science*, vol. 299, pp. 502–524, 1994.

[122] J. Van Brakel, "Pure chemical substances," *Stuff: The Nature of Chemical Substances*, pp. 145–161, 2008.

[123] J. Yu, C. Y. Jimmy, M. K.-P. Leung, W. Ho, B. Cheng, X. Zhao, and J. Zhao, "Effects of acidic and basic hydrolysis catalysts on the photocatalytic activity and microstructures of bimodal mesoporous titania," *Journal of Catalysis*, vol. 217, no. 1, pp. 69–78, 2003.

[124] K. Maeda and K. Domen, "Photocatalytic water splitting: recent progress and future challenges," *The Journal of Physical Chemistry Letters*, vol. 1, no. 18, pp. 2655–2661, 2010.

[125] A. A. Ismail and D. W. Bahnemann, "Photochemical splitting of water for hydrogen production by photocatalysis: a review," *Solar Energy Materials and Solar Cells*, vol. 128, pp. 85–101, 2014.

[126] D. Zhao, J.-F. Han, J.-Y. Cui, X. Zong, and C. Li, "A new Pb (iv)-based photocathode material Sr_2PbO_4 with good light harvesting ability," *Journal of Materials Chemistry A*, vol. 3, no. 22, pp. 12051–12058, 2015.

[127] J. Schneider, M. Matsuoka, M. Takeuchi, J. Zhang, Y. Horiuchi, M. Anpo, and D. W. Bahnemann, "Understanding TiO_2 photocatalysis: mechanisms and materials," *Chemical Reviews*, vol. 114, no. 19, pp. 9919–9986, 2014.

[128] S. C. Roy, O. K. Varghese, M. Paulose, and C. A. Grimes, "Toward solar fuels: photocatalytic conversion of carbon dioxide to hydrocarbons," *American Chemical Society Nano*, vol. 4, no. 3, pp. 1259–1278, 2010.

[129] J. Tang and J. Ye, "Photocatalytic and photophysical properties of visible-light-driven photocatalyst $ZnBi_{12}O_{20}$," *Chemical Physics Letters*, vol. 410, no. 1, pp. 104–107, 2005.

[130] J. Bockris, "Hydrogen economy in the future," *International Journal of Hydrogen Energy*, vol. 24, no. 1, pp. 1–15, 1999.

[131] W. Wang, X. Chen, G. Liu, Z. Shen, D. Xia, P. K. Wong, and C. Y. Jimmy, "Monoclinic dibismuth tetraoxide: A new visible-light-driven photocatalyst for environmental remediation," *Applied Catalysis B: Environmental*, vol. 176, pp. 444–453, 2015.

[132] J. Reddy, S. Kurra, R. Guje, S. Palla, N. K. Veldurthi, G. Ravi, and M. Vithal, "Photocatalytic degradation of methylene blue on nitrogen doped layered perovskites, $CsM_2Nb_3O_{10}$ (M = Ba and Sr)," *Ceramics International*, vol. 41, no. 2, pp. 2869–2875, 2015.

[133] M. R. Hoffmann, S. T. Martin, W. Choi, and D. W. Bahnemann, "Environmental applications of semiconductor photocatalysis," *Chemical Reviews*, vol. 95, no. 1, pp. 69–96, 1995.

[134] J. C. Ireland, P. Klostermann, E. W. Rice, and R. M. Clark, "Inactivation of escherichia coli by titanium dioxide photocatalytic oxidation.," *Applied and Environmental Microbiology*, vol. 59, no. 5, pp. 1668–1670, 1993.

[135] R. Cai, Y. Kubota, T. Shuin, H. Sakai, K. Hashimoto, and A. Fujishima, "Induction of cytotoxicity by photoexcited TiO_2 particles," *Cancer Research*, vol. 52, no. 8, pp. 2346–2348, 1992.

[136] J. M. Robertson, P. K. Robertson, and L. A. Lawton, "A comparison of the effectiveness of TiO_2 photocatalysis and UVA photolysis for the destruction of three pathogenic micro-organisms," *Journal of Photochemistry and Photobiology A: Chemistry*, vol. 175, no. 1, pp. 51–56, 2005.

[137] M. T. Khan, D. Chatterjee, and M. Bala, "Photocatalytic reduction of N_2 to NH_3 sensitized by the [RuIII-ethylenediaminetetraacetate-2, 2-bipyridyl]- complex in a Pt-TiO_2 semiconductor particulate system," *Journal of Photochemistry and Photobiology A: Chemistry*, vol. 67, no. 3, pp. 349–352, 1992.

[138] M. T. Khan, D. Chatterjee, M. Krishnaratnam, and M. Bala, "Photosensitized reduction of N_2 by RuII (bipy) 32^+ adsorbed on the surface of $Pt/TiO_2/RuO_2$ semiconductor particulate system containing RuIII-EDTA complex and L-ascorbic acid," *Journal of Molecular Catalysis*, vol. 72, no. 1, pp. 13–18, 1992.

[139] N. Jackson, C. M. Wang, Z. Luo, J. Schwitzgebel, J. Ekerdt, J. Brock, and A. Heller, "Attachment of TiO_2 powders to hollow glass microbeads: Activity of the TiO_2-coated beads in the photoassisted oxidation of ethanol to acetaldehyde," *Journal of the Electrochemical Society*, vol. 138, no. 12, pp. 3660–3664, 1991.

[140] A. Fujishima, X. Zhang, and D. A. Tryk, "TiO_2 photocatalysis and related surface phenomena," *Surface Science Reports*, vol. 63, no. 12, pp. 515–582, 2008.

[141] K.-W. Lee and Y.-H. Kim, "Mosquito attracting and killing apparatus with air cleaning function," Mar. 24 2005. US Patent App. 10/984,590.

[142] E. K. Rugut, "Numerical simulation of structural, electronic and optical properties of transition metal chalcogenides," Master's thesis, University of the Witwatersrand, 2017.

[143] P. Hohenberg and W. Kohn, "Inhomogeneous electron gas," *Physical Review*, vol. 136, no. 3B, p. B864, 1964.

[144] E. Zahedi, M. Hojamberdiev, and M. F. Bekheet, "Effective masses, electronic and optical properties of (111)-layered B-site deficient hexagonal perovskite $Ba_5M_4O_{15}$ (M = Ta, Nb): a DFT study using HSE06," *Royal Society of Chemistry Advances*, vol. 6, no. 66, pp. 61150–61161, 2016.

[145] R. G. Pearson, "Absolute electronegativity and hardness: application to inorganic chemistry," *Inorganic Chemistry*, vol. 27, no. 4, pp. 734–740, 1988.

[146] C. Catlow and A. Stoneham, "Ionicity in solids," *Journal of Physics C: Solid State Physics*, vol. 16, no. 22, p. 4321, 1983.

[147] B. Viswanathan, "Photocatalytic processes-selection criteria for the choice of materials," *Bulletin of the Catalysis Society of India*, vol. 2, p. 71, 2003.

[148] J. P. Perdew and M. Levy, "Physical content of the exact Kohn-Sham orbital energies: band gaps and derivative discontinuities," *Physical Review Letters*, vol. 51, no. 20, p. 1884, 1983.

[149] L. I. Bendavid and E. A. Carter, "First-principles predictions of the structure, stability, and photocatalytic potential of Cu_2O surfaces," *The Journal of Physical Chemistry B*, vol. 117, no. 49, pp. 15750–15760, 2013.

[150] X. Wu, R. Wang, and S. Wang, "Generalized-stacking-fault energy and surface properties for HCP metals: A first-principles study," *Applied Surface Science*, vol. 256, no. 11, pp. 3409–3412, 2010.

[151] M. Batzill, "Fundamental aspects of surface engineering of transition metal oxide photocatalysts," *Energy & Environmental Science*, vol. 4, no. 9, pp. 3275–3286, 2011.

[152] S. Salustro, A. M. Ferrari, R. Orlando, and R. Dovesi, "Comparison between cluster and supercell approaches: the case of defects in diamond," *Theoretical Chemistry Accounts*, vol. 136, no. 4, p. 42, 2017.

[153] J. Greeley, J. K. Nørskov, and M. Mavrikakis, "Electronic structure and catalysis on metal surfaces," *Annual Review of Physical Chemistry*, vol. 53, no. 1, pp. 319–348, 2002.

[154] J. Steckel, T. Phung, K. D. Jordan, and P. Nachtigall, "Concerted use of slab and cluster models in an *ab initio* study of hydrogen desorption from the Si(100) surface," *The Journal of Physical Chemistry B*, vol. 105, no. 18, pp. 4031–4038, 2001.

[155] K. Kearney, A. Rockett, and E. Ertekin, "Computational insights into charge transfer across functionalized semiconductor surfaces," *Science and Technology of Advanced Materials*, vol. 18, no. 1, pp. 681–692, 2017.

[156] S. Kondo, M. Nakamura, N. Maki, and N. Hoshi, "Active sites for the oxygen reduction reaction on the low and high index planes of palladium," *The Journal of Physical Chemistry C*, vol. 113, no. 29, pp. 12625–12628, 2009.

[157] A. Lock, J. Toennies, and G. Witte, "Surface phonons of stepped metal surfaces," *Journal of Electron Spectroscopy and Related Phenomena*, vol. 54, pp. 309–316, 1990.

[158] M. Van Hove and G. Somorjai, "A new microfacet notation for high-miller-index surfaces of cubic materials with terrace, step and kink structures," *Surface Science*, vol. 92, no. 2-3, pp. 489–518, 1980.

[159] G. G. Rusina and E. V. Chulkov, "Phonons on the clean metal surfaces and in adsorption structures," *Russian Chemical Reviews*, vol. 82, no. 6, p. 483, 2013.

[160] G.-H. Lu, M. Huang, M. Cuma, and F. Liu, "Relative stability of Si surfaces: A first-principles study," *Surface Science*, vol. 588, no. 1-3, pp. 61–70, 2005.

[161] D. Su, S. Dou, and G. Wang, "Gold nanocrystals with variable index facets as highly effective cathode catalysts for lithium-oxygen batteries," *Nature Publishing Group Asia Materials*, vol. 7, no. 1, p. e155, 2015.

[162] N. E. Singh-Miller and N. Marzari, "Surface energies, work functions, and surface relaxations of low-index metallic surfaces from first principles," *Physical Review B*, vol. 80, no. 23, p. 235407, 2009.

[163] J. Goniakowski, F. Finocchi, and C. Noguera, "Polarity of oxide surfaces and nanostructures," *Reports on Progress in Physics*, vol. 71, no. 1, p. 016501, 2007.

[164] F. Liu, M. Hohage, and M. Lagally, "Encyclopedia of Applied Physics," 1999.

[165] G. Liu, C. Y. Jimmy, G. Q. M. Lu, and H.-M. Cheng, "Crystal facet engineering of semiconductor photocatalysts: motivations, advances and unique properties," *Chemical Communications*, vol. 47, no. 24, pp. 6763–6783, 2011.

[166] N. Hörmann and A. Groß, "Stability, composition and properties of Li_2FeSiO_4 surfaces studied by DFT," *Journal of Solid State Electrochemistry*, vol. 18, no. 5, pp. 1401–1413, 2014.

[167] H. L. Skriver and N. Rosengaard, "Surface energy and work function of elemental metals," *Physical Review B*, vol. 46, no. 11, p. 7157, 1992.

[168] W. Tyson and W. Miller, "Surface free energies of solid metals: Estimation from liquid surface tension measurements," *Surface Science*, vol. 62, no. 1, pp. 267–276, 1977.

[169] D. A. Tompsett, S. C. Parker, and M. S. Islam, "Surface properties of α-MnO_2: relevance to catalytic and supercapacitor behaviour," *Journal of Materials Chemistry A*, vol. 2, no. 37, pp. 15509–15518, 2014.

[170] J. L. Da Silva, C. Stampfl, and M. Scheffler, "Converged properties of clean metal surfaces by all-electron first-principles calculations," *Surface Science*, vol. 600, no. 3, pp. 703–715, 2006.

[171] A. Kahn, "Fermi level, work function and vacuum level," *Materials Horizons*, vol. 3, no. 1, pp. 7–10, 2016.

[172] M. Yu and D. R. Trinkle, "Accurate and efficient algorithm for bader charge integration," *The Journal of Chemical Physics*, vol. 134, no. 6, p. 064111, 2011.

[173] G. Henkelman, A. Arnaldsson, and H. Jónsson, "A fast and robust algorithm for bader decomposition of charge density," *Computational Materials Science*, vol. 36, no. 3, pp. 354–360, 2006.

[174] A. E. Reed, R. B. Weinstock, and F. Weinhold, "Natural population analysis," *The Journal of Chemical Physics*, vol. 83, no. 2, pp. 735–746, 1985.

[175] F. Hirshfeld, "XVII. Spatial partitioning of charge density," *Israel Journal of Chemistry*, vol. 16, no. 2-3, pp. 198–201, 1977.

[176] P. Bultinck, C. Van Alsenoy, P. W. Ayers, and R. Carbó-Dorca, "Critical analysis and extension of the Hirshfeld atoms in molecules," *The Journal of Chemical Physics*, vol. 126, no. 14, p. 144111, 2007.

[177] W. Tang, E. Sanville, and G. Henkelman, "A grid-based Bader analysis algorithm without lattice bias," *Journal of Physics: Condensed Matter*, vol. 21, no. 8, p. 084204, 2009.

[178] A. Faghanina, *Theory of Carrier Transport From First Principles: Applications in Photovoltaic and Thermoelectric Materials*. PhD thesis, Washington University in St. Louis, 2016.

[179] J. Singh, *Modern physics for engineers*. John Wiley & Sons, 2008.

[180] A. Togo, L. Chaput, and I. Tanaka, "Distributions of phonon lifetimes in Brillouin zones," *Physical Review B*, vol. 91, no. 9, p. 094306, 2015.

[181] Z. Tian, S. Lee, and G. Chen, "A comprehensive review of heat transfer in thermoelectric materials and devices," *Annual Review of Heat Transfer*, vol. 17, pp. 425–483, 2014.

[182] A. Bulusu and D. Walker, "Review of electronic transport models for thermoelectric materials," *Superlattices and Microstructures*, vol. 44, no. 1, pp. 1–36, 2008.

[183] G. Nolas, J. Sharp, and J. Goldsmid, *Thermoelectrics: Basic Principles and New Materials Developments*. Springer Series in Materials Science, Springer Berlin Heidelberg, 2013.

[184] T. M. Tritt, "Thermoelectric materials: Principles, structure, properties, and applications," 2002.

[185] N. T. Hung, A. R. Nugraha, and R. Saito, "Two-dimensional InSe as a potential thermoelectric material," *Applied Physics Letters*, vol. 111, no. 9, p. 092107, 2017.

[186] G. K. Madsen, J. Carrete, and M. J. Verstraete, "BoltzTraP2, a program for interpolating band structures and calculating semi-classical transport coefficients," *Computer Physics Communications*, vol. 231, pp. 140–145, 2018.

[187] P. Sundarraj, D. Maity, S. S. Roy, and R. A. Taylor, "Recent advances in thermoelectric materials and solar thermoelectric generators-a critical review," *Royal Society of Chemistry Advances*, vol. 4, no. 87, pp. 46860–46874, 2014.

[188] D. Sun Lee, T.-H. An, M. Jeong, H.-S. Choi, Y. Soo Lim, W.-S. Seo, C.-H. Park, C. Park, and H.-H. Park, "Density of state effective mass and related charge transport properties in K-doped BiCuOSe," *Applied Physics Letters*, vol. 103, no. 23, p. 232110, 2013.

[189] H. Wang, S. Li, Y. Liu, J. Ding, Y.-H. Lin, H. Xu, B. Xu, and C.-W. Nan, "$Bi_{1-x}La_xCuSeO$ as new tunable full solar light active photocatalysts," *Scientific Reports*, vol. 6, 2016.

[190] J. Zhang, P. Zhou, J. Liu, and J. Yu, "New understanding of the difference of photocatalytic activity among anatase, rutile and brookite TiO_2," *Physical Chemistry Chemical Physics*, vol. 16, no. 38, pp. 20382–20386, 2014.

[191] J. Zhang, W. Yu, J. Liu, and B. Liu, "Illustration of high-active Ag_2CrO_4 photocatalyst from the first-principle calculation of electronic structures and carrier effective mass," *Applied Surface Science*, vol. 358, pp. 457–462, 2015.

[192] C.-M. Liegener, "Derivation of Rowe's renormalized random phase approximation from the Bethe-Salpeter equation," *Physics Letters A*, vol. 85, no. 6-7, pp. 324–326, 1981.

[193] J. J. Plata, D. Usanmaz, P. Nath, C. Toher, J. Carrete, M. Asta, M. de Jong, M. B. Nardelli, M. Fornari, and S. Curtarolo, "Predicting the lattice thermal conductivity of solids by solving the Boltzmann transport equation: AFLOW-AAPL an automated, accurate and effecient framework," *arXiv preprint arXiv:1611.05481*, 2016.

[194] I. E. Castelli, K. W. Jacobsen, and K. S. Thygesen, *Computational Screening of Materials for Water Splitting Applications*. PhD thesis, Technical University of Denmark (DTU), 2013.

[195] J. P. Perdew, K. Burke, and M. Ernzerhof, "Generalized gradient approximation made simple," *Physical Review Letters*, vol. 77, no. 18, p. 3865, 1996.

[196] A. D. Becke, "Density-functional exchange-energy approximation with correct asymptotic behavior," *Physical Review A*, vol. 38, no. 6, p. 3098, 1988.

[197] M. Ropo, K. Kokko, and L. Vitos, "Assessing the Perdew-Burke-Ernzerhof exchange-correlation density functional revised for metallic bulk and surface systems," *Physical Review B*, vol. 77, no. 19, p. 195445, 2008.

[198] F. Tran and P. Blaha, "Accurate band gaps of semiconductors and insulators with a semilocal exchange-correlation potential," *Physical Review Letters*, vol. 102, no. 22, p. 226401, 2009.

[199] J. Oudenhoven, F. Scheijen, and M. Wollfs, "Fundamental of photocatalytic water splitting by visible light," *Chemistry of Catalytic System 2: Photocatalysis*, pp. 1–22, 2004.

[200] H. Zhang, L. Liu, and Z. Zhou, "First-principles studies on facet-dependent photocatalytic properties of bismuth oxyhalides (BiOXs)," *Royal Society of Chemistry Advances*, vol. 2, no. 24, pp. 9224–9229, 2012.

[201] Z. Han, L. Ren, Z. Cui, C. Chen, H. Pan, and J. Chen, "Ag/ZnO flower heterostructures as a visible-light driven photocatalyst via surface plasmon resonance," *Applied Catalysis B: Environmental*, vol. 126, pp. 298–305, 2012.

[202] G. Liu, L. Wang, H. G. Yang, H.-M. Cheng, and G. Q. M. Lu, "Titania-based photocatalysts-crystal growth, doping and heterostructuring," *Journal of Materials Chemistry*, vol. 20, no. 5, pp. 831–843, 2010.

[203] D. P. Woodruff, *Modern techniques of surface science*. Cambridge university press, 2016.

[204] H. Shodja and C. Enzevaee, "Surface characterization of face-centered cubic crystals," *Mechanics of Materials*, vol. 129, pp. 15–22, 2019.

[205] H. Lüth, "Optical spectroscopy of electronic surface states," *Applied Physics*, vol. 8, no. 1, pp. 1–14, 1975.

[206] M. Bouri and U. Aschauer, "Bulk and surface properties of the Ruddlesden-Popper oxynitride Sr_2TaO_3N," *Physical Chemistry Chemical Physics*, vol. 20, no. 4, pp. 2771–2776, 2018.

[207] V. Berkovits, V. Kiselev, and V. Safarov, "Optical spectroscopy of (110) surfaces of III-V semiconductors," *Surface Science*, vol. 211, pp. 489–502, 1989.

[208] N. W. Ashcroft, "ND Mermin solid state physics," *Saunders College, Philadelphia*, vol. 120, 1976.

[209] A. Togo and I. Tanaka, "First principles phonon calculations in materials science," *Scripta Materialia*, vol. 108, pp. 1–5, 2015.

[210] L. Chaput, A. Togo, I. Tanaka, and G. Hug, "Phonon-phonon interactions in transition metals," *Physical Review B*, vol. 84, no. 9, p. 094302, 2011.

[211] F. Mouhat and F.-X. Coudert, "Necessary and sufficient elastic stability conditions in various crystal systems," *Physical Review B*, vol. 90, no. 22, p. 224104, 2014.

[212] C. Zener, *Elasticity and anelasticity of metals*. University of Chicago press, 1948.

[213] E. Güler and M. Güler, "Phase transition and elasticity of gallium arsenide under pressure," *Materials Research*, vol. 17, no. 5, pp. 1268–1272, 2014.

[214] W. Voigt *et al.*, *Lehrbuch der kristallphysik*, vol. 962. Teubner Leipzig, 1928.

[215] A. Reuss, "Calculation of the flow limits of mixed crystals on the basis of the plasticity of monocrystals," *Zeitschrift für Angewandte Mathematik und Mechanik*, vol. 9, pp. 49–58, 1929.

[216] R. Hill, "The elastic behaviour of a crystalline aggregate," *Proceedings of the Physical Society. Section A*, vol. 65, no. 5, p. 349, 1952.

[217] S. Pugh, "XCII. Relations between the elastic moduli and the plastic properties of polycrystalline pure metals," *The London, Edinburgh, and Dublin Philosophical Magazine and Journal of Science*, vol. 45, no. 367, pp. 823–843, 1954.

[218] S. Tariq, A. Ahmed, S. Saad, and S. Tariq, "Structural, electronic and elastic properties of the cubic $CaTiO_3$ under pressure: A DFT study," *American Institute of Physics Advances*, vol. 5, no. 7, p. 077111, 2015.

[219] J. Haines, J. Leger, and G. Bocquillon, "Synthesis and design of superhard materials," *Annual Review of Materials Research*, vol. 31, no. 1, pp. 1–23, 2001.

[220] X.-Q. Chen, H. Niu, D. Li, and Y. Li, "Modeling hardness of polycrystalline materials and bulk metallic glasses," *Intermetallics*, vol. 19, no. 9, pp. 1275–1281, 2011.

[221] O. L. Anderson, "A simplified method for calculating the debye temperature from elastic constants," *Journal of Physics and Chemistry of Solids*, vol. 24, no. 7, pp. 909–917, 1963.

[222] T. Nakashima and Y. Umakoshi, "Anisotropy of electrical resistivity and thermal expansion of single-crystal Ti_5Si_3," *Philosophical Magazine Letters*, vol. 66, no. 6, pp. 317–321, 1992.

[223] J. Bardeen and W. Shockley, "Deformation potentials and mobilities in non-polar crystals," *Physical Review*, vol. 80, no. 1, p. 72, 1950.

[224] J. Xi, M. Long, L. Tang, D. Wang, and Z. Shuai, "First-principles prediction of charge mobility in carbon and organic nanomaterials," *Nanoscale*, vol. 4, no. 15, pp. 4348–4369, 2012.

[225] A. Gold-Parker, P. M. Gehring, J. M. Skelton, I. C. Smith, D. Parshall, J. M. Frost, H. I. Karunadasa, A. Walsh, and M. F. Toney, "Acoustic phonon lifetimes limit thermal transport in methylammonium lead iodide," *Proceedings of the National Academy of Sciences*, vol. 115, no. 47, pp. 11905–11910, 2018.

[226] L. Yeh and R. Chu, "Thermal interface resistance," in *Thermal Management of Microelectronic Equipment*, ASME Press, 2002.

[227] C. D. Wright, L. Wang, P. Shah, M. M. Aziz, E. Varesi, R. Bez, M. Moroni, and F. Cazzaniga, "The design of rewritable ultrahigh density scanning-probe phase-change memories," *IEEE Transactions on Nanotechnology*, vol. 10, no. 4, pp. 900–912, 2010.

[228] X. Wu, J. Lee, V. Varshney, J. L. Wohlwend, A. K. Roy, and T. Luo, "Thermal conductivity of wurtzite zinc-oxide from first-principles lattice dynamics-a comparative study with gallium nitride," *Scientific Reports*, vol. 6, p. 22504, 2016.

[229] D. G. Cahill, P. V. Braun, G. Chen, D. R. Clarke, S. Fan, K. E. Goodson, P. Keblinski, W. P. King, G. D. Mahan, A. Majumdar, *et al.*, "Nanoscale thermal transport. II. 2003–2012," *Applied Physics Reviews*, vol. 1, no. 1, p. 011305, 2014.

[230] S. N. H. Eliassen, "A first principles study of lattice thermal conductivity in XNiSn (X= Ti, Zr, Hf) half-heusler alloys for thermoelectric applications," Master's thesis, University of Oslo, 2016.

[231] B. Peng, H. Zhang, H. Shao, Z. Ning, Y. Xu, G. Ni, H. Lu, D. W. Zhang, and H. Zhu, "Stability and strength of atomically thin borophene from first principles calculations," *Materials Research Letters*, vol. 5, no. 6, pp. 399–407, 2017.

[232] A. Togo, L. Chaput, I. Tanaka, and G. Hug, "First-principles phonon calculations of thermal expansion in Ti_3SiC_2, Ti_3AlC_2, and Ti_3GeC_2," *Physical Review B*, vol. 81, no. 17, p. 174301, 2010.

[233] E. L. Da Silva, J. M. Skelton, S. C. Parker, and A. Walsh, "Phase stability and transformations in the halide perovskite $CsSnI_3$," *Physical Review B*, vol. 91, no. 14, p. 144107, 2015.

[234] E. Kaxiras, *Atomic and electronic structure of solids*. Cambridge University Press, 2003.

[235] N. Vočadlo and G. D. Price, "The Grüneisen parameter-computer calculations via lattice dynamics," *Physics of the Earth and Planetary Interiors*, vol. 82, no. 3-4, pp. 261–270, 1994.

[236] G. A. Slack, "Nonmetallic crystals with high thermal conductivity," *Journal of Physics and Chemistry of Solids*, vol. 34, no. 2, pp. 321–335, 1973.

[237] M. Huber, "Sur la répartition des cations dans les spinelles $MgGa_2O_4$ et $CdGa_2O_4$," *Journal de Chimie Physique*, vol. 57, pp. 202–227, 1960.

[238] C. O. Arean, M. R. Martinez, and A. M. Arjona, "Structural study of $Cd_xNi_{1-x}Al_2O_4$ spinels," *Materials Chemistry and Physics*, vol. 8, no. 5, pp. 443–450, 1983.

[239] S.-D. Mo and W. Ching, "Electronic structure of normal, inverse, and partially inverse spinels in the $MgAl_2O_4$ system," *Physical Review B*, vol. 54, no. 23, p. 16555, 1996.

[240] N. Mounet and N. Marzari, "First-principles determination of the structural, vibrational and thermodynamic properties of diamond, graphite, and derivatives," *Physical Review B*, vol. 71, no. 20, p. 205214, 2005.

[241] H. Alves, J. Alves, A. Santos, L. Scolfaro, and J. Leite, "Ab initio calculation of the (100) and (110) surface phonon dispersion of GaAs and GaN," *Brazilian Journal of Physics*, vol. 34, no. 2B, pp. 617–619, 2004.

[242] M. Laing and M. Laing, "Dulong and Petit's law: we should not ignore its importance," *Journal of Chemical Education*, vol. 83, no. 10, p. 1499, 2006.

[243] T. Liang, W.-Q. Chen, C.-E. Hu, X.-R. Chen, and Q.-F. Chen, "Lattice dynamics and thermal conductivity of lithium fluoride via first-principles calculations," *Solid State Communications*, vol. 272, pp. 28–32, 2018.

[244] J. P. Perdew, A. Ruzsinszky, G. I. Csonka, O. A. Vydrov, G. E. Scuseria, L. A. Constantin, X. Zhou, and K. Burke, "Restoring the density-gradient expansion for exchange in solids and surfaces," *Physical Review Letters*, vol. 100, no. 13, p. 136406, 2008.

[245] B. Ghebouli, M. Ghebouli, M. Fatmi, and A. Bouhemadou, "First-principles study of the structural, elastic, electronic, optical and thermodynamic properties of the cubic perovskite $CsCdCl_3$ under high pressure," *Solid State Communications*, vol. 150, no. 39, pp. 1896–1901, 2010.

[246] W. G. Aulbur, L. Jönsson, and J. W. Wilkins, "Quasiparticle calculations in solids," *Solid State Physics*, vol. 54, pp. 1–218, 2000.

[247] B. D. Viezbicke, S. Patel, B. E. Davis, and D. P. Birnie III, "Evaluation of the Tauc method for optical absorption edge determination: ZnO thin films as a model system," *Physica Status Solidi (b)*, vol. 252, no. 8, pp. 1700–1710, 2015.

[248] V. Fiorentini and M. Methfessel, "Extracting convergent surface energies from slab calculations," *Journal of Physics: Condensed Matter*, vol. 8, no. 36, p. 6525, 1996.

[249] F. Ojaghnezhad and H. M. Shodja, "A combined first principles and analytical treatment for determination of the surface elastic constants: application to Si (001) ideal and reconstructed surfaces," *Philosophical Magazine Letters*, vol. 92, no. 1, pp. 7–19, 2012.

[250] L. Wang, F. Zhou, Y. Meng, and G. Ceder, "First-principles study of surface properties of $LiFePO_4$: Surface energy, structure, Wulff shape, and surface redox potential," *Physical Review B*, vol. 76, no. 16, p. 165435, 2007.

[251] E. J. Siem, W. C. Carter, and C. Dominique, "The equilibrium shape of anisotropic interfacial particles," *Philosophical Magazine*, vol. 84, no. 10, pp. 991–1010, 2004.

[252] P. Lazar and M. Otyepka, "Accurate surface energies from first principles," *Physical Review B*, vol. 91, no. 11, p. 115402, 2015.

[253] E. Ringe, R. Van Duyne, and L. Marks, "Wulff construction for alloy nanoparticles," *Nano Letters*, vol. 11, no. 8, pp. 3399–3403, 2011.

[254] R. E. García and J. Blendell, "Equilibrium wulff shape generator," Jun 2012.

[255] Y. Su, H. Li, H. Ma, J. Robertson, and A. Nathan, "Controlling surface termination and facet orientation in Cu_2O nanoparticles for high photocatalytic activity: a combined experimental and density functional theory study," *American Chemical Society Applied Materials & Interfaces*, vol. 9, no. 9, pp. 8100–8106, 2017.

[256] G. Liu, X. Wang, L. Wang, Z. Chen, F. Li, G. Q. M. Lu, and H.-M. Cheng, "Drastically enhanced photocatalytic activity in nitrogen doped mesoporous TiO_2 with abundant surface states," *Journal of Colloid and Interface Science*, vol. 334, no. 2, pp. 171–175, 2009.

[257] W. Zhang, J. Tang, and J. Ye, "Structural, photocatalytic, and photophysical properties of perovskite $MSnO_3$ (M= Ca, Sr, and Ba) photocatalysts," *Journal of Materials Research*, vol. 22, no. 7, pp. 1859–1871, 2007.

[258] K. Momma and F. Izumi, "VESTA 3 for three-dimensional visualization of crystal, volumetric and morphology data," *Journal of Applied Crystallography*, vol. 44, no. 6, pp. 1272–1276, 2011.

[259] J. Simfukwe, R. E. Mapasha, A. Braun, and M. Diale, "Density functional theory study of Cu doped $\{0001\}$ and $\{0112\}$ surfaces of hematite for water splitting," *Materials Research Society Advances*, vol. 3, no. 13, pp. 669–678, 2018.

[260] M. Butler and D. Ginley, "Prediction of flatband potentials at semiconductor-electrolyte interfaces from atomic electronegativities," *Journal of the Electrochemical Society*, vol. 125, no. 2, pp. 228–232, 1978.

[261] K. Choudhary and F. Tavazza, "Automatic convergence and machine learning predictions of monkhorst-pack k-points and plane-wave cut-off in density functional theory," *arXiv preprint arXiv:1809.01753*, 2018.

[262] G. Kresse and J. Furthmüller, "Vasp 4.6 guide http://cms. mpi. univie. ac. at," 2007.

[263] C. Kittel *et al.*, *Introduction to solid state physics*, vol. 8. Wiley New York, 1976.

[264] D. Sholl and J. A. Steckel, *Density functional theory: a practical introduction*. John Wiley & Sons, 2011.

[265] L. Li, *Theoretical and Computational Studies Related to Solar Water Splitting with Semiconductor Alloys*. PhD thesis, The Graduate School, Stony Brook University: Stony Brook, NY., 2011.

[266] H. L. Zhuang and R. G. Hennig, "Single-layer group-III monochalcogenide photocatalysts for water splitting," *Chemistry of Materials*, vol. 25, no. 15, pp. 3232–3238, 2013.